Architectures for Improved Organic Semiconductor Devices

Jonathan H. Beck

Submitted in partial fulfillment of the
requirements for the degree
of Doctor of Philosophy
in the Graduate School of Arts and Sciences

COLUMBIA UNIVERSITY

2014

ABSTRACT

Architectures for Improved Organic Semiconductor Devices

Jonathan H. Beck

Advancements in the microelectronics industry have brought increasing performance and decreasing prices to a wide range of users. Conventional silicon-based electronics have followed Moore's law to provide an ever-increasing integrated circuit transistor density, which drives processing power, solid-state memory density, and sensor technologies. As shrinking conventional integrated circuits became more challenging, researchers began exploring electronics with the potential to penetrate new applications with a low price of entry: "Electronics everywhere." The new generation of electronics is thin, light, flexible, and inexpensive.

Organic electronics are part of the new generation of thin-film electronics, relying on the synthetic flexibility of carbon molecules to create organic semiconductors, absorbers, and emitters which perform useful tasks. Organic electronics can be fabricated with low energy input on a variety of novel substrates, including inexpensive plastic sheets. The potential ease of synthesis and fabrication of organic-based devices means that organic electronics can be made at very low cost. Successfully demonstrated organic semiconductor devices include photovoltaics, photodetectors, transistors, and light emitting diodes.

Several challenges that face organic semiconductor devices are low performance relative to conventional devices, long-term device stability, and development of new organic-compatible processes and materials. While the absorption and emission performance of organic materials in photovoltaics and light emitting diodes is extraordi-

narily high for thin films, the charge conduction mobilities are generally low. Building highly efficient devices with low-mobility materials is one challenge. Many organic semiconductor films are unstable during fabrication, storage, and operation due to reactions with water, oxygen and hydroxide. A final challenge facing organic electronics is the need for new processes and materials for electrodes, semiconductors and substrates compatible with low-temperature, flexible, and oxygenated and aromatic solvent-free fabrication. Materials and processes must be capable of future high volume production in order to enable low costs. In this thesis we explore several techniques to improve organic semiconductor device performance and enable new fabrication processes.

In Chapter 2, I describe the integration of sub-optical-wavelength nanostructured electrodes that improve fill factor and power conversion efficiency in organic photovoltaic devices. Photovoltaic fill factor performance is one of the primary challenges facing organic photovoltaics because most organic semiconductors have poor charge mobility. Our electrical and optical measurements and simulations indicate that nanostructured electrodes improve charge extraction in organic photovoltaics.

In Chapter 3, I describe a general method for maximizing the efficiency of organic photovoltaic devices by simultaneously optimizing light absorption and charge carrier collection. We analyze the potential benefits of light trapping strategies for maximizing the overall power conversion efficiency of organic photovoltaic devices. This technique may be used to improve organic photovoltaic materials with low absorption, or short exciton diffusion and carrier-recombination lengths, opening up the device design space.

In Chapter 4, I describe a process for high-quality graphene transfer onto chemically sensitive, weakly interacting organic semiconductor thin-films. Graphene is a promising flexible and highly transparent electrode for organic electronics; however, transferring graphene films onto organic semiconductor devices was previously impossible. We demonstrate a new transfer technique based on an elastomeric stamp

coated with an fluorinated polymer release layer. We fabricate three classes of organic semiconductor devices: field effect transistors without high temperature annealing, transparent organic light-emitting diodes, and transparent small-molecule organic photovoltaic devices.

Table of Contents

List of Figures

List of Tables

Acknowledgments

I would first like to thank my advisor, Professor Ioannis Kymissis, for his guidance and sharing his knowledge. And second, all past and present members of the Columbia Laboratory for Unconventional Electronics. I would particularly like to thank my early mentors Dr. Yu-Jen Hsu, Dr. Nadia Pervez, Dr. Zhang Jia, Dr. Vincent Lee, and Dr. Marshall Cox. My fellow researchers Hassan Edrees, Shyuan Yang, Fabio Carta, Amrita Masurkar, Kostas Alexandrou, and Aida Colon Berrios have engaged me with great discussions and helpful advice.

I would like to thank fellow Columbia EFRC researchers for their discussions and collaborations, especially Muhammad Alam and Biswajit Ray from Purdue University. I would like to thank Charles Black and his research group at Brookhaven National Laboratory, especially Danvers Johnston, Chang-Yong Nam, Aaron Stein, and Ming Lu for many hours of discussion about nanofabrication. I would like to thank Cheng-Chia Tsai, Richard Grote, Richard Osgood, Jr. and Dirk Englund for their contributions to optics analysis. I would like acknowledge the assistance and previous graphene research of Marshall Cox, Robert Barton, Kostas Alexandrou and Nick Petrone.

I would like to acknowledge the financial and material support of the Energy Frontier Research Center, Brookhaven National Laboratory, and National Institute of Standards and Technology, where the majority of the research for my thesis took place. Finally, I must thank the Columbia Center for Integrated Science and Engineering and Department of Electrical Engineering for endless assistance in supporting our research activities.

I would like to thank my friends and family for their love and support; I couldn't have come this far without you. To my mom, dad, brother and sister.

Chapter 1

Introduction

1.1 Background and Motivation

According to the U.S. Energy Information Administration, global energy use is projected to increase by 56% between 2010 and 2040, Figure 1.1. Global carbon dioxide emissions are estimated to rise by 46% during the same period. In the United States, about 65% of electricity is generated from non-renewable sources like coal and natural gas. We must provide new renewable energy sources to meet increasing energy demands with less carbon output. Renewable energy technologies are a potential solution to provide more electricity, reduce the effects of global climate change and reduce pollution.

A brief summary of global renewable energy sources, and their current utilization, is listed in Table 1.1. Solar energy has a large untapped capacity to supply on the order of hundreds of exajoules worth of energy per year. Global adoption of renewable energy sources like photovoltaics is growing by 2.5% annually. The price of crystalline silicon photovoltaic (PV) cells has dropped from ˜$8 per watt in the 1990's to a forecast $0.74 per watt in 2013. [3] The price of power generated by silicon PV has steadily dropped as economics of scale have pushed down the prices of fabrication, installation and raw materials. Silicon PV can compete with traditional

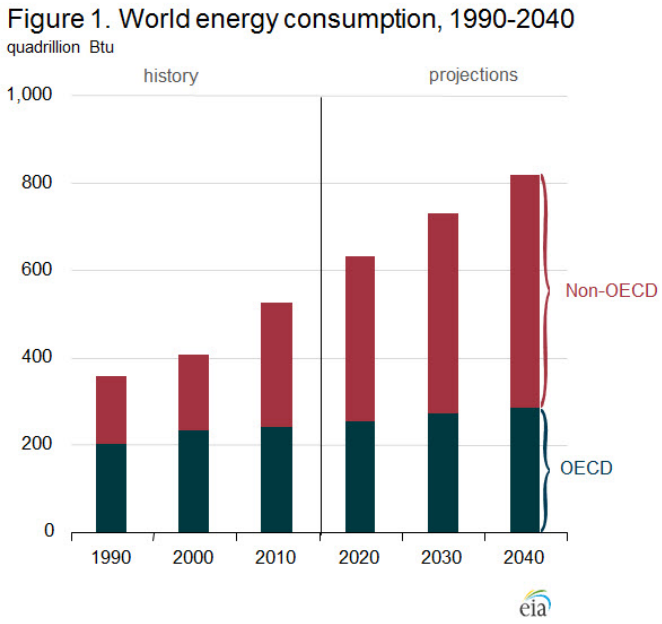

Figure 1.1: World energy consumption, 1990-2040. Adapted from the U.S. Energy Information Administration. [1]

Type	Resource EJ/year	Implemented EJ/year	Percentage explored
Solar	2730000	0.31	0.0012%
Wind	2500	4.0	0.16%
Geothermal	1000	1.2	0.10%
Hydro	52	9.3	18.0%

Table 1.1: Global renewable energy resources: explored, implemented. Adapted from Chen [2]

energy sources in some energy markets. However, lower prices will further encourage adoption and competition with electricity produced by petroleum, natural gas and coal. New photovoltaic energy technologies have the potential to reduce the cost of renewable energy sources, increase adoption by enabling new PV system architectures, and increase the efficiency of current PV systems.

Organic photovoltaics (OPVs) are a renewable energy technology that could potentially be high-volume and inexpensive. OPV research is driven by the demand for high-efficiency, low-cost photovoltaic cells. There has been significant research progress and initial industry progress towards commercialization of OPV technologies. Traditional inorganic PVs require high material purity and high-temperature processing (˜1400°C), which increase the cost of production. High temperature processing is incompatible with many substrates, such as flexible plastics and cellulose. Organic materials can be processed in solution at room temperature or deposited with physical vapor deposition at low temperatures (100-300°C). The relatively low processing temperature enables a wider choice of substrates. OPV cells enable commercial and novel device architectures include columnar strands, partially transparent sheets for architectural surfaces, and flexible plastic panels [4, 5]. Organic photovoltaics are a promising renewable energy technology due to their potential low cost, compatibility with roll-to-roll processing, and demonstrated power conversion efficiencies above 10% [6, 7].

A second technology enabled by advanced organic semiconductors devices is the Organic Light Emitting Diode (OLED). OLEDs are useful for digital emissive displays such as televisions and mobile phones, and overhead lighting. Light emitting diodes (LEDs) and LED displays are important technologies that have grown into virtually every field. OLED displays offer advantages over traditional LED displays such as low cost, flexible plastic substrates, high visual contrast ratio, wide viewing angle, and high power efficiency.

Organic electronics have great potential to disrupt the electronics industry because they enable new device architectures with potentially inexpensive materials, with inexpensive packaging such as plastics, with unprecedented ability to integrate sensors, actuators, digital logic, energy collection, and energy storage. The current obstacles to organic electronics are performance, development of industrial fabrication processes, and device stability. If these challenges can be met, organic electronics

may power a new generation of electronics. Major themes discussed throughout this thesis are organic photovoltaics (OPVs), organic light emitting diodes (OLEDs), and graphene.

1.2 Organic Semiconductor Devices

1.2.1 Introduction to Organic Electronics

Organic semiconductors are carbon-based molecules with electron delocalization that is created by sp^2 hybridization. Organic semiconductors are compelling materials because they can be made on a low thermal budget and are elemental abundant. Since many organic materials form van der Waals bonds, the energetic input required for assembly of thin films is low. Furthermore, many useful organic devices can be formed without epitaxial or crystal growth. A large variety of organic materials can be designed and synthesized due to the chemical flexibility of carbon molecules. Performance of organic electronics have been catching up to inorganic devices and surpasses the challenge of placing electronics on a wide variety of substrates, including plastic sheets, paper cellulose, and glass.

Interest in organic electronics accelerated with the demonstration of the first OFETs, OPVs [8] and OLEDs [9] in the late 1980's. Excitement grew as chemists synthesized soluble organic semiconductor materials, enabling solution processing techniques. We now have a wide variety of substrates, semiconductors, insulators, and processing techniques to build organic semiconductor devices. OLED devices have begun to see great commercials interest in the smartphone and television market as high-contrast and flexible displays.

Organic semiconductor materials can be divided into two categories: polymers and small molecules. Polymers are made up of small carbon-rich units such as -vinyls, -thiophenes, and -pyrroles in long chains. Several polymeric organic semiconductor are shown in Figure 1.2; the top row shows electron donor materials while the bottom

row shows electron acceptor materials. Polythiophene and polyfluorene are well-known polymer semiconductors. The molecular orientation of polymers often has a significant effect on intermolecular charge transport and device performance. [10] Polymers can be synthesized to have a high rate of packing and a low energy input for crystallization. Substrate heating, surface temperature and morphology engineering all determine the properties of the organic polymer thin films. Polymer and soluble organic molecules are mainly processed from solution; polymers decompose when heated or may have too large of a molecular mass for evaporation. Small molecule organic semiconductors are low molecular weight, unpolymerized units. In some cases, functional units can be added to make the small molecules soluble. Pentacene and C60 are well-known small molecule organic semiconductors, as is the functionalized, soluble C60 derivative [6,6]-phenyl-C61-butyric acid methyl ester (PCBM). Several small molecule organic semiconductors are shown in Figure 1.3. Small molecules are mainly deposited with thermal physical vapor deposition.

In inorganic semiconductor band theory, the valence and conduction bands describe the state of electron mobility in a material. In organic semiconductors these bands roughly correspond to the highest occupied molecular orbital (HOMO) and lowest unoccupied molecular orbital (LUMO). The location of the HOMO and LUMO levels determines whether the material easily transports electrons or holes. The absorption of the organic material is determined by energetic transitions from the LUMO to the HOMO level.

The semiconductor energy levels are also important when selecting metal contacts. Barriers to charge injection and extraction at the electrode metal-semiconductor junctions depend on the difference between the metal work function and the HOMO/LUMO levels. There is also an influence of interface dipoles which can shift the band alignment. [12] Commonly used interface electrodes are listed with their work functions in Table 1.2. Au is a popular metal for accessing the HOMO level of organic semiconductors while Al and Ca are used to access the LUMO levels. Low work

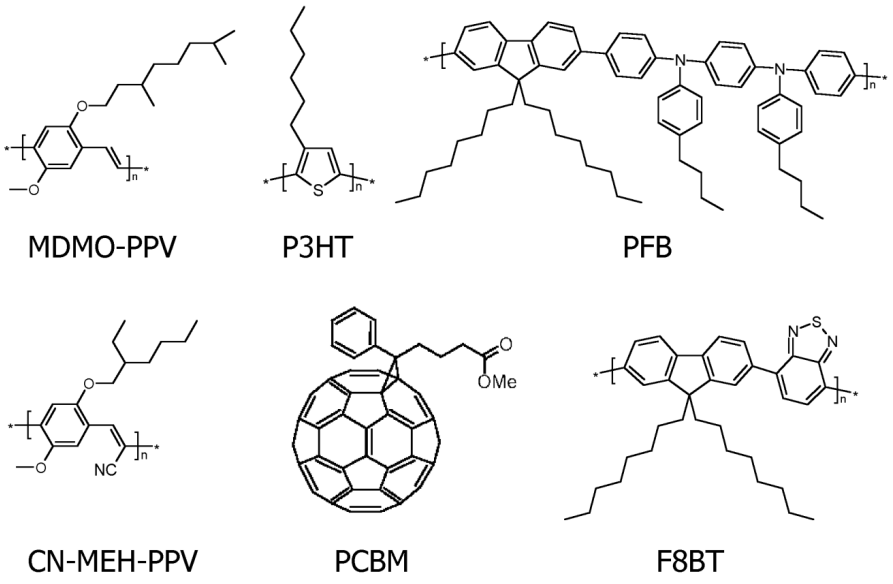

Figure 1.2: Solution processable polymeric organic semiconductors. Top row: MDMO-PPV (poly[2-methoxy-5-(3',7'-dimethyloctyloxy)]-1,4-phenylenevinylene), P3HT (poly(3-hexylthiophene-2,5- diyl) and PFB (poly(9,9'-dioctylfluorene-co-bis-N,N'-(4-butylphenyl)-bis-N,N'-phenyl-1,4-phenylenediamine). Bottom row: CN-MEH-PPV (poly-[2-methoxy-5-(2'-ethylhexyloxy)-1,4-(1-cyanovinylene)-phenylene), F8TB (poly(9,9'- dioctylfluorene-co-benzothiadiazole) and PCBM (1-(3-methoxycarbonyl) propyl-1-phenyl[6,6]C61). Reprinted (adapted) with permission from [11]. Copyright 2004 Materials Research Society.

function metals are difficult to incorporate because their low activation energy makes them naturally reactive. The stability of low work function metals can be increased by making them very thin (˜ 1 nm) and followed by higher work function metals, or alloyed with other metals during a co-deposition process.

1.2.2 Organic Semiconductor Stability

Stability is a major challenge to organic electronics. Organic semiconductors react with H^+ ions, OH^- ions and O_2 molecules which are readily available in the environ-

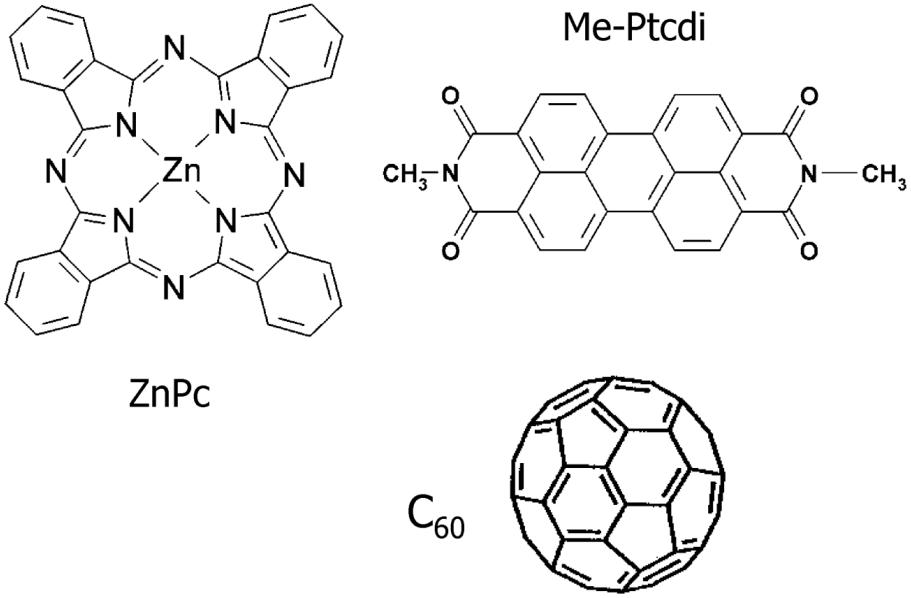

Figure 1.3: Small molecule organic semiconductors: ZnPc (zinc-phthalocyanine), Me-PTCDI (N,N'-dimethyl-perylene-3,4,9,10-dicarboximide), and fullerene C_{60}. Reprinted (adapted) with permission from [11]. Copyright 2004 Materials Research Society.

ment. The energy input required to interact with ions can be increased by engineering the HOMO and LUMO levels; however, n-type organic materials are difficult to stabilize because their Fermi level is higher, so the redox potential is lower. [14] The environmental stability problem is often solved by encapsulation and synthesis of more stable molecules. Encapsulation has been a topic of significant research in the OFET, OLED and OPV communities. Plastic sheets, glass, metals, metal oxides, and graphene can be used to seal the organic material from the environment; desiccant can be placed in the sealed cavity to passivate residual water and oxygen. Lightweight and transparent roll-coating barriers have been developed for flexible displays. [15]

Metal	Work function (eV)
Ca	2.87
Al	4.28
Cu	4.65
Au	5.05
Pd	5.12
Ni	5.15
Pt	5.65

Table 1.2: Common electrode metals with their work functions. [13]

1.3 Organic Photovoltaics

1.3.1 OPV Device Physics

Organic photovoltaics (OPVs) may potentially bring low cost, low weight and highly flexible solar cells to a wide market. Organic semiconductors generally have strong absorption, which makes them useful for thin-film photovoltaic devices. The match between absorption coefficient and the AM 1.5 solar spectrum is shown in Figure 1.4. The best OPV materials have a large absorption overlap with the solar spectrum. Many organic semiconductors have optical band gaps around 2 eV, which places their absorption strongly in the blue and reduces their maximum theoretical photogenerated current. [11] One difference between organic photovoltaics and conventional PV is that OPV are majority carrier devices, which means that the hole is transported in the donor and the electron is transported in the acceptor. In conventional PV, the minority carriers are holes in the n-type side and electrons in the p-type side of the junction.

The process of photocurrent generation in a heterojunction device is schematically shown in Figure 1.5. In the first step, light is absorbed by one of the organic semiconductor active layers. We call this an active layer because it is absorbing light

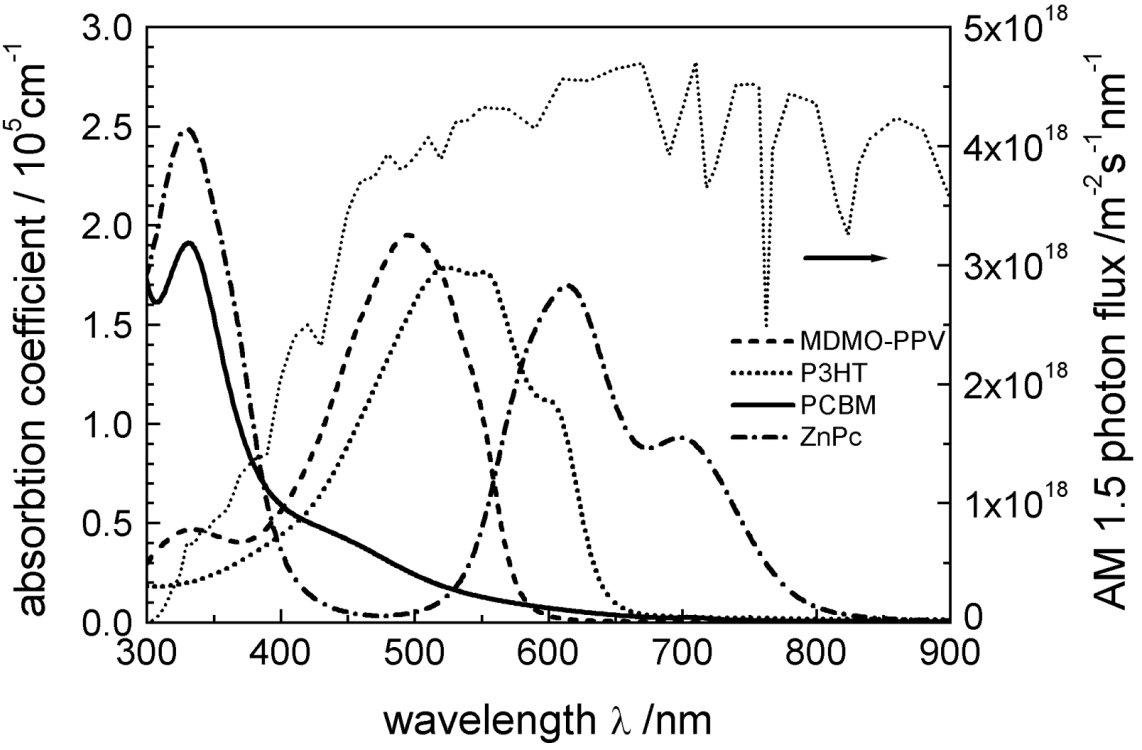

Figure 1.4: Absorption coefficients of common materials used in OPV devices in comparison with the radiant flux of the AM 1.5 solar spectrum. Reprinted (adapted) with permission from [11]. Copyright 2004 Materials Research Society.

and transporting charge. The photon energy excites an electron from the HOMO band to the LUMO band and creates a bound particle called an exciton. The exciton has a binding energy of 0.5 - 1.0 eV and is neutrally charged. The electron/hole in Figure 1.5 are shown with energy levels less than the HOMO/LUMO to account for the binding energy of the exciton. The exciton must diffuse to a dissociation site at the donor/acceptor junction where the difference in electron energy level between the donor/acceptor is sufficient to break the exciton binding energy, resulting in an electron in the acceptor layer and a hole in the donor layer. The difference in work functions of anode and cathode attracts the free electrons and holes to the respective contacts.

We can quantitatively describe the steps of photovoltaic energy transfer with the

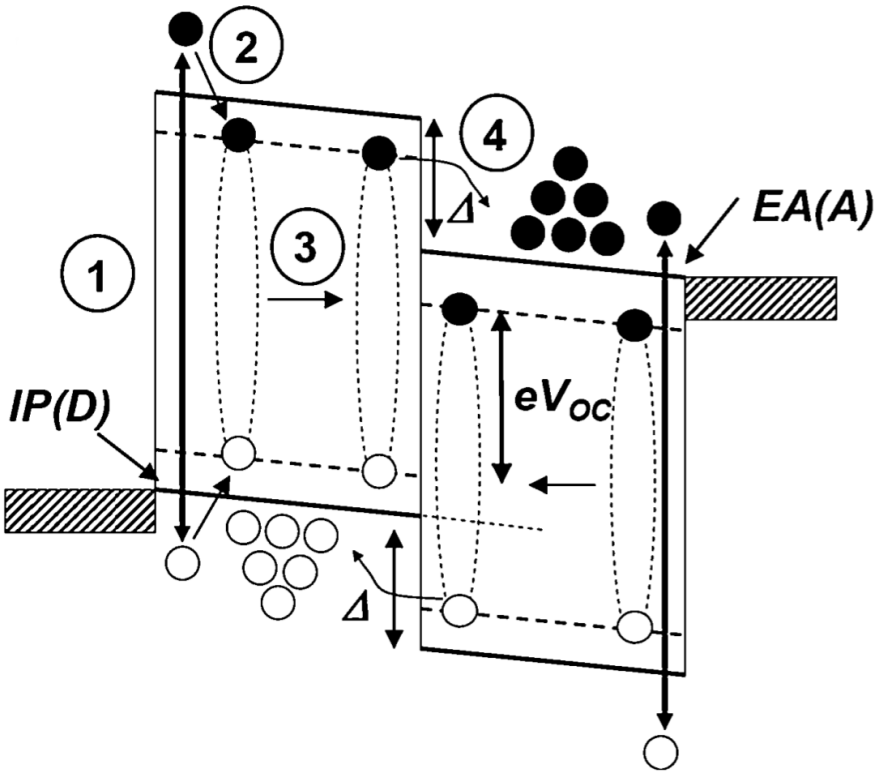

Figure 1.5: Schematic of OPV energy collection and transfer. Reprinted (adapted) with permission from [16]. Copyright 2009 Royal Society of Chemistry.

External Quantum Efficiency, which describes the number of electrons collected (to the external circuit) per incident photon:

$$\eta_{EQE} = \eta_A(\lambda)\eta_{ED}\eta_{CT}(V)\eta_{CC}(V) \tag{1.1}$$

η_A is the optical absorption efficiency. η_{ED} is the efficiency of photogenerated exciton diffusion to the heterojunction. η_{CT} is the charge transfer efficiency for excitons to dissociate into holes and electrons. η_{CC} is the charge collection efficiency which is the fraction of charge carriers that travel from the heterojunction to the electrodes. [17] This equation describes the conversion of optical energy to electricity.

There is a fundamental trade-off in designing OPV cell thickness because the exciton diffusion length L_D is usually much less than the optical absorption length (1 / α). Exciton diffusion lengths are commonly in the range of 5 - 20 nm. In many

organic materials the charge transfer and charge collection efficiencies (η_{CT} and η_{CC}) are high so the major challenges are absorption and exciton diffusion. In bilayer OPV devices the best performance is achieved when active layer thickness is on the order of the exciton diffusion length, though this results in decreased absorption. [18] Effective strategies to improve performance of bilayer devices are bulk / mixed heterojunction architectures and employing light-trapping schemes to increase optical absorption while maintaining high exciton diffusion efficiency, η_{ED}.

Early homojunction OPV devices transported both electrons and holes in a single layer and had low power conversion efficiencies. The advantage of heterojunction OPV devices over homojunctions is that electrons and holes travel within separate donor/acceptor layers and are therefore less likely to recombine. In heterojunction devices the photocurrent is linearly dependent on illumination and high fill factors are possible. [11] Two types of heterojunction solar cells reviewed here are planar heterojunctions and bulk heterojunctions.

Planar heterojunction (PHJ) photovoltaics are formed by sequentially depositing distinct donor/acceptor films, usually by thermal evaporation. The intersection of donor/acceptor layers forms a junction. A schematic is shown in Figure 1.6a. The first PHJ OPV devices were developed by Tang et al. in 1986 to move away from homojunction photovoltaics. The first PHJ OPV devices paired a -phtalocyanine donor with a -perylene acceptor and achieved almost 1% power conversion efficiency. [8] The best PHJ devices are now 3-4% efficient. The relatively low efficiency of PHJ OPV devices is attributed to a small short-circuit current caused by poor exciton collection efficiency, η_{ED}. [19]

Bulk heterojunction (BHJ) photovoltaic devices mix donor/acceptor materials that form an interpenetrating network in the device active volume. A schematic is shown in Figure 1.6b. BHJ OPVs overcome a bottleneck in exciton dissociation by increasing the surface area between donor/acceptor layers. In 1995 Yu et al. published an early paper on BHJ OPV highlighting the internal network of donor/acceptor het-

erojunctions. These early BHJ devices achieved 2.9% power conversion efficiency at ≈ 0.2 suns illumination. [20] BHJ devices have remained a topic of significant interest and generated efficiencies above 10%. BHJs are often formed by mixing soluble donor/acceptor materials in a solvent, applying them to a conductive electrode, and annealing. The annealing step serves to eliminate residual solvent and cause donor/acceptor domains to form. The performance of BHJ OPV devices is highly dependent on nanoscale morphology of the donor/acceptor phases. Continuous donor/acceptor domains are required to effectively transport electrons/holes to the respective electrodes. BHJ solution processing has generated interest from the OPV community to potentially enable high volume, roll to roll processing without high vacuum processes, which may offer an inexpensive route to commercialized OPV.

1.3.2 OPV Device Structure

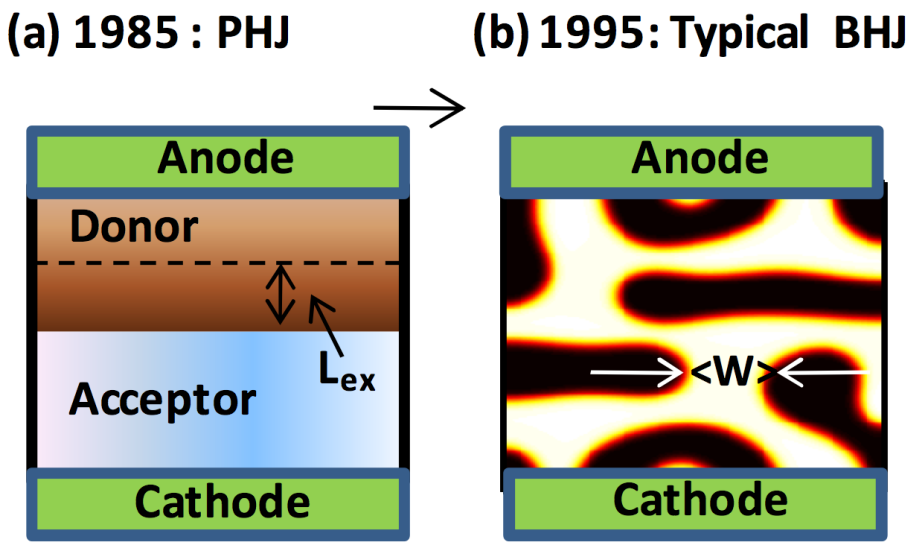

Figure 1.6: a) A planar heterojunction OPV device. b) A bulk heterojunction OPV device. c) Investigation of ideal morphologies for BHJ OPV devices. Reprinted (adapted) with permission from [21]. Copyright 2011 IEEE.

In the following paragraphs we explain the purpose of each thin film element

common to the OPV devices discussed in this thesis:

Electron donor materials, often shortened to donors (D), are characterized by low ionization potentials (HOMO), and typically transport holes. For this reason, donors may also be referred to as hole transporting layers (HTLs). The primary donor material used in OPV devices in this thesis is boron subphthalocyanine chloride (SubPc), which offers improved absorption and open-circuit voltage compared to the earlier donor material copper subphthalocyanine (CuPc). In heterojunction devices, the donor is paired with an acceptor.

Electron acceptor materials, often shortened to acceptors (A), are characterized by a high electron affinity (LUMO) and typically transport electrons. For this reason, acceptors may also be referred to as electron transporting layers (ETLs). The primary donor material used in OPV devices in this thesis is the fullerene C_{60}, which offers high mobility. When selecting the donor and acceptor organic semiconductors for OPVs, the most important material characteristics are absorption profile, charge-carrier mobility, band gap, and exciton diffusion length.

The anode is the hole extracting electrode for the OPV device. The anode work function should be chosen to have a close match to the HOMO of the donor. Indium tin oxide is a common anode material which is popular due to optical transparency and relatively good match to many donor HOMO levels. Thin gold (less than 50 nm thick) can also be sufficiently conductive and transparent over visible wavelengths. Though the anode may commonly be the bottom electrode in OPV devices, the anode may also be placed on top of device stacks to form an inverted OPV device.

The cathode is the electron extracting electrode for the OPV device. The cathode work function is chosen to have a close match to the LUMO level of the acceptor. Common cathodes are silver, magnesium-silver, and aluminum. The cathode often has a low function and is susceptible to oxidation and degradation in ambient environments. In regular OPV devices the cathode is deposited on top of the organic materials; in inverted OPV devices the cathode is deposited prior to organic deposi-

tion.

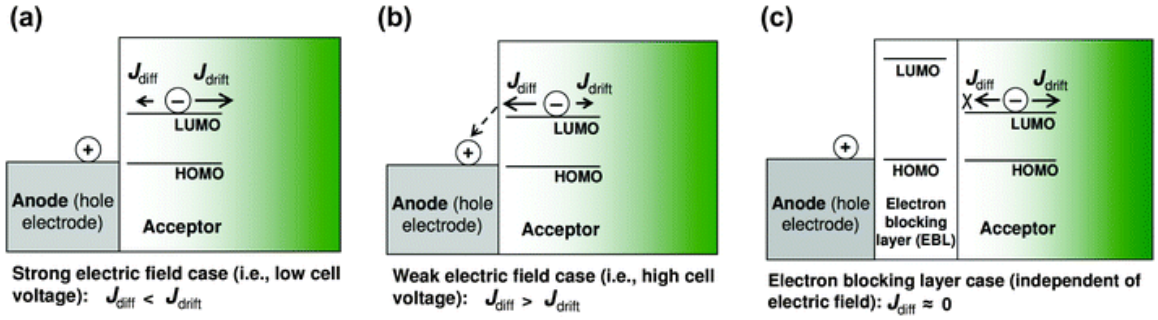

Figure 1.7: The role of electron blocking layers at the interface between the anode and the electrode acceptor. a) Shows the case of direct anode-acceptor contact with a low cell voltage. b) Shows the case of direct anode-acceptor contact with a high cell voltage. c) Shows the insertion of a blocking layer between the anode-acceptor interface. Reprinted (adapted) with permission from [22]. Copyright 2011, The Royal Society of Chemistry.

Injection layers placed between the semiconductor and contact reduce the extraction barrier height. The injection layers may also have a blocking property to become 'selective contacts.' Injection layers are useful when the difference in energy levels between the metal and semiconductor HOMO/LUMO is large. Smaller injection barriers lead to smaller contact resistance. [11] If both donor and acceptor phases contact the electrode, then electrons and holes may recombine at the electrode. A schematic of blocking layer integration is shown in Figure 1.7. In Fig. 1.7a, the V_{oc} is low and a strong electric field exists within the cell. The high electric field creates J_{drift} larger than $J_{diffusion}$, which supports hole transport at the anode. As the V_{oc} increases, Fig. 1.7b, the $J_{diffusion}$ grows and causes electrons to diffuse and recombine at the anode. In Fig. 1.7c the addition of a blocking layer with a LUMO level higher than in the bulk prevents $J_{diffusion}$ from causing electrons to recombine at the anode. A common injection layer at the cathode/organic interface is LiF, which has a lower work function than most cathode metals. A common injection layer at the anode/or-

ganic interface is PEDOT:PSS, which has a higher work function than indium-tin oxide (ITO), which is commonly used as a transparent conducting oxide anode. PEDOT:PSS is commonly deposited by an aqeous/acidic solution and baked. Another option for injection/extraction layers is molybdenum oxide, which is used to reduce the barrier for hole injection/extraction between the anode and organic. MoO_3 was applied as an interlayer in an OPV study and found to reduce the hole extraction barrier, resulting in lower series resistance and improved fill factor performance. [23]

Exciton blocking layers (EBLs) prevent excitons from quenching near the metal electrodes. The oscillating dipole field of the excited molecules induces a field in the metal, causing quenching. [24] EBLs block the transport of excitons because their band gaps are larger than the band gaps in the donor/acceptor materials, which makes exciton transport much less likely. Photoluminescence is commonly used to probe quenching. BCP and TPBi are common exciton blocking layers in OPV devices. [24] The exciton blocking layer has the additional effect of acting as an optical spacer to displace the donor/acceptor junction so it is at the optical field intensity maximum. The D/A junction should ideally be placed near the optical maximum so generated excitons do not have to diffuse over a long distance to reach the junction. [18]

Rand et al. proposed that charge transport in the exciton blocking layer BCP occurs due to damage caused during deposition of metals. The damage-induced defect states permit charge transport, as shown in Figure 1.8, despite a $\sim$ 1.0 eV difference between C_{60} LUMO and BCP LUMO. Damage may not sufficiently penetrate thick layers of BCP, which results in high series resistance and low FF for BCP layers thicker than 10-20 nm. [25] An additional study by Vogel et al. found that BCP creates an ohmic contact between Al and C_{60}. [24] Lassiter et al. found that hole transport from the cathode to the acceptor through BCP causes a net positive electron current into the cathode, also shown in Figure 1.8. [26] The charge conduction mechanism for similar wide-bandgap exciton blocking materials, such as TPBi, could be explored in a similar study. [25] Throughout this study, we implement TPBi as the exciton

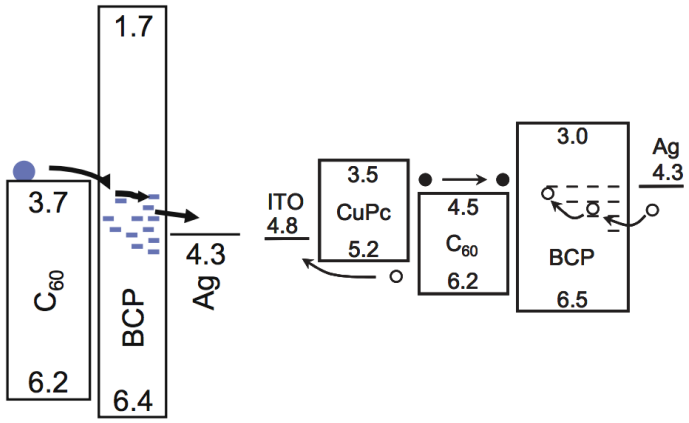

Figure 1.8: Schematic energy diagrams showing two proposed mechanisms for charge transport through the BCP exciton blocking layers. Left: acceptor electrons reach the cathode via trap states in the BCP. Right: acceptor electrons recombine with holes injected from the cathode. From [25, 26]. Copyright 2005 Wiley.

blocking material because TPBi has been found to be more stable than BCP, which degrades via crystallization. [27]

1.3.3 Evaluating OPV Performance

The common photovoltaic figures of merit are power conversion efficiency, short-circuit current, open-circuit voltage, and fill factor. These figures of merit are recorded in the Current-Voltage characteristic of the photovoltaic device and are applicable to both inorganic and organic photovoltaics. Power conversion efficiency is defined as

$$\eta_p = FF \cdot V_{oc} \cdot J_{sc}/P_{incident}. \tag{1.2}$$

Significant research has been devoted to discovering the theoretical limits to OPV device efficiency. Models for charge transfer conclude that there is a compromise between tailoring the donor/acceptor films to simultaneously maximize V_{oc} and J_{sc}. V_{oc} can be maximized by increasing the difference between donor HOMO and acceptor LUMO. J_{sc} can be maximized by tuning the HOMO-LUMO optical band gap

to maximize absorption. Rand et al. calculated a maximum efficiency for organic heterojunction solar cells. [17] They optimized the donor/accepter optical excitation band gap (1.8 and 1.5 eV) and donor/acceptor alignment gap (1.1 eV), to reach a maximum efficiency of 7.9%. Based on more recent applications of the Shockley-Queisser limit to OPV, the limit for single junctions is about 11% and the limit for tandem architectures is 15%. [28]

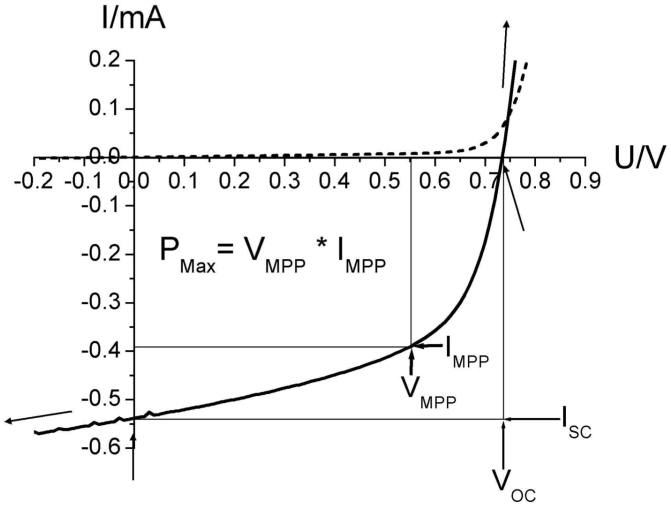

Figure 1.9: A current-voltage characteristic of a photovoltaic device. The definitions of Fill Factor, Open-Circuit Voltage, and Short-Circuit Current are shown. Reprinted (adapted) with permission from [11]. Copyright 2004 Cambridge Univ. Press.

The short-circuit current density, J_{sc}, is found by applying zero potential to the OPV device and recording the current (see Figure 1.9). In research environments, where OPV devices are commonly less than 1 cm^2 in area, current density is more valuable than short-circuit current, I_{sc}. The drift-diffusion current for electrons can be written as:

$$J_n = q\mu nE + q\mu \frac{kT}{q} \frac{\partial n}{\partial x} \tag{1.3}$$

which represents contributions from the electric field driven drift current and contributions from the diffusion current. The short-circuit current is limited by the organic

semiconductor material set. Maximum J_{sc} depends on the molecule's spectral absorption profile match to the incoming solar spectrum. [18, 29, 30].

The open-circuit voltage, V_{oc}, is found by illuminating the OPV device and recording the voltage at which current is equal to zero (see Figure 1.9). At the open-circuit voltage the energy diagram flat band condition is reached. Based on traditional silicon solar cell theory, the open-circuit voltage can increase linearly with the band gap of the cell material. However, in heterojunction devices with organic materials of large band gaps (2 - 3 eV) the open-circuit voltage is usually (0.5 - 1 V). Open circuit voltage is not simply a function of the work functions of the metals at the electrodes. Maximum V_{oc} is constrained by the energy difference between the highest occupied molecular orbital (HOMO) of the donor and the lowest unoccupied molecular orbital (LUMO) of the acceptor. An equation for the maximum open-circuit voltage was developed by Rand et al.:

$$qV_{OC}^{max} = IP_{donor} - EA_{acceptor} - \frac{q^2}{4\pi\epsilon_0\epsilon r r} \tag{1.4}$$

where ϵ_0 is the vacuum permittivity, ϵ_r is the relative dielectric constant of the organic materials, and r_{DA} is the physical separation of the optically generated hole/electron pair in the donor/acceptor films after charge transfer. [17] The third term accounts for loss to binding energy of the dissociated electron-hole pair.

Fill factor (FF) describes the efficiency of charge extraction in the photovoltaic device and is defined as

$$FF \equiv (J \cdot V)_{mpp}/J_{sc} \cdot V_{oc} \tag{1.5}$$

where *mpp* indicates the maximum power point (see Figure 1.9). The maximum power point (MPP) is found by maximizing the quantity of electrical power, $P = IV$. Due to nonidealities in the photovoltaic device, the maximum current/voltage power point is less than maximum V_{oc} and J_{sc}. FF is therefore determined by the percentage of charge carriers (electrons or holes) which reach the electrodes as the external voltage increases and the build-in field decreases. The charge carrier drift

distance is dependent on carrier lifetime τ and the carrier mobility μ: $d = \mu \times \tau \times E$ where E is the electric field. The fill factor can be increased with materials with large $\mu \times \tau$ products in order to decrease the d dependence on electric field. For high fill factor the shunt resistance must be very large to prevent leakage current and the series resistance must be very low. "Shorts" in the OPV device are a primary cause of decreased shunt resistance.

External quantum efficiency (EQE) is defined as the fraction of incident photons that produce electrons at the device contacts,

$$EQE(\lambda) = SR(\lambda)\dot{hc}/q\lambda \tag{1.6}$$

where $SR(\lambda) = J_{sc}(\lambda)/\Phi(\lambda)$. In order to measure $SR(\lambda)$ we illuminate the OPV with a programmable monochromator with a calibrated intensity. Internal quantum efficiency (IQE) is distinguished from EQE by removing the effect of photon absorption. IQE is defined as

$$IQE(\lambda) = \frac{EQE(\lambda)}{1 - T(\lambda) - R(\lambda)}. \tag{1.7}$$

1.3.4 PV Performance Limits

In this section we discuss the theoretical performance limits and nonidealities of photovoltaic devices. Ideally, all photons with energy above the semiconductor band gap are absorbed and converted into electron-hole pairs. Therefore, the maximum short-circuit current, J_{sc}, is achieved when the band gap is lower than the majority of the AM 1.5 solar spectrum. For the ideal p-n junction photovoltaic device, the V_{oc} is given by

$$V_{oc} = \frac{kT}{q} ln(\frac{I_L}{I_0} + 1) \tag{1.8}$$

where I_L is the light-generated current and I_0 is the diode saturation current. By minimizing I_0 the V_{oc} is maximized; for silicon, the maximum V_{oc} is about 700 mV. The maximum power conversion efficiency is strongly influenced by the band gap of the absorber. Using the AM 1.5 solar spectrum, a maximum efficiency of 33.7%

is possible with an ideal band gap of 1.34 eV. The maximum efficiency for mono crystalline silicon, which has a band gap of 1.1 eV, is 29%. The limit of photovoltaic power conversion efficiency is further described by the Shockley-Queisser limit.

In 1961, Shockley and Queisser developed an upper theoretical efficiency limit for single p-n junction photovoltaic devices based on solar blackbody radiation and a unity rate of radiative recombination. [31] This limit is now known as the "Shockley-Queisser limit," or "SQ limit." The detailed balance limit describes a relationship between the upper theoretical limit of power conversion efficiency depending on semiconductor bandgap. The SQ limit assumes that all photons above the bandgap are absorbed, 100% efficiency of charge extraction, and unity radiative recombination. The power of incoming photons is divided into the following: power converted into electricity; power of below-bandgap photons, which pass through the photovoltaic and aren't absorbed; excess photon energy above the band gap, which is emitted as phonons; decreased current due to electron-hole recombination at the maximum power point; and decreased voltage at the maximum power point. When highly energetic photons interact with the semiconductor and an electron/hole pair is excited, the electron and hole relax to the band edges and emit phonons. The extra energy in this process is lost. This effect limits the maximum efficiency of a single junction to about 44%. [32] Silicon photovoltaics, with a bandgap of 1.1 eV, have a maximum efficiency of 29% and have demonstrated efficiencies approaching 25%. [33] The SQ limit applies to organic photovoltaic devices; however, modifications to the theory are required.

Organic photovoltaic device physics has several departures from the physics assumed in calculating the SQ limit. The exciton binding energy and band offset necessary to dissociate excitons, create a fundamental loss in OPV devices, compared to inorganic PV. [34] OPV devices have large internal nonradiative recombination, which can be observed in photoluminescence quenching in organic heterojunctions. [35] The charge carrier mobility in organic semiconductors is generally lower than mobility

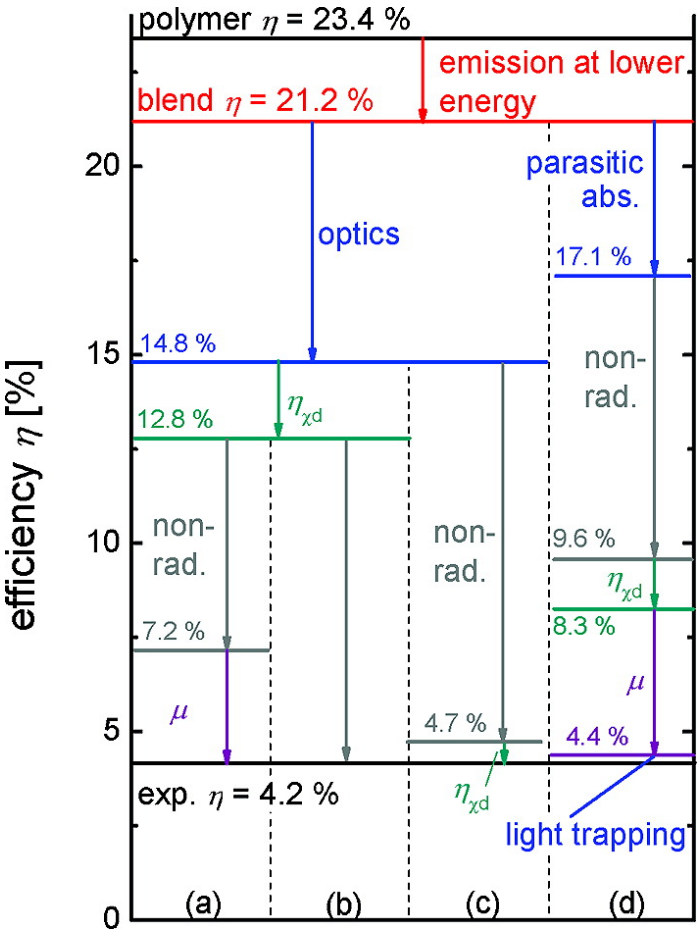

Figure 1.10: Comparison of efficiency loss factors for OPV devices based on the Shockley-Queisser limit. The subfigures a-d propose various combinations of loss mechanisms to explain the 4.2% power conversion efficiency of a sample PF10TBT/PCBM device. Reprinted with permission from [34]. Copyright 2009 American Chemical Society.

in silicon. Therefore the SQ limit assumption of perfect charge collection is not valid. [36] Several other loss mechanisms prevent OPV devices from reaching the SQ limit, shown in Figure 1.10. Exciton dissociation may not be a unity process. Electrons and holes may recombine nonradiatively at interfaces, defects within the bulk films and at the contacts. Kirchartz et al. estimated that non radiative recombination at the donor/acceptor interface decreased the limit of power conversion efficiency by

around 8% points. [34] However, quantum efficiencies close to 100% have been demonstrated. [37] Finite mobility in OPV devices causes up to an approximately 3% point drop in maximum efficiency. Based on the optical properties of photovoltaic polymers, the estimated SQ radiative efficiency is in the range of 21-23%. [34] In a similar study, Ameri et al. investigated the SQ limit for OPV devices starting from a theoretical device at 30.1% efficiency. [28] They proposed limitations for an OPV device with the ideal band gap of 1.5 eV and LUMO-LUMO offset of 0.3 eV. Based on exciton dissociation, charge carrier transport losses, and non-unity external quantum efficiency, Ameri et al. more conservatively estimated the current material sets could achieve practical efficiencies of around 11%.

Several methods have been proposed to exceed the SQ limit. Multijunction OPV devices increase the efficiency limit by introducing multiple absorber bandgaps. Two junctions can achieve a maximum efficiency of 42% while three junctions can achieve 49%. [28] Several studies have demonstrated photovoltaic devices with multiple-exciton generation. In a 2006 study Schaller et al. demonstrated the use of semiconductor nano crystals to to produce up to seven excitons from a single photon, corresponding to a 700% photon-to-exciton conversion efficiency. [38] Congreve at al. demonstrated external quantum efficiencies above 100% via singlet exciton fission, in which multiple excitons are generated when a single high-energy exciton is converted. [39]

1.3.5 OPV Equivalent Circuit

A simplified equivalent circuit diagram (ECD) for OPV devices is shown in Figure 1.11. The current source I_L is the photogenerated current when the OPV is illuminated. The diode current I_d counteracts the photogenerated current. The shunt current I_{sh} occurs due to parasitic conduction in the device. The net current is $I_{sc} = I_L - I_{sh} - I_d$. Other terms included in the ECD are series resistance (R_S) and shunt resistance (R_{SH}). Series resistance is a combination of material resistivity,

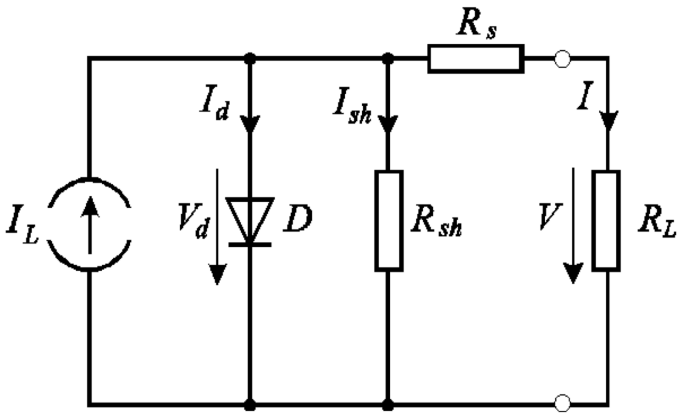

Figure 1.11: Photovoltaic equivalent circuit diagram. Reprinted from [40]. Copyright 2000 Cambridge and Graz.

electrode resistivity, and metal-organic interfaces at the electrodes. A low shunt resistance corresponds to leaks and shorts in the diode. When shunt resistance is low, the V_{oc} is often reduced; we often measure "shorted" devices with low V_{oc} and high I_{sh} when we fabricate OPV cells.

1.4 Organic Light Emitting Diodes

Organic light emitting diodes (LEDs) are a subset of organic diodes which emit light. OLED displays have been commercialized by a variety of electronics manufacturers. There is also interest in white OLEDs as an efficient solid-state lighting source. [41] In 2009 Reineke et al. reported a white OLED with a power efficiency of 90 lmW^{-1}, higher than the 60-70 lmW^{-1} commonly found in ubiquitous fluorescent tubes. [42]

1.4.1 Device Physics

OLEDs based on organic injection type electroluminescence (EL) were pioneered in the 1950's and 1960's. [43] OLEDs were eventually reduced from large crystals down to thin organic films formed by thermal evaporation. The reduced thickness of films en-

abled sufficient electric fields for electroluminescence with much lower voltages. Tang et al. introduced the multi-layer OLED in 1987 with improved charge balance. [9] The multi-layer OLED structure combines a hole-transporting layer and an electron-transporting layer with at least one transparent electrode. The brightest OLEDs occur when there is equal hole and electron density at the interface. The mechanism of light generation is recombination luminescence. For example, in Alq3-based devices, this film simultaneously transports electrons and emits.

For EL to occur, electrons and holes have to recombine and form an exciton, which then decays radiatively. In Alq3-based devices, the charge carrier mobility is higher in the hole-transporting layer than the electron transporting layer (Alq3). The lower ETL mobility causes most exciton recombination to occur with Alq3, where emission occurs. The recombination process creates excitons into two states: 75% into a triplet and 25% into a singlet state. Therefore, early OLED devices that only emitted via singlets were capped at a maximum 25% internal quantum efficiency. Baldo et al. later introduced an electrophosphorescent material to harvest the triplet state in phosphorescent OLEDs. [44] OLED devices with nearly 100% internal quantum efficiency, which would indicate complete triplet and singlet exciton decay, have been demonstrated. In Figure 1.12a and 1.12b we show two structures for fluorescent and phosphorescent emitting OLEDs.

1.4.2 OLED Device Structure

A sample band structure, ignoring band adjustments at constants, for an electrophosphorescent device is shown in Figure 1.13. In the sample band structure, α-NPD is used to transport holes from the ITO anode to the luminescent layer. The luminescent layer consists of $Ir(ppy)_3$ in CBP. In many EL OLEDs, Alq_3 is used as a green emitter, while in this phosphorescent OLED $Ir(ppy)_3$ is a green emitter or BDASBi and PEBA can be blue. Red emission has been demonstrated using the phosphorescent emitter $IR(MDQ)_2(acac)$ doped into an α-NPD host. [45] BCP is used as an exciton

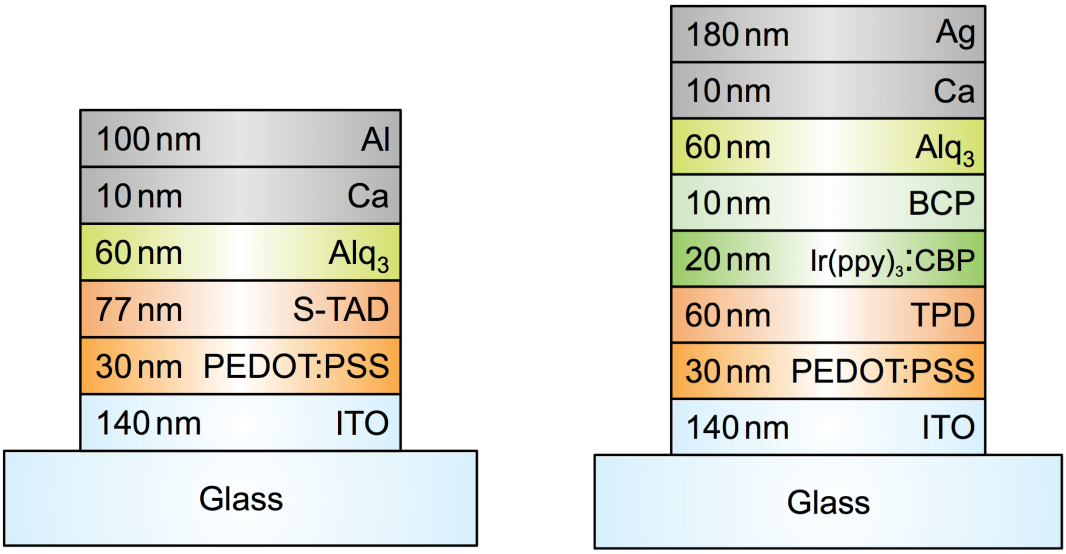

(a) **(b)**

Figure 1.12: Structures for fluorescent and phosphorescent OLEDs. From [45]. Copyright 2013 physica status solidi (a).

blocking layer to confine excitons created at the α-NPD/Ir(ppy)$_3$ interface. Excitons might otherwise reach Alq$_3$ and emit within that layer. In this OLED device the Alq$_3$ layer is the electron transport material. MgAg forms the electron-injecting cathode. The OLED anode must have a high work function to be able to inject holes. The OLED cathode must have a low work function to inject electrons. OLED cathodes are chosen with similar considerations to those used in OPVs, as shown in Table 1.2, namely work function, morphology, and stability.

Charge injection occurs when electrons transfer from the metal to the LUMO of the semiconductor. Injection energy barriers occur when there is a difference between the Fermi energy level of the electrode and the transport level in the organic semiconductor. The energetics of metal-semiconductor junctions have been a subject of great research. After deposition of organic molecules on metal electrodes the work function of the contact undergoes a change called the "vacuum-level shift," also referred to as an interface dipole. In some cases the shift in work function increase the injection

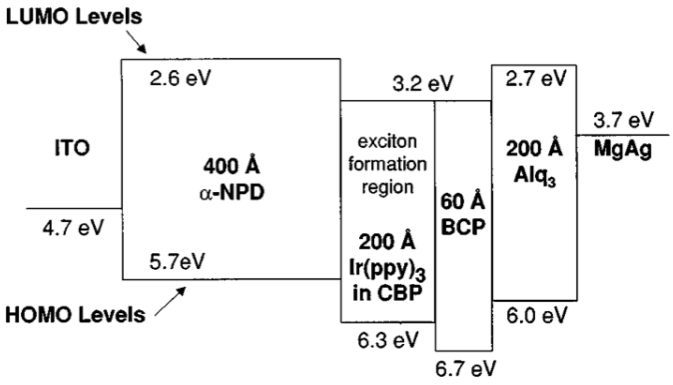

Figure 1.13: Band structure for the POLED device with triplet exciton harvesting by Baldo et al. Reprinted (adapted) with permission from [44]. Copyright 1999 AIP Publishing, LTD.

barrier height, which may hinder OLED performance. One example of this effect is the shift of Au's work function from 5.1-5.4 eV in UHV to 4.5-4.9 eV after exposure to lower vacuum levels or ambient environments. [46] Molecules deposited on the Au surface cause a shift in energy level. In another example, indium tin oxide (ITO) is a common transparent anode material in OLED devices. The work function of ITO can be shifted to lower the hole injection barrier by surface treatments such as UV/ozone and oxygen plasma. [46] The work function of the ITO anode can also be favorable shifted downward by coating with polymers such as PEDOT:PSS.

In 1995 Ettedgui et al. proposed a model for band bending modified tunneling at the interface between metals and organic polymers. [47] After the metal contacts the polymer, charge transfer and equilibration of the Fermi levels cause a built-in electric field to form. When the applied voltage increases above the built-in field, charge injection occurs via tunneling.

Additional insertion layers are commonly added between the organic semiconductor and contact to improve charge injection. Ultrathin ($\sim$ 1-5 nm) electron injection layers such as LiF and MgO can reduce the barrier between cathodes and the organic LUMO level. [48] Low work function metals are good cathodes in OLED devices be-

cause they can easily inject electrons; however, these metals are often less stable, which reduces device lifetime as the metal oxidizes. The work function of LiF may be as low as 2.9 eV while previous metals had higher work functions: Al (4.28 eV), Mg (3.66 eV). [48] In the study by Hung et al., the report concluded that LiF caused the adjacent Alq_3 band to bend down by more than 1 eV, reduce the barrier between the Fermi level of Al and the LUMO level of Alq_3. By reducing the electron insertion barrier, the drive voltage of the OLED device (at 100 mA/cm^2) was reduced from 13-17 V with MgAg and Al cathodes to 10 V, which results in higher electroluminescence efficiency.

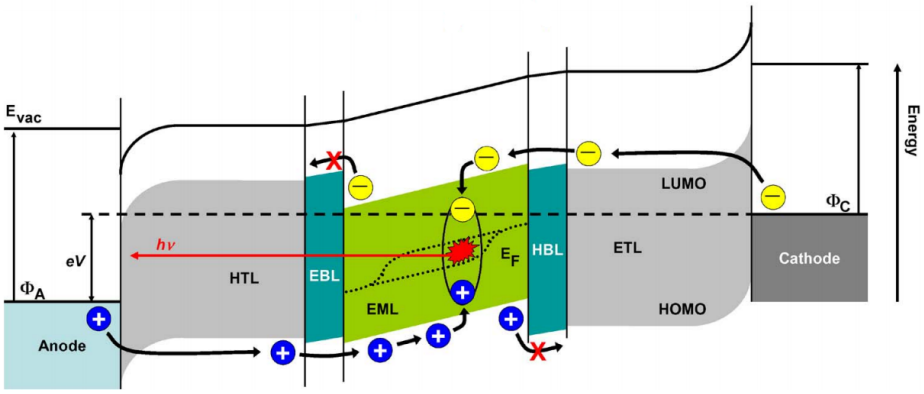

Figure 1.14: Schematic energy diagram of a p-i-n OLED device under operation. From [49]. Copyright 2009 IEEE.

The OLED band diagram shown in Figure 1.14 includes the previously discussed energy band bending at contacts, energy level shift under applied bias, and intermediate bands within the emissive layer. [49] Holes and electrons are injected to the LUMO and HOMO levels of the ETL and HTL through thin layers via tunneling. The energy level gap from the emissive layer to the EBL prevents electrons from reaching the HTL, where they might recombine with holes within the HTL or at the anode. The HBL functions similarly to prevent holes from entering the ETL. The hole and electron form a bound excitonic state with the emissive layer which has energy levels below the LUMO and HOMO due to the binding energy. Photon emission

occurs through the transparent anode. The EBL and HTL are ideally wide bandgap materials that do not absorb emitted photons.

1.4.3 Evaluating OLED Performance

I-V characteristics are important to understand the turn-on voltage of OLED devices. I-V curves are taken with a source-measurement unit. Luminance-Voltage characteristics are taken using a calibrated photodiode. OLEDs are measured with spectrometers to characterize the emission spectrum. Finally, quantum efficiency is an important cell engineering metric. Internal quantum efficiency refers to the number of photons created for each electron-hole pair injected at the electrodes. With the introduction of phosphorescent OLEDs that capture triplet emission, internal quantum efficiency can approach 100%. External quantum efficiency (EQE) is the number of photons that emit from the OLED for each electron-hole pair injected at the electrodes. Photons generated within the emissive layer often couple to surface plasmons, emission to the substrate, waveguide modes, internal absorption, and emission to air. [45] Emission to air, which is equivalent to EQE, is often 10-20%. Improving the EQE (emitted light) of OLEDs is a topic of significant research.

1.5 Graphene

Graphene is a two-dimensional crystalline form of graphite, made up of a hexagonal lattice of carbon atoms. Graphite was previously known in its other dimensional forms: in 0D as fullerenes like C_{60}; rolled into 1D nanotubes; or in the bulk 3D form of graphite. The first 2D sheets of graphene were isolated by Novoselov and Gaim. in 2004 [51, 52]. A schematic image of graphene's 2D "honeycomb" structure is shown in Figure 1.15. Graphene has since garnered widespread interest for its excellent electrical [50, 53–56], mechanical [57–59], and optical [60] properties. Charge carriers can travel thousands of interatomic distances in graphene without scattering.

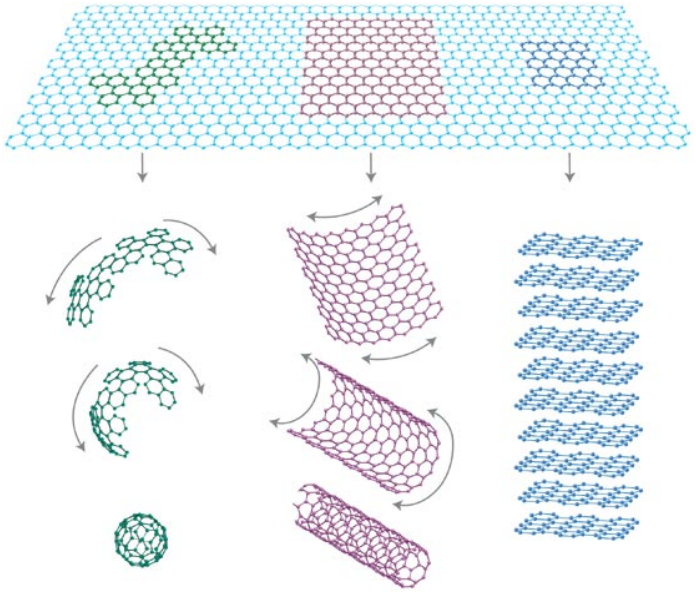

Figure 1.15: Three dimensionalities of 2D graphene films: 0D fullerene C_{60}, 1D nanotube, and 3D graphite. From [50]. Copyright 2007 Nature Publishing Group.

1.5.1 Graphene Electrodes for Organic Electronics

Graphene is a promising flexible, highly transparent, and elementally abundant electrode for organic electronics. Recent work shows that graphene can be grown in large areas with roll-to-roll fabrication [61] and used as a transparent and flexible electrode for organic optoelectronic devices. [59, 62, 63] Graphene is an improvement over current top-electrodes because it is highly transparent, compatible with roll-to-roll processing, and avoids plasma sputtering. [64–66]

The current standard for transparent electrodes is indium tin oxide (ITO). ITO electrodes commonly have sheet resistances less than 100 $\Omega\ \square^{-1}$, optical transmission of about 90%, and practically unlimited scalability. These properties have made ITO the predominant transparent conductor in the display and microelectronics industry. The disadvantages to ITO are the low-throughput, expensive process, poor flexibility of ITO films, and limited integration on top of organic electronics. ITO is a difficult material to deposit on top of organic electronics because it diffuses into the relatively

soft active layers, which alters the energy band structure of the organics. [67]

There are recent reports that graphene can replace ITO transparent anodes for organic optoelectronics devices such as OLEDs and OPVs. Recently, graphene devices have been demonstrated to have similar quality as ITO-based devices in an OLED device [68] and an OPV device. [67] In 2010, Bae et al. introduced large area, roll-to-roll graphene production with single-layer sheet resistances as low as 125 $\Omega\ \square^{-1}$ and 97.4% optical transmission. Multi-layer graphene films were recorded with sheet resistances as low as 30 $\Omega\ \square^{-1}$ and 90% optical transmission. [61] Multi-layer graphene films have similar optical transparency and lower sheet resistance than ITO, and therefore are an eligible replacement. However, there is much work yet to be done to increase the ability to integrate high-quality graphene with organic electronics. In order to take advantage of graphene's properties as a transparent electrode for organic optoelectronic devices, we must solve the problem of integrating large-area CVD graphene with organic thin-films.

1.5.2 Graphene Electrode Physics

Graphene is a zero-bandgap semiconductor with a density of states equal to zero at the Dirac point. Graphene has a linear dispersion relation with Dirac fermions of zero effective mass. In order to improve the conductivity of graphene, the density of states must be adjusted by shifting the Fermi level away from the Dirac point. The highest attained room temperature mobility of exfoliated and chemical vapor deposition (CVD) grown graphene is in the range of 45-60,000 $cm^2V^{-1}s^{-1}$. [69, 70]

In order to use graphene as an electrode for organic electronics, the work function must have a good match to the HOMO/LUMO level of the organic semiconductor to form an ohmic contact. The work function of graphene can be affected by chemical substitution, electric field, and contact doping. Chemical substitution changes the work function of graphene by substitution dopant atoms such as B or N in place of carbon during synthesis. [71] Electric fields can alter the graphene fermi level by up to

0.2 eV. [72] Contact doping can shift the graphene fermi level by up to 0.5 eV. [73] In a previous study by Jo et al., the work function of an untreated multilayer graphene film was found to be 4.58 ± 0.08 eV. [74] Interfacial layers can form interfacial dipoles which alter the graphing work function by 0.05 to 0.33 eV. The graphene work function was decreased by 0.33 eV to 4.25 eV by adding a WPF-6-oxy-F interfacial dipole layer; the decrease in work function enabled the use of graphene as a cathode for an OPV device. Nitric acid, HNO_3, is an effective p-dopant for graphene films, which can shift graphene's work function by 0.13 eV. [61]

1.6 Objectives and Approach

This thesis concentrates on advancing the field of organic photovoltaics by investigations of photogenerated charge collection and optimization of optical absorption, and the overall field of organic electronics by investigating the integration of graphene electrodes in organic optoelectronic devices.

Chapter 2

Nanostructured Electrodes Improve the Fill Factor of Organic Photovoltaics

2.1 Introduction

In this chapter we discuss improvements to OPV fill factor by inserting sub-optical-wavelength nanostructured electrodes (NEs). The new electrode design improves FF without compromising open-circuit voltage or short-circuit current. We attribute this improvement to efficient charge collection by the NEs, which reduce recombination in low-mobility organic semiconductors. NEs increase the fill factor of planar heterojunction devices with boron subphthalocyanine chloride (SubPc)/C_{60} from 28% to 40%. Electrical characterization and optical measurements indicate that NEs compensate for reduced material volume and improve charge extraction in materials with low mobility. Our findings suggest that NEs can be optimized for a given material set to improve fill factor performance, which is important for improving organic photovoltaic power conversion efficiency.

One reason OPV power conversion efficiency is low is due to low fill factor. OPV

often have poor fill factor (FF) due to low charge carrier mobility and high bimolecular recombination rates. Improving FF is important because power conversion efficiency,

$$\eta_p = FF \cdot V_{oc} \cdot J_{sc}/P_{incident} \tag{2.1}$$

is directly proportional to FF.

2.1.1 Recombination and Charge Transport in OPV Devices

Improving performance of heterojunction OPV devices is possible by understanding the recombination mechanisms. Geminate pair recombination describes the recombination of an electron-hole pair at the D/A interface after dissociation. The electron-hole pair have a Coulombic attraction, which drives recombination. Interface recombination may also occur at defects and trap states at the D/A interface. If the geminate pair (exciton) successfully dissociates, the electron-hole pair have remaining recombination mechanisms via bimolecular recombination, defects, and traps. Bimolecular recombination occurs when electrons traveling through the donor, that remain near the D/A junction, recombine with holes in the acceptor. Bimolecular recombination is particularly harmful in BHJ devices which have a high interfacial area. Bimolecular recombination is caused by low mobility and traps. Clarke et al. found that polymer:fullerence BHJ OPV devices had localized trap states which increased recombination. [75] They found that the trap state density was approximately $7 \cdot 10^{17}$ cm^{-3} and could eventually be filled by increasing illumination intensity.

While the recombination mechanisms in organic photovoltaic devices share some similarities with inorganic devices, differences in mobility, bound state energetics, and impurities merit additional study. Organic photovoltaics are majority carrier devices, while inorganic photovoltaics are minority carrier devices. In inorganic PV cells, both electrons and holes travel through the same bulk material and have many opportunities to recombine. After exciton dissociation in OPV cells, the separated electron/holes travel through respective accepter/donor layers. In the ideal case, these

charge carriers do not encounter opposite charges with which they can recombine. The majority of recombination occurs at interfaces as bimolecular recombination. [76] However, in real-world OPV devices the semiconductor material purity is less than 100%, which creates the opportunity for trap-assisted recombination.

Impurities play a primary role in the OPV recombination process. Research-grade OPV materials are often available in purities of 95-99.9% and better. Further purification via vacuum sublimation can achieve purities above 99.99%. Trap states in the OPV devices affect performance via several routes: Photons may be absorbed directly into the bandgap formed between trap and HOMO level. Second, excitons may dissociate at the interface between bulk material and trap. Third, mobile charge carriers in the bulk may be trapped by impurities. [77] Once the charges are trapped they may recombine to the ground state or de-trap to the LUMO level with energy from photons or phonons.

2.1.2 OPV Fill Factor

FF performance is one of the primary challenges facing OPV because most organic semiconductors have poor charge mobility [78, 79]. OPV devices often have FFs of 40-60% while traditional silicon devices have FF >80% due to high minority charge carrier mobility and long minority carrier lifetime which enables carrier diffusion lengths up to $\sim$ 400 microns [33, 80]. Donor materials used in OPVs such as boron subphthalocyanine chloride, squaraine, and MDMO-PPV have hole mobilities in the range of $10^{-5} - 10^{-8}$ $cm^2V^{-1}s^{-1}$, which are much lower than the electron mobility of the common acceptor material C_{60}, $\sim 10^{-2}$ $cm^2V^{-1}s^{-1}$ [81–84]. Recombination increases and FF decreases when organic semiconductor films are thicker than the donor/acceptor (D/A) carrier diffusion lengths [18]. The performance is limited by the lower mobility among the two materials, which means that extraction of the holes is a priority for improving the cell [83, 85].

In a previous study of imbalanced mobility by Tress et al., the investigators note

that poor FF associated with an "S-shaped" kink in the IV curve is a result of poor transport of free charge carriers. [86] For balanced, high mobility materials, the charge carriers are all extracted. In low mobility materials, a space charge region builds up in the device, increasing electron/hole concentration near the D/A interface where bimolecular recombination occurs. Previous investigations have improved OPV FF through balancing the electron and hole mobilities. Chen et al. increased the FF and J_{sc} of a CuPc/C_{60} OPV by doping the low-mobility CuPc with high-mobility pentacene in order to improve hole extraction in the donor [87]. Li et al. showed that FF was maximized by optimizing the BHJ mixing conditions to achieve an electron/hole mobility close to unity [88]. Previous investigations have improved OPV FF by modifying material crystallinity, introducing conductive molecules, and modifying organic-electrode interfaces [89–92].

Though the previous studies demonstrate increased FF, a universal, material-agnostic technique to improve charge collection efficiency would benefit the majority of OPV devices. Ray et al. previously developed simulations revealing the potential for optimized nanostructured electrodes (NEs) to increase OPV FF [85]. In this investigation we integrate an innovative device structure that improves OPV FF through the implementation of optimized NEs.

Nanostructured three-dimensional electrodes improve effective mobility in organic films by providing efficient hole- or electron- collection paths within donor and acceptor films, respectively [85]. Structured electrodes and inserted conductive nanostructures have previously been shown to improve optical absorption and electronic transport in OPV devices. Textured and photonic crystal electrodes can increase OPV light-trapping, which increases J_{sc}, but do not improve charge collection efficiency within semiconductor films because the electrode pitches are too large [93–95]. Nanostructured electrodes that improve light trapping have been investigated and may enable ultra-thin OPV devices with high FF and J_{sc} [96]. Inserted nanostructures must be sufficiently small, in the subwavelength scale, to improve charge carrier

transport in organic semiconductors.

Several groups have previously investigated conductive nanostructures in OPV. Dispersed carbon nanotube NEs improve effective mobility in organic bulk heterojunction cells [90]. Confined NEs fabricated using templating achieve improved bulk heterojunction OPV charge transfer [97]. Additional studies of embedded conductive NEs were shown to improve FF [98–101]. Without careful control of dimensions, conductive nanostructures can decrease FF by decreasing shunt resistance and cause shorts through the D/A films [102]. In this paper we demonstrate optimized NEs, which are designed to maximize FF for a small-molecule OPV material set.

2.2 Results and Discussion

2.2.1 Simulation and Theory

Ray et al. investigated optimal NEs for OPV devices via opto-electronic simulations and found that NEs improve carrier extraction efficiency when added to planar heterojunction devices [85]. The simulation equations and boundary conditions are listed in Figure 2.1. Nanostructured electrodes improve the performance of OPV devices by two primary means: First, the NE reduce the transit time between the heterojunction and the electrode, which increases FF. A schematic of these effects is shown in figure 2.3. The first effect mainly improves the FF performance under the maximum power point, when the effective electric field has decreased as the external voltage approaches V_{oc}. The second effect reduces charge carrier recombination in the bulk, causing an increase in J_{sc}.

Based on previous investigations by Ray et al., we developed a new electrode design for the SubPc/C_{60} planar heterojunction device. The design rules for inserted electrodes stipulate that the electrode pitch needs to be small - 100 nm or less - and the electrode height needs to be about half of the film thickness and contained within one material (Figure 2.2). NEs that cross the D/A junction decrease J_{sc} and FF

Optical Absorption:

$$F_{ph}(r) = \int \frac{A(\lambda, r) I_0(\lambda)}{hc/\lambda} d\lambda \quad (1)$$

Exciton Diffusion equation:

$$D_{ex}\nabla^2 n_{ex} = G_{ex}(r) - R_{ex}(n_{ex}) \;\; ; \quad R_{ex} = \frac{n_{ex}}{\tau_{ex}}; \; G_{ex} = \nabla F_{ph} \quad (2)$$

Poisson equation:

$$\nabla(\epsilon_r \epsilon_0 \nabla\psi) = -q(n_h - n_e) \quad (3)$$

Continuity equation:

$$\nabla J_{e,h} = \mp\left(G_{e,h}(n_{ex}) - R_{e,h}(n_e, n_h)\right) \quad (4)$$

Drift-diffusion equation:

$$J_{e,h} = \mu_{e,h} n_{e,h}(-\nabla\psi) \pm D_{e,h}\nabla n_{e,h} \quad (5)$$

Recombination equation:

$$R_{e,h}(n_e, n_h) = \gamma(n_e, n_h - n_{int}^2) \quad (6)$$

Electron boundary condition:

$$\nabla n_e|_{z=0} = 0; \;\; n_e(z = T_{film}) = N_c exp\left(-\frac{\Phi_c - LUMO_A}{kT}\right) \quad (7)$$

Hole boundary condition:

$$n_h(z = 0) = N_v exp\left(-\frac{\Phi_a - HOMO_D}{kT}\right) \;\; ; \nabla n_h|_{z=T_{film}} = 0 \quad (8)$$

Figure 2.1: The equations for carrier transport. Table adapted from Ray et al.'s investigation. [85] Image Copyright 2012 IEEE.

by introducing an electric field that causes local charge accumulation. The inserted electrode should be designed to collect holes in the donor material because mobility is generally lower in the donor film. While the inserted electrodes remove active volume from the OPV device, the current loss from the decreased volume is compensated by improved charge extraction, causing J_{sc} to increase by a small percentage.

Via the general PHJ design rules summarized in the previous study we simulated

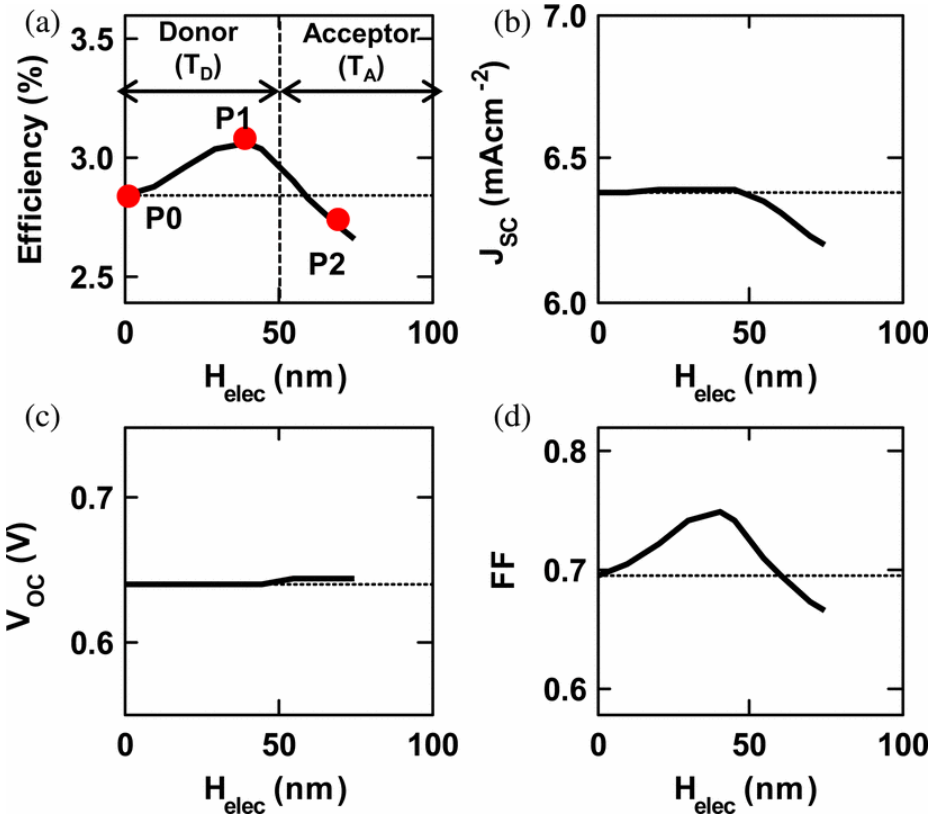

Figure 2.2: The effect of inserted electrode height on the performance of a planar heterojunction OPV device. (a) Power conversion efficiency, (b) Short-circuit current, (c) Open-circuit voltage, (d) Fill Factor. Figure adapted from Ray et al.'s investigation. [85] Image Copyright 2012 IEEE.

and optimized an existing boron subphthalocyanine chloride (SubPc) / C_{60} planar heterojunction device. The device structure is shown in Fig. 2.11. We fabricated planar devices in order to create a table of known material and device parameters, shown in Figure 2.4.

Based on simulations, we fabricated an NE device with a 100 nm two-dimensional electrode pitch and a 30 nm electrode pillar height. The NEs are confined to the low-mobility SubPc donor film. Based on the NE dimensions, OPV structure, and material electrical and optical properties, the simulations predict that FF should increase from 33% to 47%, while maintaining similar V_{oc} and J_{sc}.

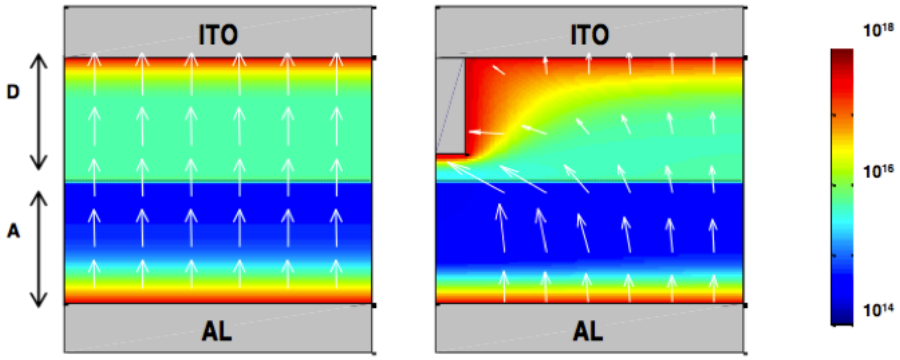

Figure 2.3: The effect of inserted electrode height on the electric field and carrier density. Figure adapted from Ray et al.'s investigation. [85] Image Copyright 2012 IEEE.

Parameter	Symbol	Numerical values
Exciton diffusion length	L_{ex}	15 nm
Electron mobility (C60)	μ_e	$10^{-3}\ cm^2V^{-1}s^{-1}$
Hole mobility (SubPc)	μ_h	$10^{-6}\ cm^2V^{-1}s^{-1}$
Bi-molecular recombination coefficient	γ	$10^{-9}\ cm^3/s$
SHR Rec. Time	τ_{SRH}	100 ns
Width of the D-A interface	W_{int}	2 nm
Lowest unoccupied molecular orbital (Donor)	$LUMO_D$	3.0 eV
Highest occupied molecular orbital (Donor)	$HOMO_D$	5.4 eV
Lowest unoccupied molecular orbital (Acceptor)	$LUMO_A$	3.7 eV
Highest occupied molecular orbital (Acceptor)	$HOMO_A$	6.1 eV
Effective density of states ($HOMO_D, HOMO_A, LUMO_D, LUMO_A$)	N_C	$10^{21}cm^{-3}$
Cathode work function (Al)	Φ_c	3.8 eV
Anode work function (Au)	Φ_a	5.1 eV

Figure 2.4: Experimentally measured and calculated simulation parameters for the SubPc/C_{60} based photovoltaic device.

2.2.2 Applicability to Bulk Heterojunction OPV

Simulations show that nanostructured electrodes will not improve the FF of bulk heterojunction (BHJ) OPV devices. In BHJ devices the donor/acceptor layers form a mixed active layer morphology. Therefore, the NE pillars will interact with the mixed D/A films in four ways, explained as B0 through B3 and shown in Figure 2.6. In con-

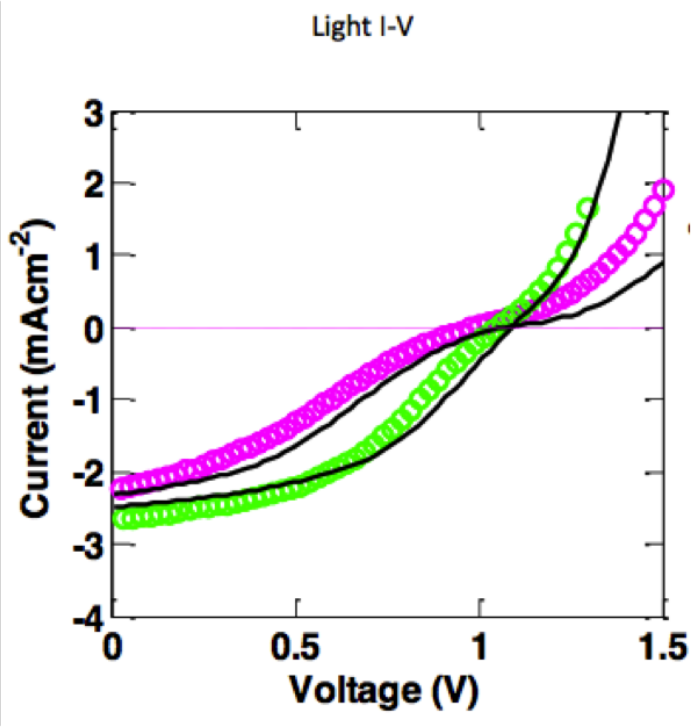

Figure 2.5: Simulated and experimental current-voltage characteristics of nanostructured electrode and planar electrode devices.

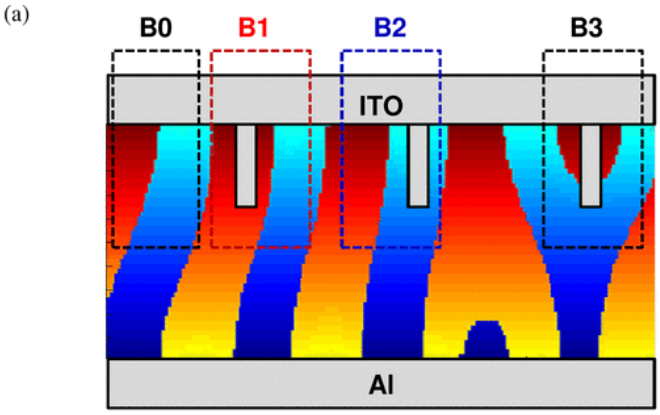

Figure 2.6: The effect of the NE on a typical BHJ OPV device morphology is divided into four cell structures: B0, B1, B2, and B3. [85] Image Copyright 2012 IEEE.

figuration B0, there is no NE and the device behaves like an ordered, vertical junction PHJ device. In configuration B1, the NE remains exclusively in the donor film and

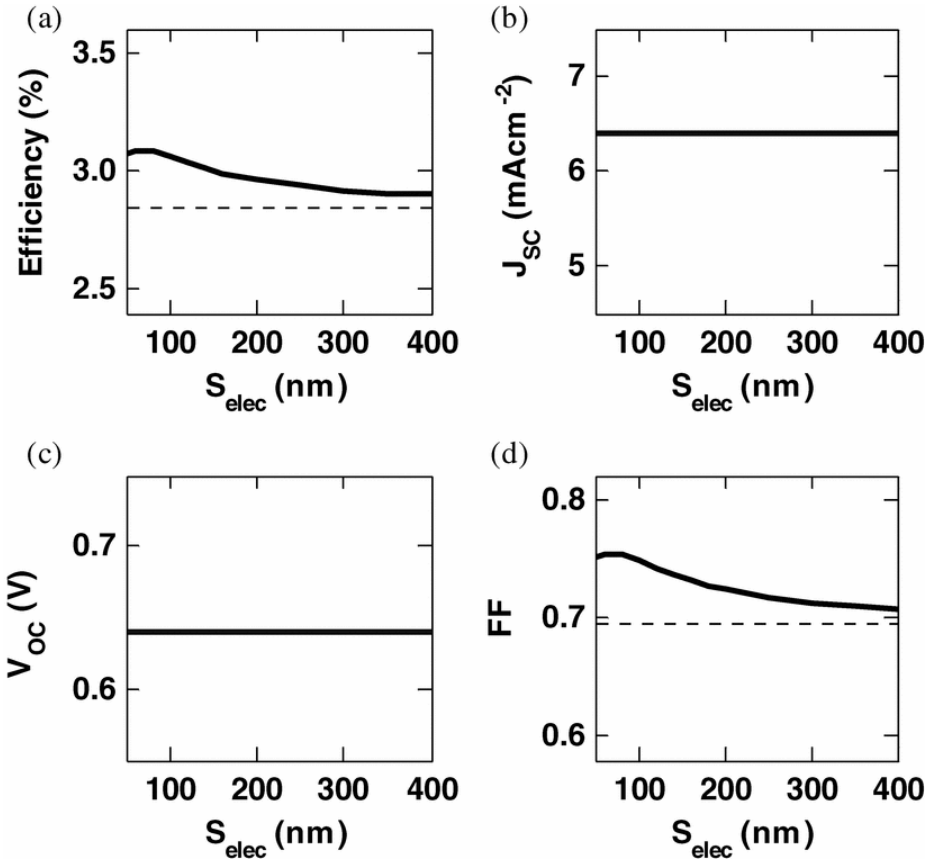

Figure 2.7: The effect of inserted electrode height on the performance of a bulk heterojunction OPV device. (a) Power conversion efficiency, (b) Short-circuit current, (c) Open-circuit voltage, (d) Fill Factor. Figure adapted from Ray et al.'s investigation. [85] Image Copyright 2012 IEEE.

will improve charge extraction from the low-mobility donor film. In configuration B2, the NE is confined to the acceptor film, which causes carriers to be extracted from the wrong electrode. In configuration B3, the NE crosses the donor/acceptor interface. This scheme corresponds to the situation shown in Figure 2.2, and causes decreased J_{sc} and FF; therefore, situation B3 is undesirable. The OPV performance is broken down by metric in Figure 2.7. In BHJ OPV some individual NEs will improve OPV performance while other NEs will degrade performance, therefore the overall efficiency cannot be significantly improved.

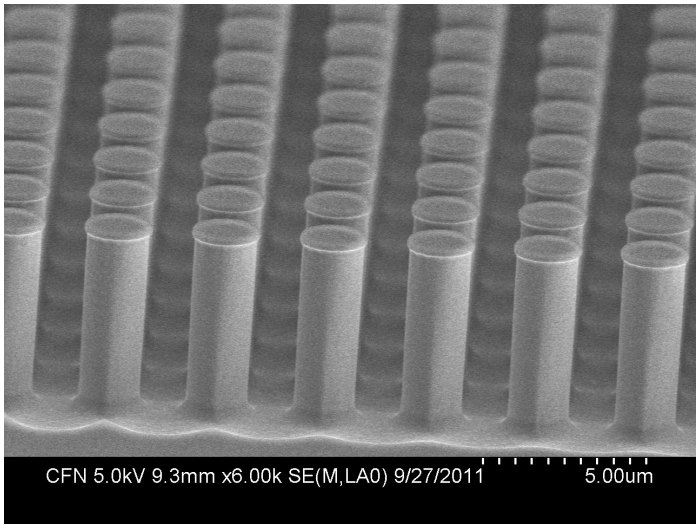

Figure 2.8: Silicon micropillars.

2.2.3 Fabrication

We initially began a study of etched Silicon nanopillar structures for photonics crystals, shown in Figure 2.8, which are micron-sized. We used electron beam lithography (EBL) to pattern polymer photoresist on Silicon and a cryogenic (-100°C) SF_6 ICP etch process. Later, we elected to fabricate smaller nano pillar structures for thin-film OPV. In an early attempt to produce large area nanostructured areas, we used EBL to fabricate insulating photoresist masks with vias to an ITO substrate, which we could then electroplate. Using this electroplating technique we hoped to achieve large area controlled growth of conductive Ag nanopillars. Unfortunately, we found that Ag nano pillar growth would either quickly grow out of control with poor uniformity (Figure 2.9a) or fill in the voids in a sparse pattern (Figure 2.9b). In order to fabricate the NE nanostructured pillars, we used EBL and switched to an (inductively coupled plasma) ICP reactive ion etching chemistry to produce fused-Silica nanopillars less than 50 nm in height. Using EBL and ICP etching, we achieved a high level of uniformity and reliability.

Fused-silica wafers were coated with 50 nm of ZEP520A electron-beam resist. 30

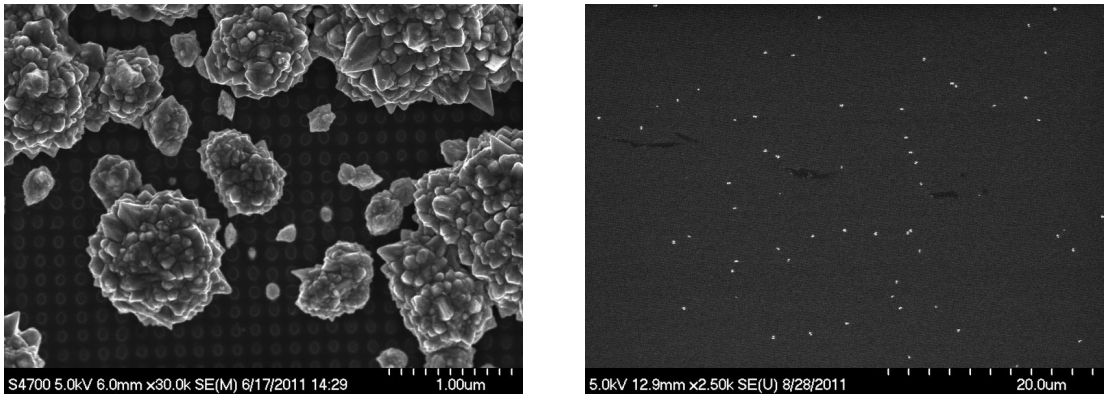

(a) **(b)**

Figure 2.9: Early attempts to fabricate nanostructured electrodes via Ag electroplating on ITO substrates, using an insulating photoresist mask with 20-50 nm vias. (a) SEM micrograph showing uncontrolled growth of Ag nanopillars out of some vias, but a complete lack of growth out of many vias. (b) SEM micrograph showing sparse growth of Ag nanopillars.

nm diameter single shot voids were exposed with a JEOL JBX-6300FS electron beam lithography system and developed. A 7 nm Cr film was thermally deposited, then lifted off for 1 hr at 60°C in Nano Remover PG to produce a Cr etch mask. The fused-silica pillars were etched in an Oxford Instruments PlasmaLab System 100 using a CHF_3 / O_2 chemistry. An advantage to this electrode fabrication process is that patterning is performed on standard fused-silica substrates before the deposition of organics or electrodes. A completed 4" wafer with 64 nanostructured OPV is shown in a photograph in Figure 2.10a. The 4" wafer will be diced into 16 substrates with four nanostructured OPV devices and four control OPV devices. An optical microscopy image of a single OPV area is shown in Figure 2.10b.

The OPV device consists of a planar heterojunction with a SubPc donor and C_{60} acceptor. SubPc/C_{60} based OPV have recently attained η_p of 4.5±0.1% [103]. SubPc has a high absorption coefficient of $\alpha^{-1} = 53.4$ nm, as measured in deposited films, broad visible absorption (Fig. 2.18) and a V_{oc} >1 V [104]. Both NE and planar

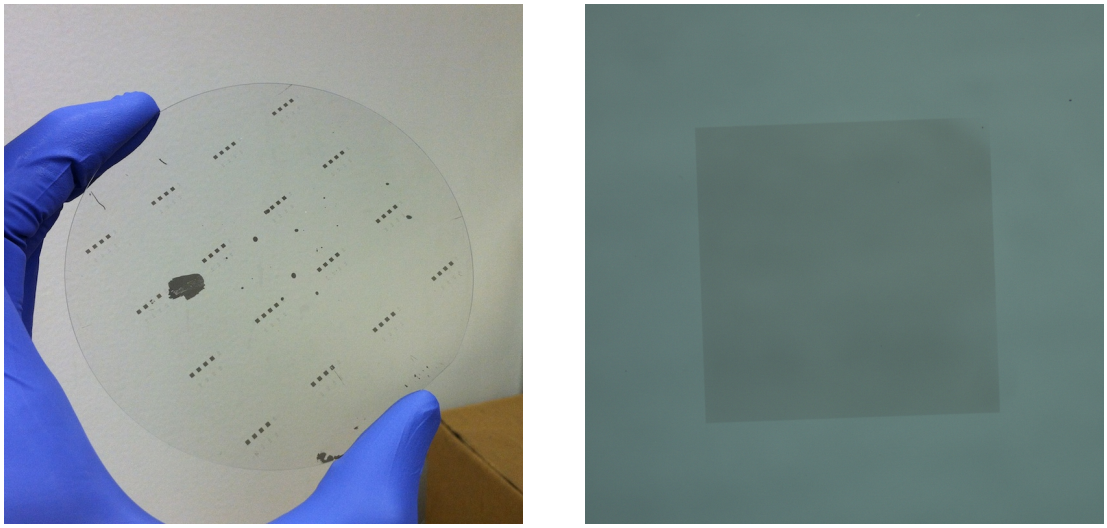

(a) **(b)**

Figure 2.10: (a) Photograph of a completed 4" fused-Silica wafer with 64 nanostructured OPV devices. Each nanostructured area is 1 x 1 mm. The wafer is diced into 16 individual substrates. (b) Optical microscope image of a single nanostructured area which is 1 x 1 mm.

electrode devices have identical electrode metals and active layer films: 3 nm Cr adhesion layer, 10 nm Au transparent anode, 5 nm MoO_3 (molybdenum oxide) hole injection layer, 40 nm SubPc electron donor, 40 nm C_{60} electron acceptor, 10 nm TPBi (2,2',2"-(1,3,5-benzinetriyl)-tris(1-phenyl-1-H-benzimidazole)) exciton blocking layer, and a 100 nm Al cathode [105] (Energy diagram in Fig. 2.12). The Cr/Au anode was deposited on a rotating stage to achieve a conformal coating of the nanostructured fused-silica pillars. The anode has a sheet resistance of 68 $\Omega\ \square^{-1}$. All electrodes, inorganic, and organic films were deposited by thermal physical vapor deposition using shadow masks. MoO_3, SubPc, C_{60} and TPBi were used as received from Luminescence Technology Corp. All depositions were performed at 1.0 Å sec^{-1} at less than $2 \cdot 10^{-6}$ Torr. The device area is 0.01 cm^2.

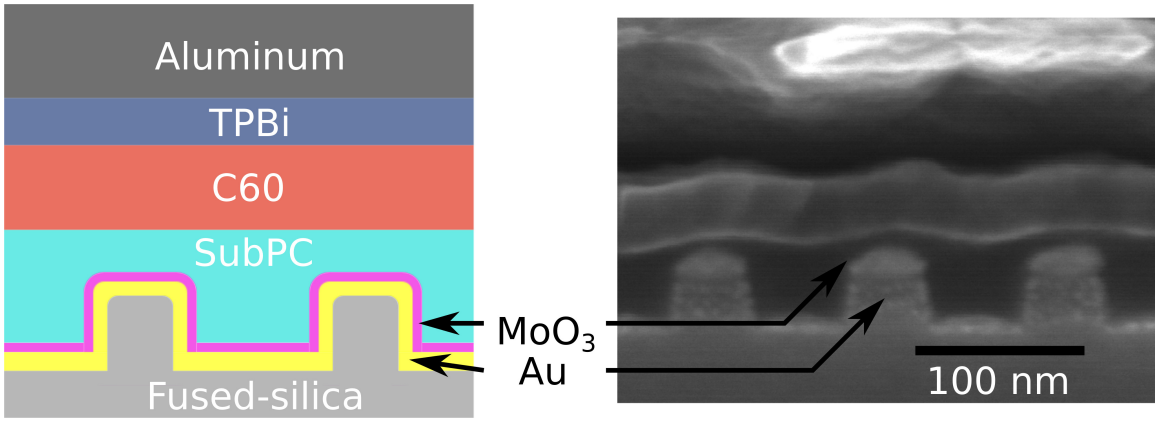

Figure 2.11: Left: Schematic of a nanostructured electrode device. Right: A cross-sectional SEM micrograph of a nanostructured electrode device. The scale bar is 100 nm.

Electrode	V_{oc} [V]	J_{sc} [mAcm^{-2}]	η_p [%]	FF [%]	R_{sh} [Ω cm^2]	R_s [Ω cm^2]
Planar	0.95 ± 0.09	2.48 ± 0.29	0.65 ± 0.06	28.0 ± 2.1	752 ± 106	27.4 ± 1.16
NE	1.01 ± 0.05	2.90 ± 0.22	1.12 ± 0.12	40.3 ± 2.7	1490 ± 203	4.16 ± 0.57

Table 2.1: Performance characteristics of NE and planar devices. Planar data is averaged over 12 identical devices. NE data is averaged over 9 identical devices.

2.2.4 Electrical Characterization

Experimental current-voltage (I-V) measurements show that NEs increase FF of the OPV from 28% to 40% (Fig. 2.13). Higher FF causes an improvement in average η_p from 0.65% to 1.18%. NEs also increase J_{sc} by an average of 17%. A summary of the NE and planar electrode device performance is listed in Table 2.1. J-V characterization is performed using a Keithley 2400 source meter and a Newport solar simulator with an AM1.5 global tilt filter in a N_2 environment. The dark current curves (Fig. 2.14) are taken in low-light conditions. The series resistance is calculated by taking the inverse slope of the linear portion of the light current curve at 2 V, well above V_{oc}, $R_S = (\frac{J}{V})^{-1}$. The shunt resistance is calculated by taking the inverse slope of

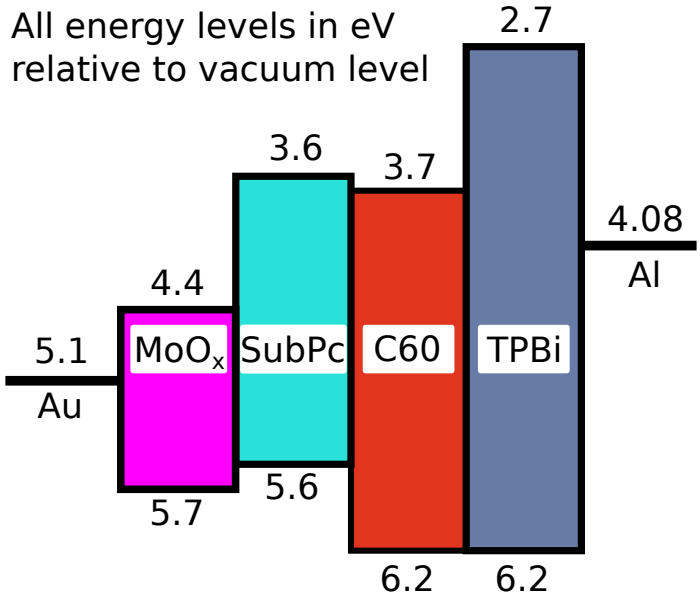

Figure 2.12: An energy band diagram for the OPV device. All energy levels are relative to the vacuum level and measured in eV [23, 104, 106].

the J-V curve at 0 V, $R_{sh} = (\frac{J}{V})^{-1}$ [107]. The S-shape of the light I-V curve results from a high series resistance.

EQE is 2% higher in the NE devices than the planar electrode devices over the wavelengths 300-650 nm (Fig. 2.15). The EQE spectra shown are averaged over two reference planar devices and two NE devices. Details of EQE measurements can be found in Appendix A. We conclude that the NE increases EQE as a result of improved charge collection efficiency and generates increased J_{sc}.

2.2.5 Optical Characterization

Optical absorption simulations show that NE devices do not significantly alter the device absorption profile or introduce any additional resonance peaks. The simulated absorption profiles of the NE and planar electrode devices are shown in Fig. 2.16. Simulations show that NE devices absorb 83% of the optical power of the planar device. The NE device absorbs less due to decreased material volume which is oc-

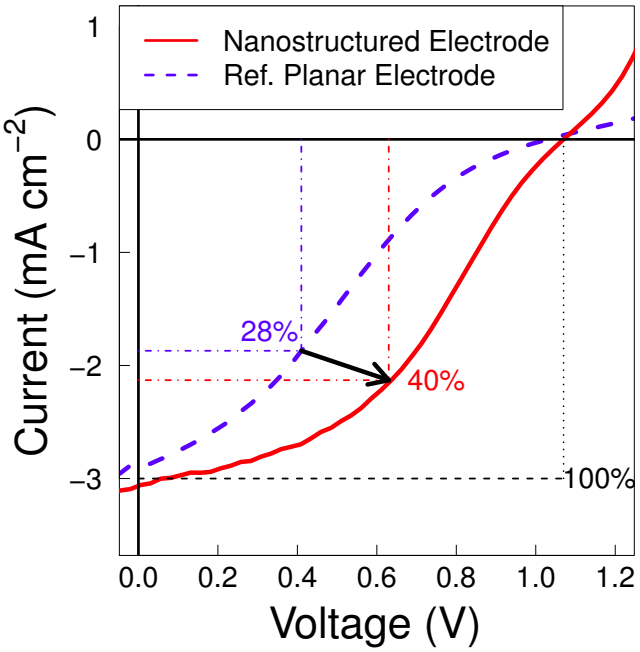

Figure 2.13: The measured J-V curve of a nanostructured electrode and planar electrode devices. The solid red line is the light current curve of the nanostructured electrode device. The dashed blue line is the light current curve of the reference planar electrode device. The inset dashed squares show the definition of 100% FF and the FF of each device type at the maximum power point.

cupied by the nanoelectrodes. Despite absorbing less optical power, the NE device generates higher J_{sc} due to improved charge collection. The NE generates a resonant peak around 625 nm, which is outside the absorption range of SubPc and does not contribute to current [108]. The absorption profiles of NE and planar OPV devices are simulated using rigorous coupled-wave analysis (RCWA) [109]. The cell absorption is simulated with $10^{20} + 1$ harmonics in the x and y directions, and is found to be accurate within $\pm 0.26\%$ when integrated over the AM 1.5 spectrum. RCWA simulations are performed using the commercially available DiffractMOD simulation package from the RSoft Design Group [109]. Material optical properties are measured using ellipsometry or taken from the literature [110–113]. Film and nanostructure di-

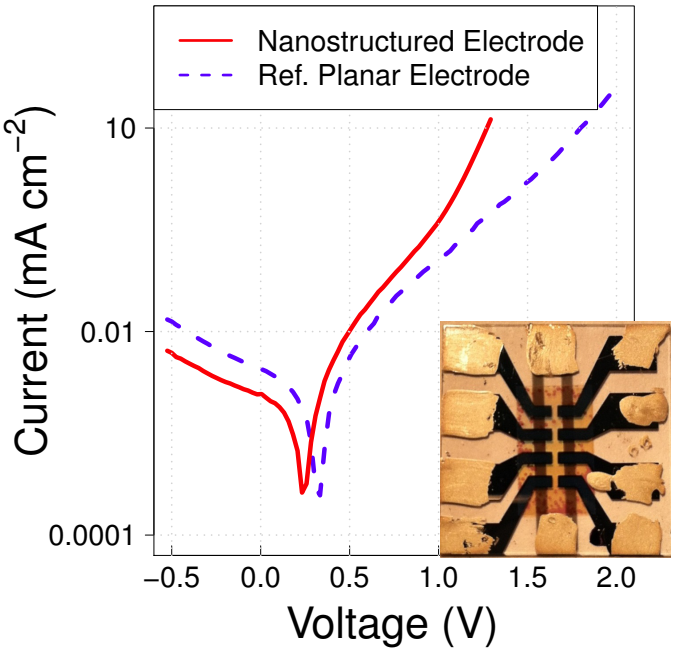

Figure 2.14: Measured dark J-V curve of nanostructured electrode and planar electrode devices. The solid red line is the dark current curve of the nanostructured electrode device. The dashed blue line is the dark current curve of the reference planar electrode device. Inset: 2 x 2 cm substrate with eight devices.

mensions are taken from cross-sectional SEM micrographs.

We confirm the absorption simulations by measuring NE and planar device absorption with focused UV-Vis, Fig. 2.17. The NE does not modify the shape of the device absorption profile. The NE device absorbs 87% of the optical power of the planar device. The focused UV-Vis light source is an Energetiq LDLS and the spectrometer is a Bruker Vertex 80 with a DTGS pyroelectric detector. Absorption is calculated from the transmission spectra by $1 - T$. Transmission is measured on NE and planar devices without Al cathodes. The active layer absorption is calculated by subtracting the absorption of the Cr/Au anode from the total device absorption, which includes the MoO_3, SubPc, C_{60} and TPBi films. Absorption profiles of three devices are measured and averaged, then normalized to 0% outside of the SubPc/C_{60}

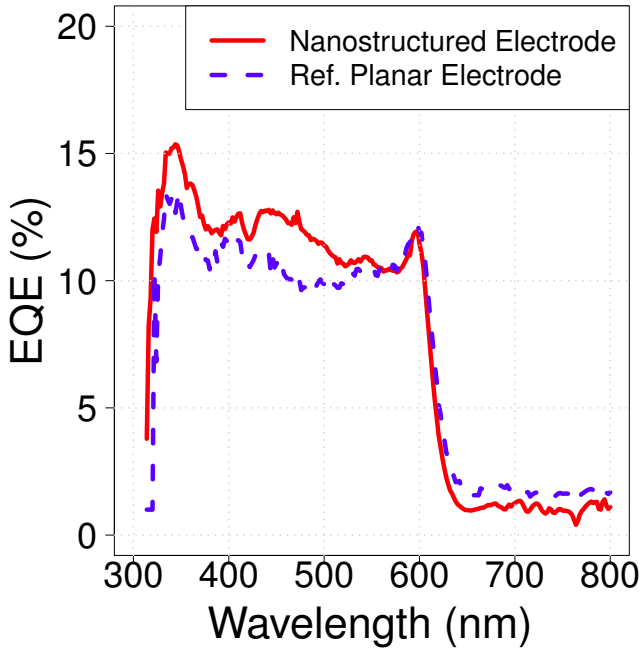

Figure 2.15: External quantum efficiency of nanostructed electrode and planar electrode devices. EQE data are averaged for two identical planar electrode devices and two NE devices.

absorption region (300-650 nm). The HeNe UV-Vis interferometer movement calibration laser at 632.8 nm is removed from the absorption profile shown in Fig. 2.17.

The UV/Vis absorption data for SubPc and C_{60} films (Fig. 2.18) are measured using a Perkins-Elmer Spectrometer with an integrating sphere; the absorption is calculated as $1-T-R$. The absorption of the fused-silica substrate has been subtracted for both films. The film thicknesses were measured using atomic force microscopy (AFM) and X-ray reflectivity. X-ray reflectometry (XRR) measures the intensity of an x-ray beam reflected at grazing angles by the sample. XRR is a useful technique for measuring single-crystalline, poly-crystalline and amorphous films between 1-1000 nm in thickness. XRR is nondestructive and has sub-nanometer accuracy. XRR works on the principle that x-rays reflect when incident upon film interfaces and the reflections form oscillations that are measured in intensity. We used XRR

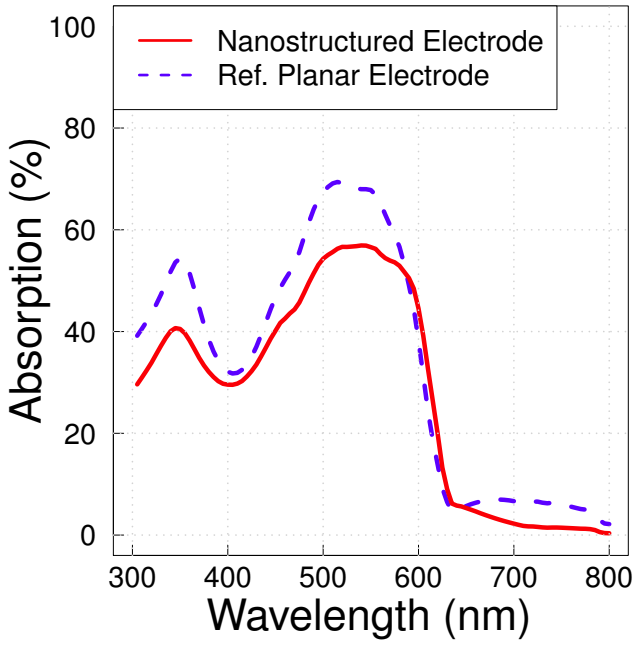

Figure 2.16: RCWA simulation of active layer absorption in NE and planar electrode OPV devices.

to confirm previous AFM and contact profilometer thickness measurements. Precise absorber thickness measurements are used to determine the optical absorption length, α, of the materials.

2.3 Conclusion

In this chapter, we show that inserted nanostructured electrodes significantly improve the fill factor of planar heterojunction OPV devices. We demonstrate improved fill factor small-molecule OPV devices by increasing charge extraction efficiency from a low-mobility film. We also show that open-circuit voltage and short-circuit current are not adversely affected by the inserted NEs. NEs increase the fill factor of an OPV device with SubPc/C_{60} from 28% to 40%. Although NEs reduce optical absorption through active volume loss, this effect is more than compensated for by improved

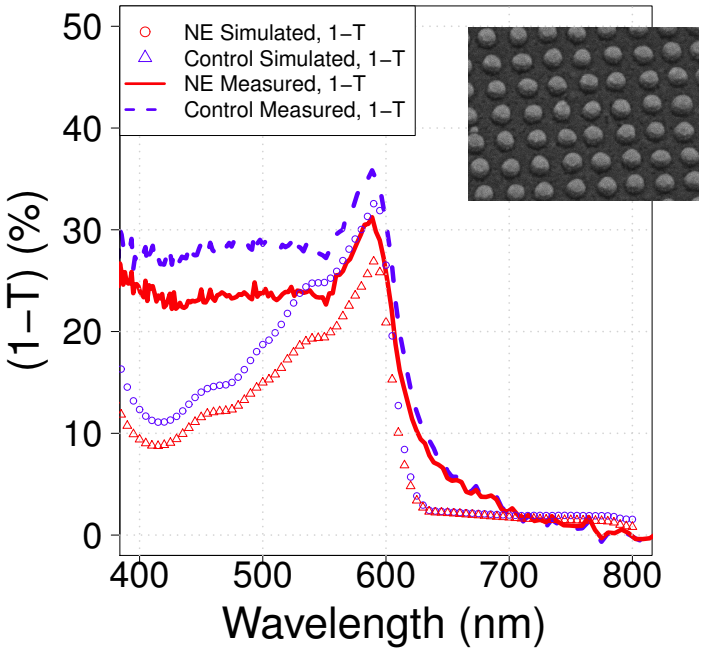

Figure 2.17: Active layer absorption measurement and RCWA simulation. Lines show the active layer UV-Vis absorption measurement with substrate and anode subtracted. Absorption data is averaged over two identical planar electrode devices and three nanostructured electrode devices. Points show RCWA active layer absorption simulation. Inset: SEM micrograph of NE array before deposition of organic material.

charge collection.

The fill factor optimization strategy can be optimized for any planar heterojunction device with low fill factor caused by poor mobility. Improved charge extraction can enable the use of thick, low-mobility films in OPV devices for more complete optical absorption.

A future improvement to the device fabrication process is the integration of NE made directly in ITO, instead of coating patterned fused-Silica glass with thin, transparent gold. An SEM micrograph of this preliminary structure is shown in Figure 2.19.

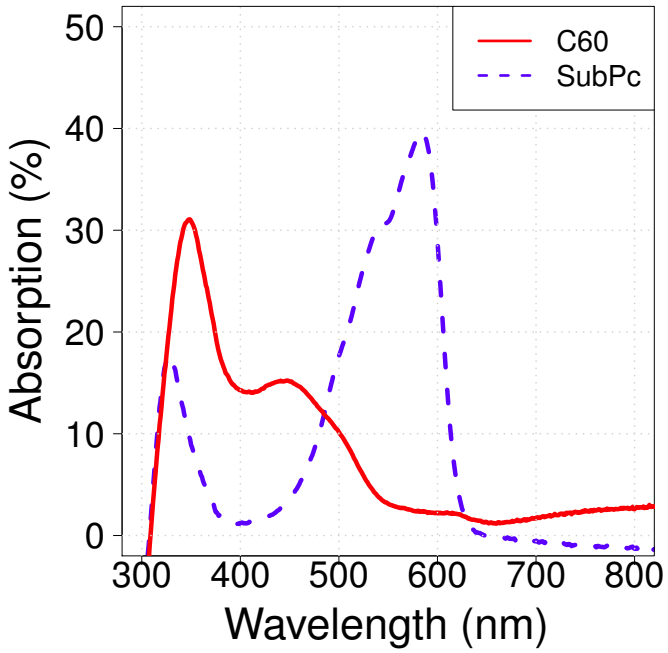

Figure 2.18: Absorption profile of neat SubPc and C_{60} films on fused-silica. The substrate absorption has been subtracted. Films are 23 nm thick as measured by AFM and X-ray reflectivity.

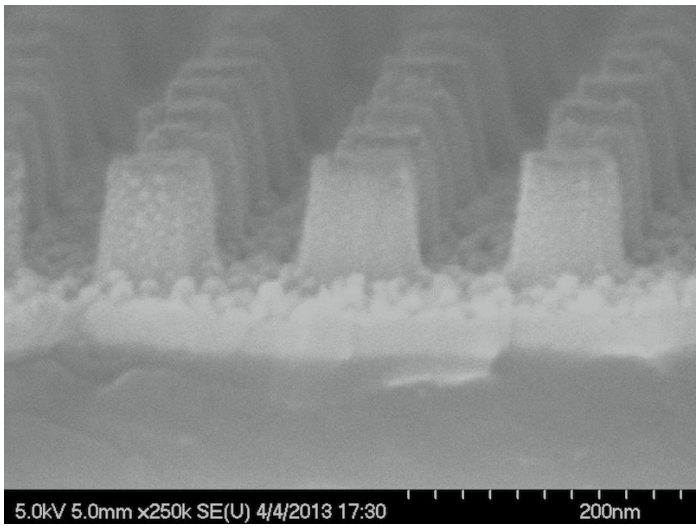

Figure 2.19: SEM micrograph of nanostructured electrodes patterned directly on ITO substrates, bypassing the need for etching of glass and coating with thin, conductive gold.

Chapter 3

Simultaneous Optimization of Absorption and Carrier Collection in OPV

3.1 Introduction

OPV efficiency is typically limited by poor carrier-collection efficiency due to the short exciton diffusion and carrier-recombination lengths in OPV active layers. There is a fundamental trade-off in designing organic photovoltaic (OPV) devices because the exciton diffusion length L_D is usually much less than the optical absorption length ($1 / \alpha$). The exciton diffusion length is commonly in the range of 5 - 20 nm. While the short exciton diffusion length restriction could be addressed by fabricating OPVs with thin active layers for efficient carrier extraction, this results in decreased optical absorption. For example, the exciton diffusion length in active layers such as boron subphthalocyanine chloride (SubPc), the dominant absorbing material considered in this study, is typically on the order of 10 nanometers [114–116], while the absorption length of SubPc is $\approx 53nm$ in the visible. The absorption and exciton diffusion challenge limits the performance of OPV devices.

In this chapter, we describe a general method for maximizing the short-circuit current in thin planar heterojunction (PHJ) OPV devices by simultaneous optimization of light absorption and carrier collection. We investigated very thin OPV devices with optical concentrators to improve absorption, which overcomes the traditional design constraint of choosing between either high exciton collection (L_D) or high optical absorption ($1 / \alpha$). We study a simple question to address this trade-off in light absorption and carrier collection: for a given absorber with experimentally obtained complex refractive indices [Figure 3.2(b)] and internal quantum efficiency η_i [Figure 3.3], how can we systematically optimize the cell performance? This framework is applicable for a wide range of OPV devices. We experimentally measured the complex refractive indices of the OPV materials and the thickness-dependence of the internal quantum efficiency of the OPV active layer. We used this data to analyze the potential benefits of light trapping strategies for maximizing the overall power conversion efficiency of the OPV device. This approach provides a general strategy for optimizing the power conversion efficiency of a wide range of OPV structures. The carrier collection efficiency and photon absorption are optimized simultaneously for different active layer thicknesses and light trapping *via* a patterned top electrode.

Our OPV design methodology simultaneously optimizes internal quantum efficiency and optical absorption. We first estimate the optimal thickness of the OPV stack electrically with the spectrally averaged internal quantum efficiency $\bar{\eta}_i$ as a function of OPV thickness. Second, we numerically optimize the patterning of an indium tin oxide (ITO) transparent top contact to maximize the photon collection within the active layer. To confirm that the optimal structure is achieved, additional optimizations of the ITO pattern are performed for slightly thinner or thicker active layers. While we focus on the SubPc/C_{60} OPV material set, the approach can be applied to any thin-film photovoltaic stack with well-characterized optical and electronic properties.

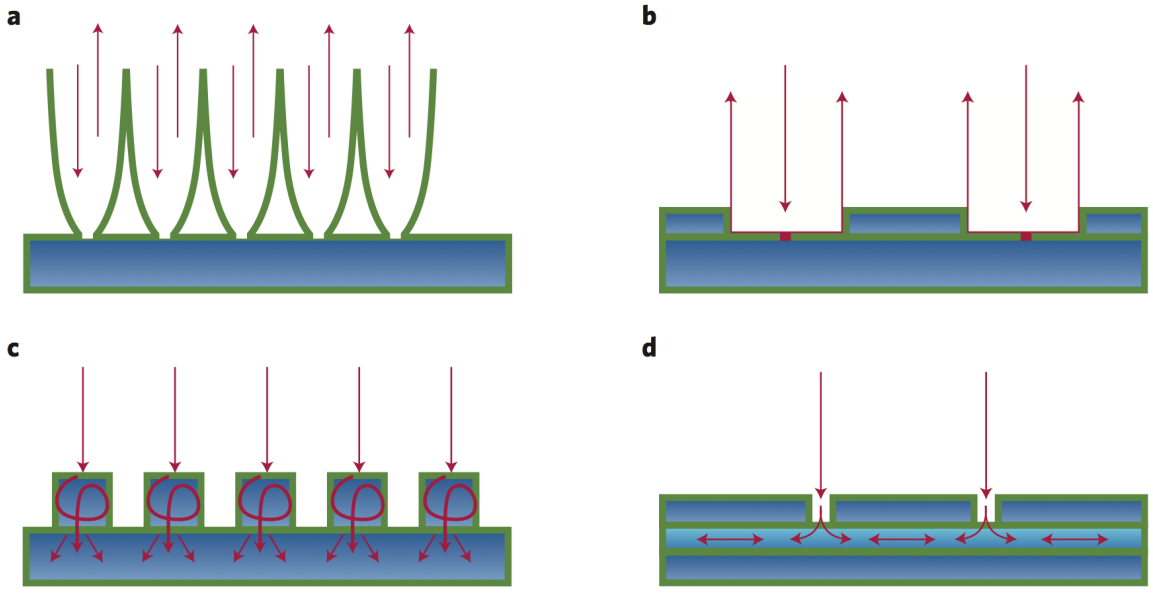

Figure 3.1: The physical structures of previous light trapping strategies applied to photovoltaic devices: a) 3D parabolic light reflectors. b) Planar antireflection nanostructures. c) Surface nanostructures to increase light trapping. d) Nanostructured slot waveguides which couple modes into the absorber. Reprinted with permission from [117]. Copyright 2012 Nature Publishing Group.

3.1.1 Improving OPV Absorption

Control of solar cell optics is vital to maximizing photovoltaic power conversion efficiency. When sunlight is incident on photovoltaic devices, the radiation will either reflect off the surface, absorb in the cell, or transmit through the cell. In order to extract the maximum power from incident radiation, the absorption should be maximized. Antireflection mechanisms, including quarter-wave coatings, texturing, and light trapping increase the absorbed radiation. In 1981, Yablonovitch investigated antireflection coatings using statistical ray optics to conclude that light-trapping schemes can increase the absorption factor by a maximum of $4n^2/sin^2\theta$, where n is the refractive index of the surface and θ is the angle of the emission cone in the medium around around the surface. [118] The ray tracing approach is applicable to

thick photovoltaic devices, which are usually much thicker than the wavelength of light they absorb. Many researchers are currently investigating whether ray optics-based enhancement factors are applicable to organic photovoltaic devices with layers much thinner than the wavelength of light. Yu et al. numerically demonstrated that the $4n^2$ Yablonovitch limit was correct only for bulk structures. By coupling multiple waveguide modes into the absorption layer, an absorption enhancement of $12 \times 4n^2$ was achieved. [119] This discovery, along with other recent photovoltaic optics research, can help create better designs for OPV antireflection coatings. Additional recent photovoltaic device light trapping strategies have included photonic crystal structures in the active material [120–123], metallic nanostructures patterned on the active layer [124–127], and dielectric gratings, which have been shown to confine light in the form of a resonance mode resulting in an enhancement of photon absorption in the underlying active layer [128–131]. An alternative approach to enhanced light trapping is building multiple junctions within one PV device.

Multijunction photovoltaics use multiple heterojunctions which absorb different fractions of the solar spectrum. The optical absorption of each sub-device depends on the band gap of the semiconductor materials. Series multijunction photovoltaics increase the voltage output at the electrodes, while maintaining the original current. When multijunction photovoltaics are in a series configuration, care must be taken to balance the current provided by each individual cell; the current output in a series configuration is limited to the output of the worst individual cell. The maximum efficiency from a multijunction photovoltaic cell with ideally designed band gaps is above 60%. [32] Fabricating and matching the current of many individual cells in one multijunction device is an engineering challenge. In practice, the best research multijunction cells have three junctions and achieved efficiencies of around 44%. The best research multijunction OPV devices have efficiencies of around 11%. [132] It is clear that multijunction photovoltaic devices offer great efficiency enhancements; however, the complex fabrication and increased cost of these devices means that

alternative methods to increase absorption are in demand.

3.1.2 OPVs with Light Trapping and High Quantum Efficiency

We modeled the optical absorption of the OPV device using rigorous coupled-wave analysis (RCWA) [109]. We find that in general for a variety of organic active media, the light trapping modes can be classified into two types: "gap" modes [135–140], as well as localized resonances in the ITO grating [128]. We find that the gap mode, which arises in an optically thin low-index material sandwiched between two high-index media, can be formed in the absorbing layers surrounded by a high-index medium such as ITO and a metal electrode. By introducing gap modes for light trapping, the enhancement increases by 20% (for 1D rectangular gratings, or 12% for triangular gratings) for TM polarized light, compared with the enhancement only

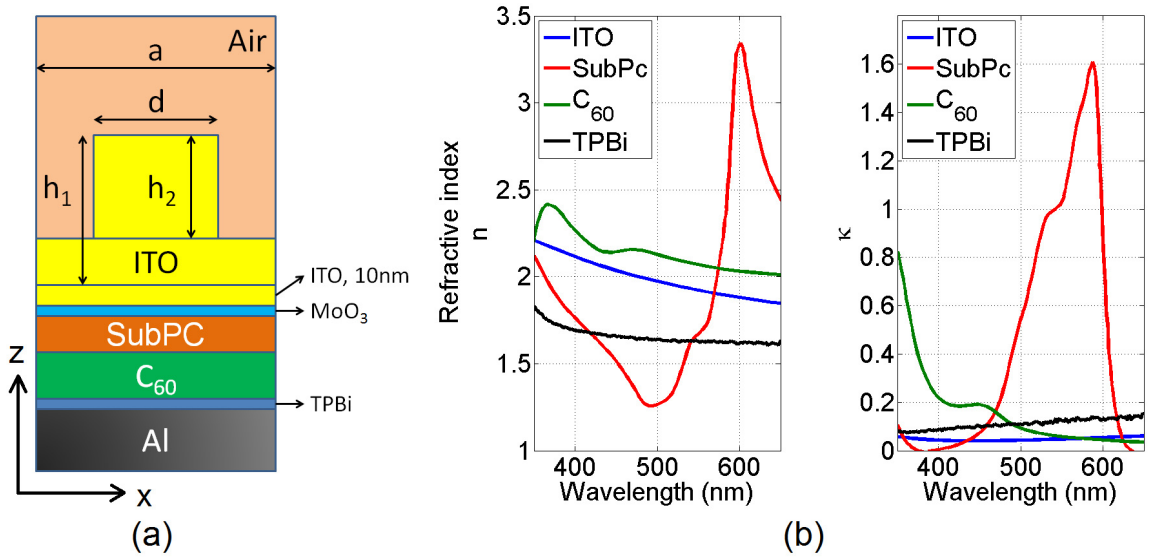

Figure 3.2: (a) Schematic showing the structure of the inverted UTOP with a patterned ITO layer on a 10/20 nm SubPc/C_{60} absorbing heterojunction layer. (b) The real part (n) and the imaginary part (κ) of the refractive index of ITO (blue) [133], C_{60} (green) [110], and SubPc (red) [134].

attributed to the dielectric resonance modes. We extend our design approach to consider two dimensional geometries, thereby eliminating the polarization dependence of the absorption enhancement. Using two-dimensional gratings comprised of ITO blocks, we find efficient mode conversion from normally-incident solar radiation into gap modes in the absorbing layers sandwiched by the bottom metallic contacts and patterned top ITO contact.

For the device with the highest η_i which occurs for a SubPc/C_{60} thickness of 30 nm, the optimal ITO grating is found to substantially enhance J_{sc} [Fig. 3.3 (inset)]. Thus, high gains are possible short circuit current for very thin structures, as was shown previously using a variety of light trapping strategies. However, if the trial material thickness is increased just slightly, this light-trapping advantage all but disappears. Specifically, for an SubPc/C_{60} layer thickness of 45 nm, we find that the ITO grating provides only a marginal J_{sc} enhancement of $\approx 5\%$ ($J_{sc} = 1.964$ mA/cm^2) over a planar cell with the identical absorbing layer and an optimized ITO layer. This result underscores the fine balance between light trapping and carrier collection: to derive the optimal cell, light trapping and carrier collection must be considered together.

3.2 UTOP Cell Efficiency

In this chapter we study the small-molecular OPV SubPc/C_{60} as a trial system. Figure 3.2(a) shows the schematic of a solar cell composed of a SubPc/C_{60} donor/accepter (D/A) planar heterojunction active layer, sandwiched by a reflecting aluminum cathode below and an ITO anode above. In the following discussion, the ratio of thicknesses of SubPc/C_{60} is set at 1 : 2, which is experimentally optimized for the cell's electrical performance. A 5 nm thick 2,2',2"-(1,3,5-benzinetriyl)-tris(1-phenyl-1-H-benzimidazole) (TPBi) layer and a 5 nm thick MoO_3 layer are inserted between the OPV layers and electrodes as exciton blocking and hole extraction layers, respectively. The OPV devices are prepared by vacuum physical vapor deposition.

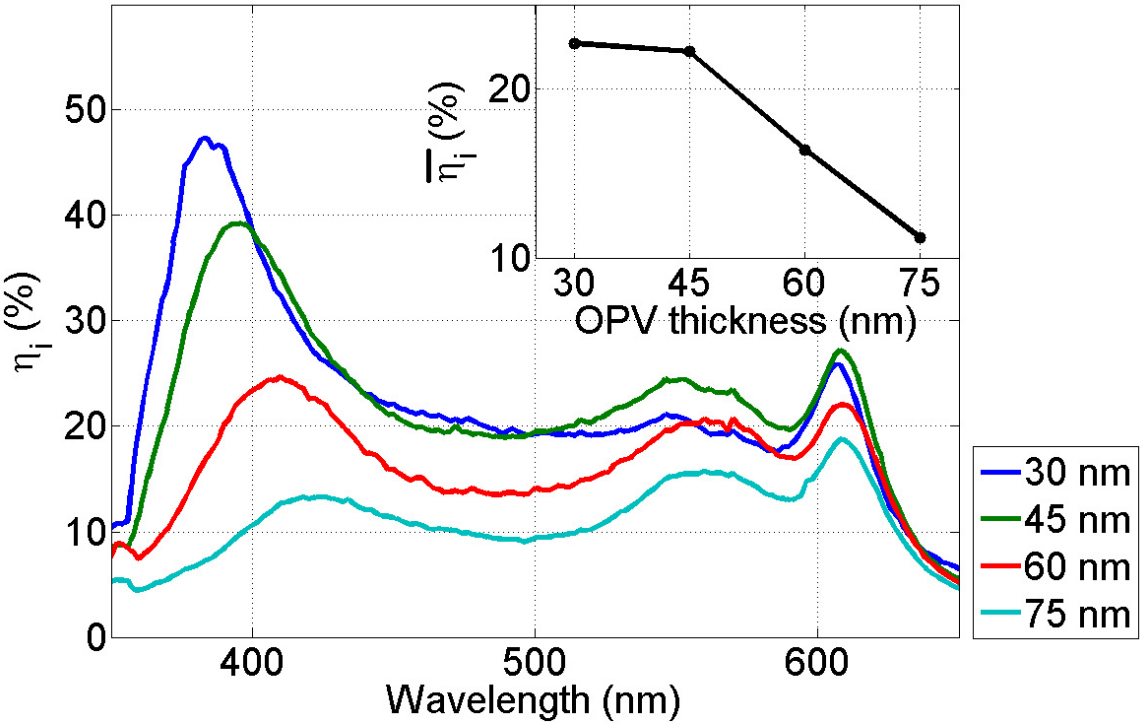

Figure 3.3: Measured η_i for the planar OPV devices with SubPc/C_{60} of different thicknesses. The ratio of the thicknesses of SubPc:C_{60} = 1 : 2. The inset shows the average quantum efficiency weighted by the solar spectrum over the relevant wavelength range.

3.2.1 Power Conversion Efficiency

We measured η_i values of the trial material's active layer stack. To measure η_i, we fabricated planar devices with active layer thicknesses from 30 nm to 75 nm in 15 nm steps. We measured $J_{sc}(\lambda)$ in response to spectrally filtered broadband illumination, using a beam chopper and lock-in amplifier to reduce background.

We measured the transmission and reflection spectra of each active layer by UV/Vis spectrometer; absorption was calculated as $A = 1 - T - R$. The absorption of each device is shown in Figure 3.5. The UV/Vis absorption data for OPV films was measured using a PerkinElmer LAMBDA 950 spectrophotometer with an integrating sphere. A diagram of sample placement for transmission and reflection

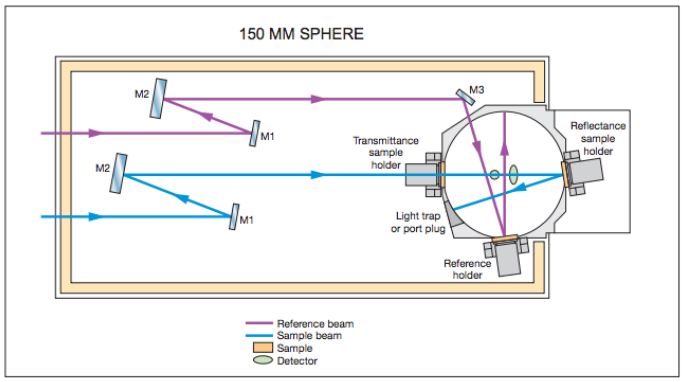

Figure 1. Optical design of 150 mm integrating sphere.

Figure 3.4: Measurement of optical absorption using an integrating sphere. Image Copyright PerkinElmer, 2004.

measurement is shown in Figure 3.4. The transmission and reflection of the actual device architecture of MoO_3 (10 nm) / SubPc (x nm) / C_{60} (2x nm) / TPBi (10 nm) on ITO glass (LumTec) were measured. In both cases the glass side of the sample faces the light source (same configuration as EQE measurements). To measure the transmission the substrate was mounted on the transmittance sample holder on the optical path prior to the integrating sphere. To measure the reflectance the substrate was mounted at the reflectance sample holder at the rear of the integrating sphere. The total device absorption is calculated as A = 1 - T - R. The absorption of the ITO glass substrate was calculated as A = 1 - T - R and subtracted from the total device absorption.

We calculated internal quantum efficiency, η_i, as the ratio of the number of extracted electrons to the number of absorbed photons. Figure 3.3 shows the measured η_i of devices composed of a planar SubPc/C_{60} layer of different thicknesses. When the active layer thickness is on the order of the exciton diffusion length, $J_{sc}(\lambda)$ depends strongly on the OPV thickness, while the open-circuit voltage (V_{oc}) and the fill factor (FF) do not vary significantly with the film thickness due to the maximal extraction of carriers before they recombine. A table showing the invariance of V_{oc} and FF is shown in Table 3.1. For very thin OPV cells with small series resistances (R_s) and

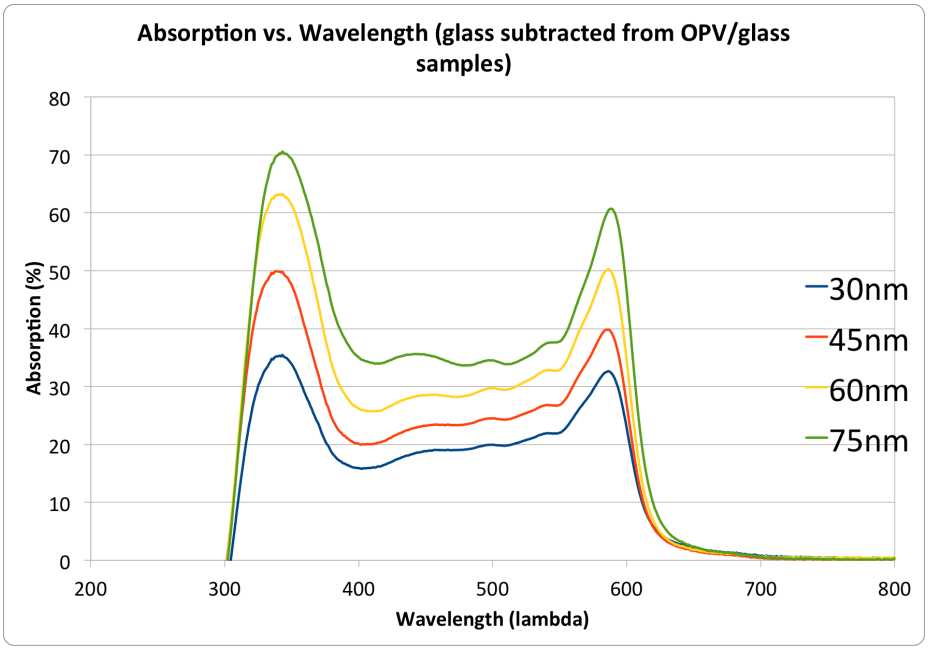

Figure 3.5: Measured absorption of SubPc/C_{60} layers with different thicknesses. The absolute absorption measurement is used to calculate internal quantum efficiency from EQE measurements.

large shunt resistances (R_{sh}), changes in R_s due to varying active layer thickness do not have a large effect on the FF or V_{oc}. [141, 142]. The short-circuit current density J_{sc} is given by

$$J_{sc} = e \int d\lambda \eta_i(\lambda) \frac{\Phi(\lambda)}{hc/\lambda} A(\lambda), \tag{3.1}$$

where $\Phi(\lambda)$ is the solar irradiance spectrum and $A(\lambda)$ is the photon collection efficiency of the cell. [143] The power-conversion efficiency of the cell, defined as $\eta_p = FF \cdot V_{oc} \cdot J_{sc}/P_{in}$, is maximized when J_{sc} is maximized. P_{in} is the incident solar power. For the remainder of this paper, we use J_{sc} as the figure of merit of our cell structures.

3.2.2 Photon Collection Efficiency

The ITO layer composed of 1D or 2D gratings acts as a resonator that causes light confinement in the gratings resulting from the destructive interference between the

Device thickness [nm]	V_{oc} [V]	FF [%]
30	1.088 ± 0.014	58.5 ± 1.7
45	1.073 ± 0.017	55.4 ± 0.8
60	1.066 ± 0.004	60.9 ± 1.3
75	1.022 ± 0	60.7 ± 0.6

Table 3.1: Performance characteristics of UTOP devices, show invariance of FF and V_{oc} with thickness. The absolute values and standard deviations are shown.

reflection at the dielectric interfaces at different heights. The gratings also provide perturbations in k-space, and induce a field component normal to the interface ($\hat{z}$) [144]. Photons are therefore coupled into surface plasmon (SP) polariton modes formed on the dielectric-metallic interface and experience stronger interaction with the active layer.

A gap-plasmon mode (gap mode) is the enhanced SP mode within a thin layer of low index dielectric material (a gap) introduced in the high-index dielectric cladding. A similar enhancement of the field confinement has been demonstrated in dielectric slot waveguides [135–137]. In this case, a dielectric slab waveguide is modified by inserting a low-index dielectric layer with the slot located in the middle of the slab; this slot supports a transverse magnetic (TM) mode. In the electrostatic limit, when the slot width is much less than the wavelength, the field intensity inside of the slot, as compared with the intensity inside the slab, can be determined by the continuity of the normal component electric displacement field $\varepsilon_w E_w = \varepsilon_s E_s$, resulting in an increase of

$$\frac{I_s}{I_w} = \frac{|E_s|^2}{|E_w|^2} = \left(\frac{\varepsilon_w}{\varepsilon_s}\right)^2 = \left(\frac{n_w}{n_s}\right)^4. \tag{3.2}$$

The subscripts w and s stand for the waveguide and the slot, respectively. This intensity increase results in an absorption increase by the same factor.

Enhanced SP modes have been observed in a system composed of a narrow low index gap layer sandwiched between a high index dielectric waveguide and a metal

surface [138–140]. In the photovoltaic device considered here, the gap mode occurs in the SubPc layer because ITO and C_{60} have higher indices. The strongly confined gap mode has a large in-plane electric-field component, which leads to increased optical absorption in the lower-index active layer.

3.3 Numerical Optimization of Top Contact Patterning

The real (n) and imaginary (κ) parts of the refractive indices of SubPc and C_{60}, (extracted from [110, 134],) are shown in the red and green lines in Figure 3.2(b), respectively. As defined in Figure 3.2(a), the transparent patterned layer has a thickness of h_1, an etch depth of h_2, a ridge width of d, and a periodicity of a. The $\tilde{n}$ of ITO is shown in the blue lines in Figure 3.2(b) [133]. The refractive index of MoO_3 is obtained from [145] and the index of TPBi is obtained by ellipsometry [black line in Figure 3.2(b)]. The software fitting step of the measurement of the refractive indices using ellipsometry is shown in Figure 3.6.

RCWA simulations are performed for the 2D grating geometry using the commercially available DiffractMOD simulation package from the RSoft Design Group [109] to investigate the dependence of the light absorption in the active layer versus all parameters h_1, h_2, a, and d. We use a gradient search algorithm to optimize all four free parameters simultaneously. For 2D simulations, 11 Fourier harmonics are used in the x-direction. For 3D simulations, 11 Fourier harmonics in both the x- and y-direction are used. For all numerical calculations, plane waves in free space are employed to model the incoming solar light, with periodic boundaries in the in-plane $(x - y)$ directions. For all optimizations, we require that the ITO has a minimum thickness of 10 nm to maintain a continuous top contact, as was done in [128]. The Air Mass 1.5 solar spectrum (global tilt, ASTM G173-03 (2008) [146]) from $\lambda = 350$ nm to 650 nm, where the SubPc/C_{60} stack possesses non-zero η_i [see Figure 3.3(b)], is

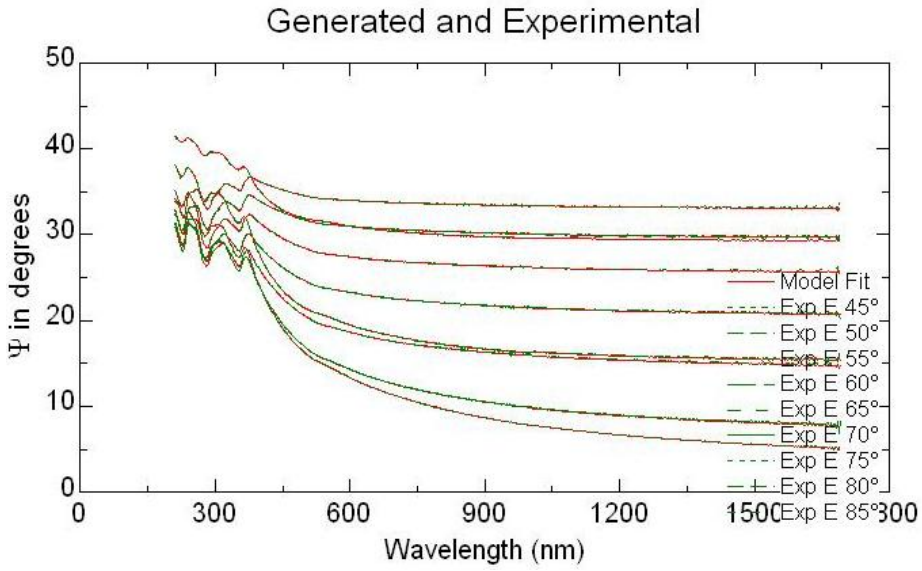

Figure 3.6: Measurement of complex refractive indices of OPV materials using a J.A. Woollam Co. spectroscopic ellipsometer, followed by curve fitting to obtain the n and k values.

used for all calculations. A plane wave source is launched at normal incidence, except for calculations where a specific angle of incidence is explicitly stated.

According to the spectrally averaged internal quantum efficiency, $\bar{\eta}_i$, in Figure 3.3, the optimal thickness of the SubPc/C_{60} layer is estimated to be 30 nm (with thicknesses of SubPc/C_{60} = 10 nm/20 nm). We start with a 30-nm thick SubPc/C_{60} stack and compare all thin-film structures with a planar reference cell with an unpatterned ITO anode with an optimized thickness of 160 nm; the reference photocurrent for this cell is J_{sc} = 1.142 mA/cm^2. Thinner ITO anodes can produce higher reference J_{sc}. We chose 160 nm thick ITO for the reference cell to because thinner ITO cause higher sheet resistance [142] (see the following section for details of the ITO anode optimization). Patterned cells also demonstrate higher J_{sc} than the improved reference J_{sc} of thin devices with $<$ 160 nm of ITO.

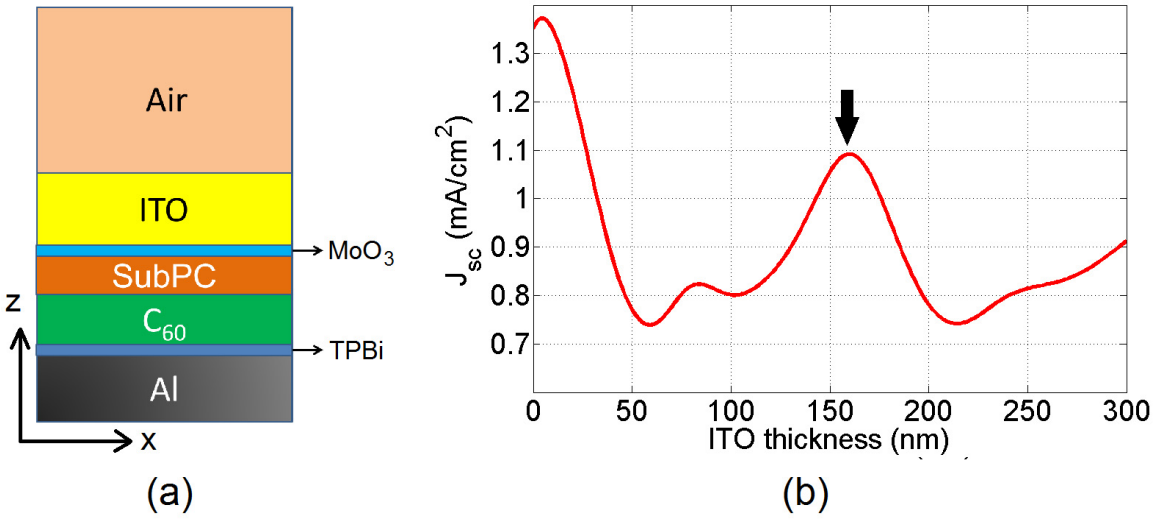

Figure 3.7: (a) Scheme of the unpatterned cell composed of a planar ITO anode. (b) J_{sc} versus the ITO thickness of the unpatterned cell.

3.4 Designing the Optimal Control OPV Device with a Planar Top Contact

In this study, the control device is an OPV cell with a planar ITO top contact. No patterning is performed on this ITO contact. The thickness of the ITO top contact will affect the optics inside the active layer of the OPV device. In this study we also qualitatively consider the ITO sheet resistance when deterring the ideal planar ITO electrode.

To calculate the photon absorbance of the solar cells enhanced by the ITO gratings, we compare the J_{sc} of all structures with that of the unpatterned structure that has the optimal thickness of the ITO anode. Figure 3.7(b) shows the photocurrent as a function of the thickness of the unpatterned ITO layer. Note that J_{sc} reaches its first local maximum of $J_{sc} = 1.372$ mA/cm^2 when the ITO is about 5 nm thick. We determine that this ITO thickness is too thin and therefore too resistive. Sputtered ITO films are also commonly crystalline and have high roughness, therefore this film may not be continuous or difficult to fabricate at this thickness. Therefore we choose

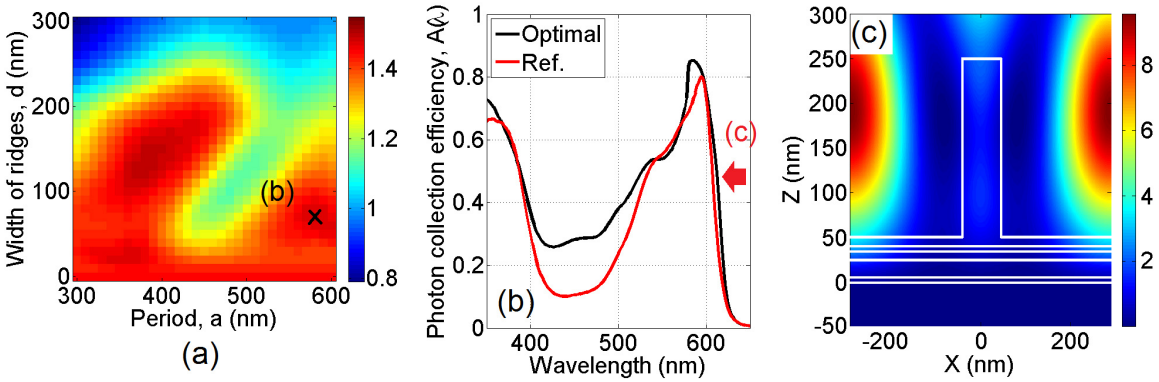

Figure 3.8: (a) Map of J_{sc} versus the period of the 1D pattern, a, and the width of the ridges, d, for TE polarized light. (b) The photon-collection efficiency spectrum of the optimal structure. (c) The intensity distribution of the electric field of the optimized case at wavelength $\lambda = 612$ nm, where the difference of photon collection efficiencies reaches the maximum.

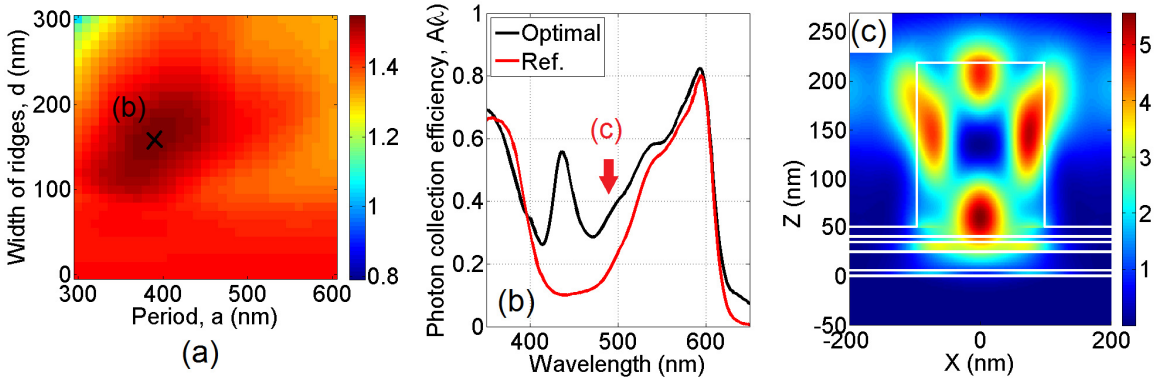

Figure 3.9: (a) Map of J_{sc} versus the period of the 1D pattern, a, and the width of the ridges, d, for TM polarized light. (b) The photon-collection efficiency spectrum of the optimal structure. (c) The intensity distribution of the electric field of the optimized case at wavelength $\lambda = 490$ nm, where the refractive index of SubPc is lowest.

the local maximum ITO thickness of 160 nm as the unpatterned reference, which is closer to the thickness of commercial ITO films on glass. At a 160 nm thickness, the J_{sc} reaches a local maximum of $J_{sc} = 1.142$ mA/cm^2.

3.4.1 1D Gratings

We first focus on the absorption in the active layer for TE polarized light (with only one $\vec{E}$ component, E_y). In this case, neither SP modes nor gap modes exist. In Figure 3.8(a), we show J_{sc} of the structure with the optimal $h_1 = 200$ nm and $h_2 = 200$ nm as determined by the numerical simulations, for different combinations of the ridge period, a, and ridge width, d. A maximum $J_{sc} = 1.498$ mA/cm^2 occurs at (a, d) =(580nm, 70nm). The optimized J_{sc} is 31% larger than that of the reference cell. The spectra of the photon collection efficiency of the optimized structure and the unpatterned reference are shown in Figure 3.8(b). Figure 3.8(c) shows the intensity distributions of the electric field along the cross-section of the optimal structure at $\lambda = 612$ nm, where the photon collection efficiency increases the most when compared with that of the planar reference cell. As expected, a resonance mode is confined in the ITO grating. This result agrees with the enhancement obtained in a previous study of enhanced light trapping in organic solar cells with dielectric photonic crystal structures as the top-surface layer [128].

With this technique, we can only induce gap modes with TM polarized light (with only one $\vec{H}$ component, H_y), because the gap mode results from the enhancement of the SP mode. For comparison, we perform a similar calculation for TM polarized light and show, in Figure 3.9(a), the impact on the J_{sc} of varying the grating period and the ridge width, using the optimized thickness of the ITO layer and etching depth (h_1, h_2)=(170 nm, 170 nm). The optimal structure has (a, d)=(400 nm, 160 nm) and the calculated $J_{sc} = 1.570$ mA/cm^2 corresponds to an increase of 38% over the unpatterned reference J_{sc}. Compared with the optimal value for TE polarized light, which does not couple to gap modes, the J_{sc} is 4.8% higher and the enhancement of J_{sc} is 20% larger, which agree with our expectation for the contribution of the gap modes. Figure 3.9(c) shows the clear presence of a gap mode enhancing the absorption in the SubPc layer at $\lambda = 490$ nm, where the light trapping in the dominant absorbing material, SubPc, is most obvious because of the lower refractive index of SubPc.

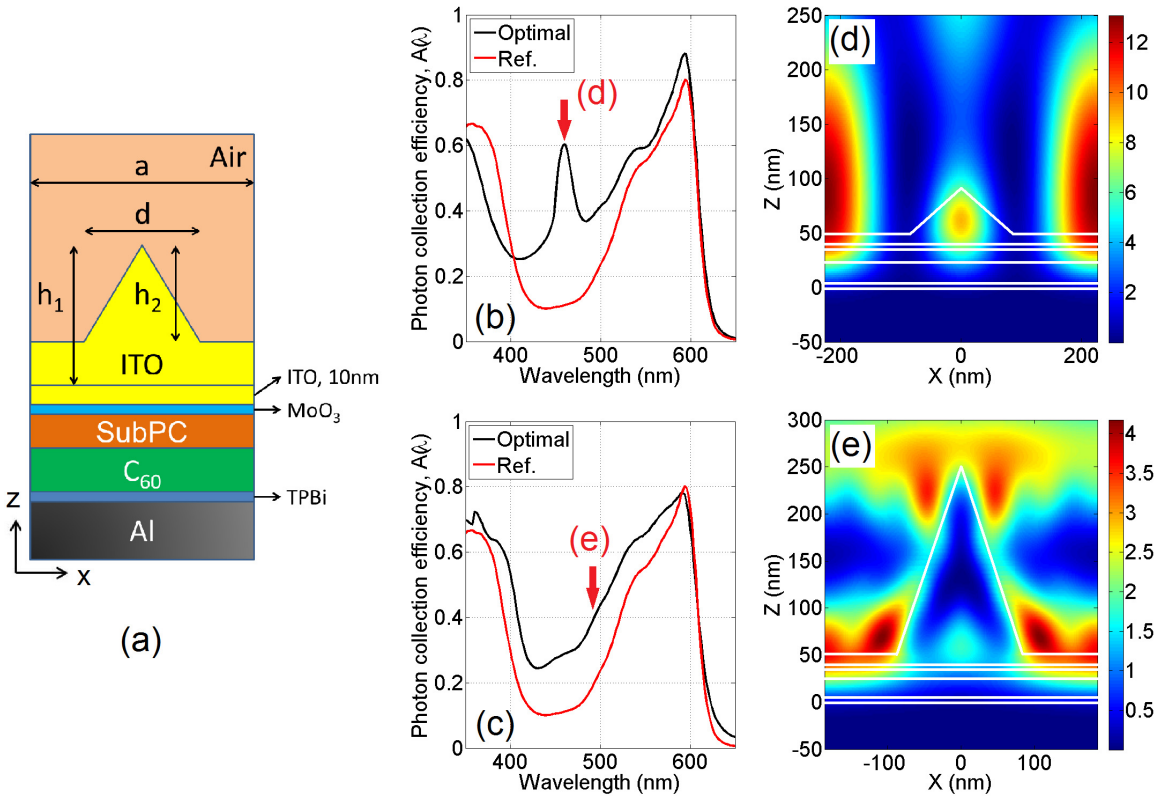

Figure 3.10: (a) Schematic of the ITO grating composed of triangular ridges. (b), (c) The spectral collection efficiencies in the active layer for TE and TM polarized light. (d) The intensities of the electric field for the optimal structure for TE polarized light at $\lambda = 458$ nm. (e) Electric field profiles for TM polarized light at $\lambda = 490$ nm.

The plasmonic and polarization dependence of the light-trapping enhancement shows the importance of the patterning geometry. Thus, the square-shaped ridges are replaced with a triangular shape to achieve better coupling between the normal-incident electric field and the SP mode. Triangular gratings cause a larger perturbation in k-space for the same volume of material as compared with square gratings, and they possess a strong second order harmonic which does not occur in the square grating due to its odd inversion symmetry. It is therefore expected that triangle gratings will provide better coupling from the incident light to a guided mode propagating along the metal back mirror [147, 148]. This triangular photovoltaic structure

is shown in Figure 3.10(a). Figures 3.10(b) and 3.10(c) plot the spectral photon collection efficiencies of the triangular structure versus that of the reference structure. The optimal structure for TE polarized light has $h_1 = h_2 = 40$ nm, $a = 400$ nm, and $d = 160$ nm, and for TM polarized light, the optimal structure has $h_1 = h_2 = 200$ nm, $a = 370$ nm, and $d = 170$ nm. The J_{sc} for TE polarized light is 1.553 mA/cm^2 and the J_{sc} for TM polarized light is 1.603 mA/cm^2. Both J_{sc} are larger than the optimized J_{sc} of the rectangular grating. The J_{sc} can be enhanced by up to 40% over that of the unpatterned reference; the enhancement resulting from both the resonance and gap mode (TM) is 12% larger than the enhancement contributed by only the resonance mode (TE).

The photon collection efficiencies of the optimal gratings for TE and TM polarized light are shown in Figures 3.10(b) and (c), respectively. Figure 3.10(d) shows well-confined resonance modes in the ITO layers at wavelength $\lambda = 458$ nm for the optimal cell for TE polarized light. Figure 3.10(e) shows the electric-field intensity at $\lambda = 490$ nm for the optimal cell for TM polarized light. Note that the index of the SubPc layer is lowest. Aside from the resonance mode, a strong gap mode is observed in the SubPc layer.

3.4.2 2D Block and Cone Arrays

To eliminate the polarization dependence of the absorption, we extend the pattern structure from one to two dimensions. As shown in Figures 3.11(a), we consider a square array of ITO rectangular blocks and cones. We calculate that the optimal block array is given by $h_1 = h_2 = 160$ nm, $a = 510$ nm, and has a side length of $d = 360$ nm to yield $J_{sc} = 1.604$ mA/cm^2. The J_{sc} is enhanced by about 41% over that of the unpatterned reference. The photon collection efficiency spectrum, $A(\lambda)$, of the optimal block arrays is shown in Figure 3.11(b). Gap modes still play an important role in the overall light confinement; for instance, Figure 3.11(d) shows strong gap modes in the intensity of the electric field at $\lambda = 490$ nm.

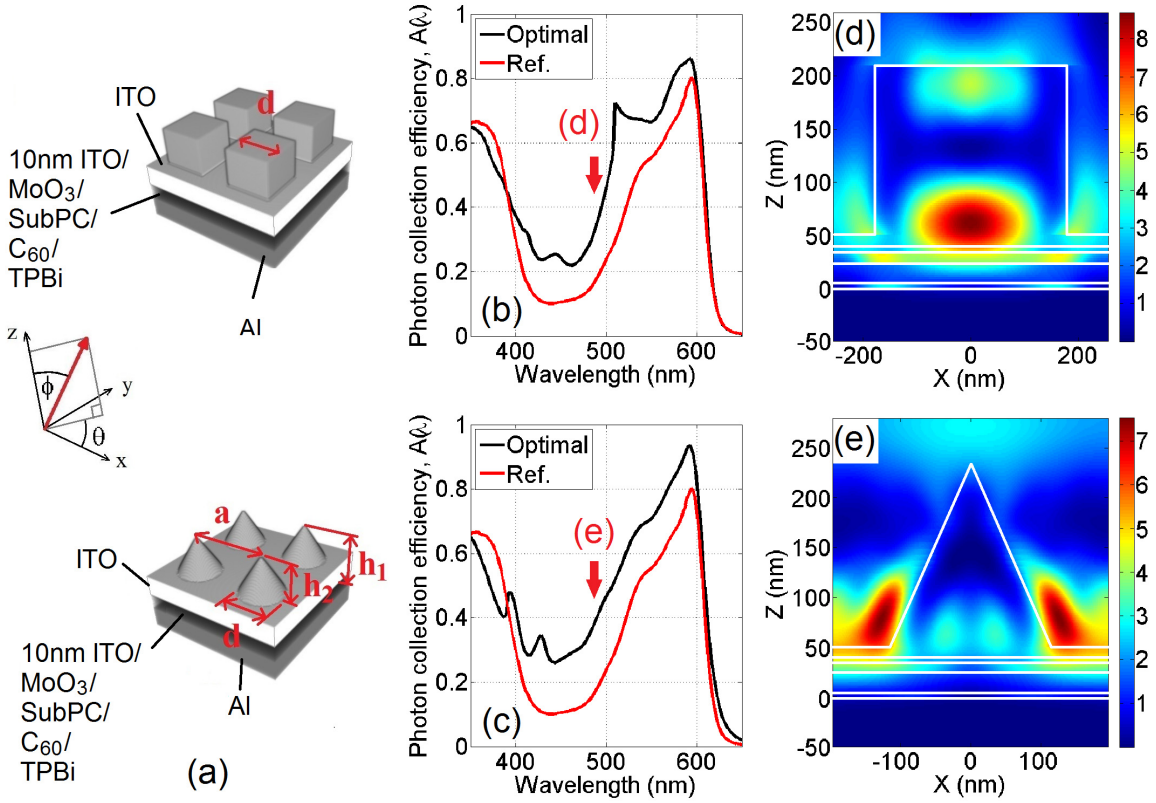

Figure 3.11: (a) Schematic of the cells composed of ITO blocks or cones in a square lattice. (b), (c) The spectral photon collection efficiency for the optimal block and cone arrays. (d), (e) The intensity distributions of the electric field of the optimized case, viewed in a cross-section which crosses the axis $y = 0$, at $\lambda = 490$ nm for the optimal block and cone arrays, respectively.

We investigated a 2D array composed of cones in a square lattice with the same motivation as for the case of 1D triangular gratings presented above. The optimal structure of the cone array has the dimensions of $h_1 = h_2 = 180$ nm, $a = 390$ nm, and $d = 240$ nm, and the optimal $J_{sc} = 1.664$ mA/cm^2. This structure has a J_{sc} that is enhanced by 46% over that of the unpatterned reference. Figure 3.11(e) shows the intensity distribution of the electric field at the estimated SP wavelength, $\lambda = 490$ nm. A strong gap mode is formed in SubPc, accompanied by a highly confined resonance mode induced closer to the active layer. The increase in J_{sc} in the cone array is 12%

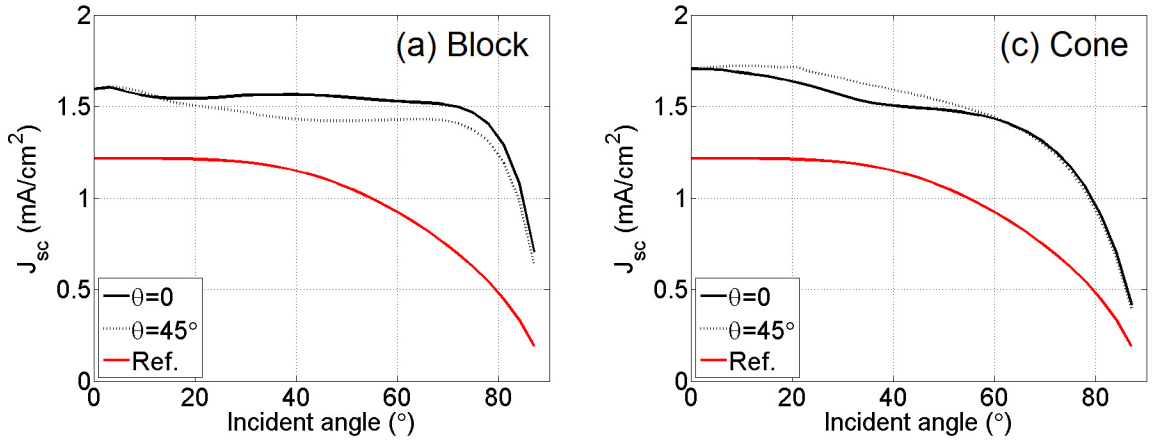

Figure 3.12: J_{sc} versus incident angle, ϕ, for the optimal block (a), and cone arrays (c). The black solid and dotted lines represent the ϕ–dependence of J_{sc} along the lattice ($\theta = 0°$) and a diagonal ($\theta = 45°$), and the red lines is for the unpatterned references.

larger in magnitude than the increase achieved by block arrays.

3.4.3 Incident-angle Dependence

One important property of photovoltaic devices is tolerance to the angle of incident light. Figure 3.12 shows the incident angle dependence of J_{sc} for the optimal block and cone arrays. For all structures, the J_{sc} of the 2D arrays is highest when light is close to normal incidence. The J_{sc} of the patterned devices remain greater than that of the unpatterned reference for all angles of incidence until $\phi > 80°$.

3.5 Discussion

The J_{sc} of our SubPc/C_{60} OPV device is maximized by optimizing the optical absorption for different active layer thicknesses and choosing the thickness that corresponds to the highest overall J_{sc}. Figure 3.13(a) shows that the J_{sc} of the cell composed of the 2D block array (solid line) reaches a maximum $J_{sc} = 1.964$ mA/cm^2 when the

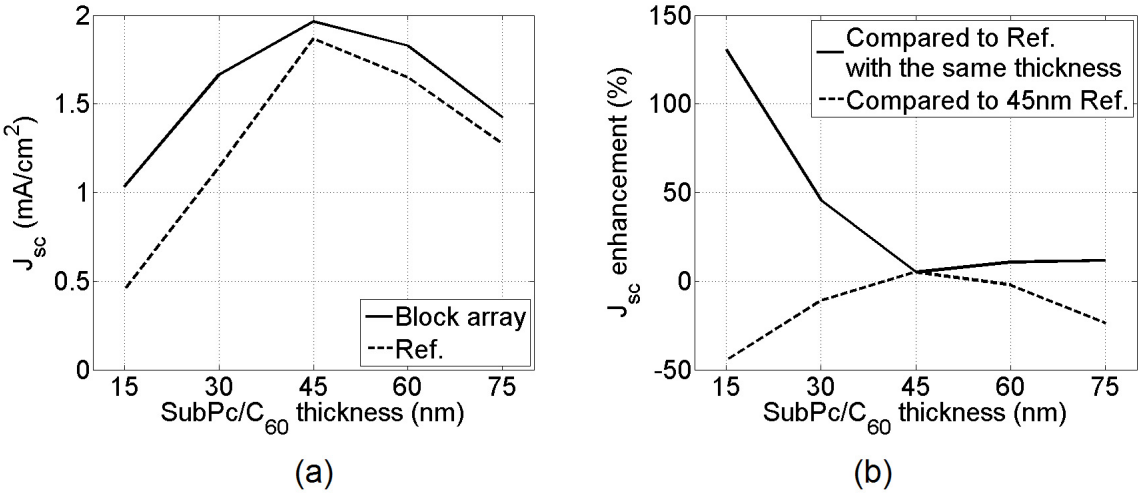

Figure 3.13: J_{sc} of 2D block arrays (solid line) and planar cells (dotted line) optimized for different UTOP thicknesses. The ratio of the thickness of SubPc:C_{60} is 1:2. (b) The enhancement of J_{sc} for block arrays compared with the optimal planar cells with corresponding SubPc/C_{60} thicknesses (solid line) and the enhancement over the planar reference having a 45 nm thick SubPc/C_{60} layer (dotted line).

thickness of SubPc/C_{60} is 45 nm (with thicknesses of SubPc/C_{60} = 15 nm/30 nm). This value corresponds to the trade-off between increasing photon absorption and decreasing η_i with increasing active layer thickness. However, for the 45 nm thick SubPc/C_{60} thin film the increase in J_{sc} is only $\approx 5\%$ [Figure 3.13(b)]. The J_{sc} enhancement shows that the enhancement in J_{sc}, compared with the optimal planar cell with corresponding active layer thickness, is much lower than in the thickest OPV devices [solid line in Figure 3.13(b)]. The dotted line in Figure 3.13(b) shows the J_{sc} enhancement compared with the optimal planar cell with a 45-nm thick active layer.

It may be possible to further increase J_{sc} over the optimal planar case by replacing top grating structures considered here with self-similar or fractal structures or other complicated pattern geometries. Fractal structures, which are inspired by nature, have been shown to provide multi-band or wide-band light trapping [149, 150] for coupling normal incident light into propagating modes in an active layer. Also, as re-

cently proposed, a quasi-periodic grating as a scattering layer on the top of the UTOP stack can provide strong and broadband light confinement in an ultra-thin active layer [151]. With these techniques, photon absorption in thin film can be enhanced beyond the limit of $4n^2/\sin^2\theta$. Though nearly 100% η_i has been reported in the previous work for thin-film organic photovoltaic cells with a 80 nm thick P3HT/PCBM blend [37], the light trapping strategies in our approach described above can still be useful to significantly enhance the cell efficiency by increasing absorption.

3.5.1 Light Trapping Polymer Nanostructures

Light trapping nanostructures can also be fabricated with a polymer grating directly on top of a thin, unpatterned planar ITO anode. For a surface polymer grating consisting of SU-8, a high-index ($n \approx 1.7$) transparent polymer material commonly used as a photoresist, we calculate an optimal 2D block array with $h_1 = h_2 = 190$ nm, $a = 580$ nm, and $d = 390$ nm for a planar ITO electrode of 10 nm on a 30-nm thick active layer. In order to compare the optical performance of a polymer grating with an ITO grating, the rest of the structure remains identical. The optimized J_{sc} for the polymer grating composed of 2D block array can achieve 1.534 mA/cm^2 and the J_{sc} enhancement is 34% over the unpatterned reference device. Although the J_{sc} increase is slightly lower than that of the cells with ITO gratings, the polymer gratings can be an effective alternative because of the substantial decrease in fabrication cost. Note that the ITO electrode should be thick enough to suppress the series resistance of the device. Based on previous studies, the sheet resistance of a 10-nm thick ITO electrode is much larger than metal thin films of the same thickness [152]. ITO remains competitive with new alternatives for transparent electrodes such as graphene and carbon nanotubes [153–155].

3.6 Conclusions

We describe a general method for optimizing the power conversion efficiency in thin planar heterojunction OPV cells by simultaneous optimization of carrier collection and light trapping. When applied to the trial OPV device with SubPc/C_{60}, we find that for a thin 30 nm active layer, we can achieve a 46% improvement in J_{sc}, as compared with an optimized planar OPV device. Moreover, the optimized patterning geometry also improves the angle-of-incident tolerance, yielding nearly constant short-circuit current up to an angle of incidence of about 80° from the vertical.

When we optimize the short-circuit current simultaneously for carrier collection and light trapping, the best cell is not the thinnest cell, or the cell with the highest IQE. Moreover, the eventual optimal cell, with a 45 nm thick SubPc/C_{60} layer, derives only a small 5% enhancement in photocurrent to $J_{sc} = 1.964$ mA/cm^2 compared to the optimized unpatterned reference cell. For other materials, the balance between light trapping and carrier collection will point to a different optimal cell geometry. This geometry might strongly favor light trapping in materials with a lower diffusion length than the trial material considered here. An alternate structure, which replaces the ITO top structure with a stampable polymer grating, yields a 34% enhancement in J_{sc} for the 30 nm thick device and would simplify fabrication.

Our results show that the simultaneous optimization of light trapping and carrier collection in a planar heterojunction OPV cell can generally improve the overall device performance, but the increase in light trapping only marginally improves some OPV devices. If the extra cost of fabrication is taken into account, complex OPV light trapping strategies may not be appropriate. On the other hand, we note that light trapping techniques can greatly improve 'bad' OPV materials with low absorption or short exciton diffusion and carrier-recombination lengths, opening up the design space for OPV cells. Light trapping may also be more beneficial for multijunction cells, which constrain the choice of OPV materials to systems that are less optimal for a given wavelength range than what is possible in single-junction cells.

Chapter 4

Graphene Electrodes on Organic Thin-Film Devices via Orthogonal Chemistry

4.1 Introduction

Integration of graphene electrodes with organic semiconductor devices has been widely investigated due to graphene's promising conductivity, flexibility, and transparency. Cox et al. previously explored the integration of single-layer graphene cathodes for organic photovoltaics. [156] In this study, a single graphene layer was transferred to a polydimethylsiloxane (PDMS) stamp and physically laminated on top of an OPV device stack. The graphene is strongly adhered to the PDMS stamp, and not to the organic thin-films; therefore, the stamp is left in contact with the device during characterization, shown in Figure 4.1. This previous study demonstrated that OPV devices with highly transparent cathodes and anodes can be highly transparent. A commercial OPV application enabled by highly transparent devices with electrodes like graphene is architectural or window-based PV. Another recent investigation also demonstrated the utility of inverted OPV devices with graphene cathodes [74], though

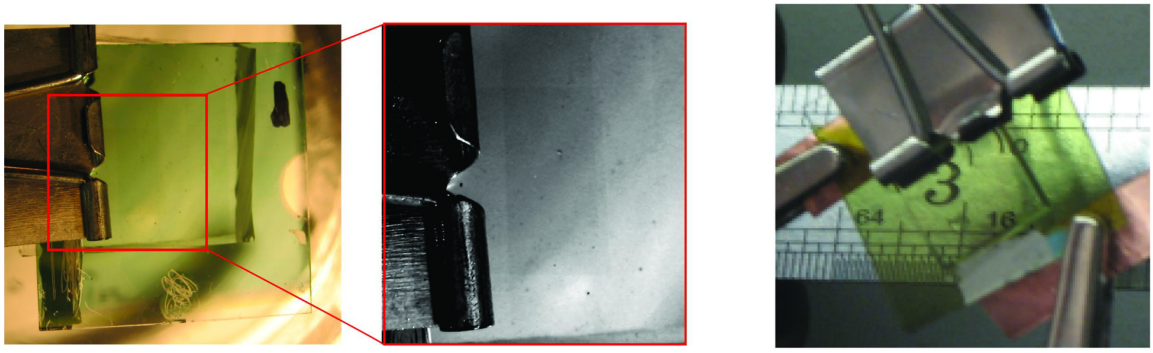

Figure 4.1: Image of a graphene device which shows the vertical ITO anode and the completed device. The OPV device is highly transparent. Adapted from 4.1. Copyright Applied Physics Letters, 2011.

not with a laminated top electrode. We targeted three improvements to these initial graphene cathode lamination studies. First, we will increase the low fill factor by decreasing the series resistance of graphene anodes. Second, we will remove the PDMS stamp after graphene transfer. Third, we will demonstrate this transfer technique on other organic electronic devices, such as OLEDs and FETs. Our graphene transfer method is more robust and has wider applicability with organic optoelectronic devices than previous transfer methods.

Typical methods to transfer large-area films of graphene synthesized by chemical vapor deposition on metal catalysts are not suitable for organic thin-films, limiting possible architectures which integrate graphene into organic optoelectronic devices. This chapter explores a process for high-quality graphene transfer onto chemically sensitive, weakly interacting organic semiconductor thin-films. To demonstrate our transfer method's compatibility with organic semiconductors, we fabricate three classes of organic electronic devices: field effect transistors without high temperature annealing, transparent organic light-emitting diodes, and transparent small-molecule organic photovoltaic devices.

A widely studied graphene transfer method is a polymer transfer method, in which graphene is coated in an intermediate polymer (like poly-methylmethacrylate

(PMMA)) to provide mechanical support. [157–160] Polymer transfer methods include a combination of solvent, water, etching and annealing steps during processing and post-processing that are incompatible with organic semiconductors.

Another graphene transfer method attaches graphene to a semi-rigid elastomeric PDMS stamp which provides mechanical support and improved pick-and-place control when stamping onto the destination substrate. [58] The PDMS stamp transfer method fails on organic thin-films because graphene tends to adhere to the stamp rather than the low surface energy organic films when the stamp is pulled away. [161] Recent investigations added functional interlayers such as graphene oxide and PEDOT:PSS to increase the surface energy of organic thin-films, which improves graphene adhesion. [162, 163]

Both polymer support and PDMS transfer methods can leave resist or uncured siloxane residue on the transferred graphene. Transfer residue can negatively affect device performance, increase the graphene contact resistance [164], and decrease flexibility of graphene films. Song et al. introduced a solution to the adhesion and cleanliness problem by coating PDMS with a set of novel polymer release layers [165]. Song used this transfer method to transfer graphene onto insulating organic materials for gated FETs and capacitors. However, no study has yet demonstrated transfer of graphene onto active organic semiconductors, as is necessary for OLED and OPV devices.

In this chapter, we describe a process for transfer of single-layer, CVD-grown, graphene onto organic semiconductor thin-film devices, enabling the use of graphene as a transparent top electrode for all organic optoelectronic devices. The transfer process incorporates an elastomeric stamp with a heavily fluorinated orthogonal photoresist release layer. The orthogonal photoresist release layer and residue are subsequently removed post-transfer with orthogonal solvents. The transferred graphene film may be stacked to improve electrode conductivity, and is clean enough to be directly contacted as an electrode or inserted as a recombination layer for multijunc-

tion organic devices. [166] These experiments demonstrate the potential of hybrid graphene/organic devices in which graphene is transferred directly onto underlying organic structures.

4.1.1 Orthogonal Processing of Organic Semiconductors

One major advantage of organic electronics fabrication is the potential for high-volume, low-temperature solution processing. In this strategy, the organic material is delivered in a solvent. The advantage to this approach can also be a disadvantage because many of the solvents commonly used in cleaning and photolithography can adversely affect organic materials. In this section we very briefly review solvent chemistry and discuss a selection of investigations on solvent compatibility with organic materials.

The two extremes of solubility are miscibility and orthogonality. A common chemistry rule is that "like [materials] dissolves like [materials]". For example, polar solvents are often good solvents for polar molecules. There are three types of solvents: oxygenated solvents, hydrocarbon solvents, and halogenated solvents. Oxygenated solvents are ketones, glycol ethers and alcohols. Examples of oxygenated solvents are acetone, isopropyl alcohol, and methanol. Hydrocarbon solvents include aromatic and aliphatic hydrocarbons. Examples of hydrocarbon solvents are decane, toluene, and xylene. Halogenated solvents have halogens (e.g. chlorobenzene). Polar solvents contain polar molecules which have a mostly positive charge on one side and a mostly negative charge on the other side. The positive end can attract the negative end of another molecule. Water is polar because the oxygen side is negative while hydrogen is positive. In non-polar bonding the molecules share electrons. Many solvents, including common oxygenated solvents used during fabrication, can degrade organic materials.

A major challenge in organic electronic fabrication is the ability to perform chemical processing on organic materials. Examples of processes complicated by solvent

incompatibility are cleaning, additional film deposition by spin casting, and patterning by lithography. To adapt these processes, we need orthogonal solvents that do not affect common organic materials. By using solvents of the opposite polarity of underlying films, multiple solution-processed organic layers can be deposited. In a study by Zakhidov et al., fluorinated solvents were used that only solubilize fluorinated organics. [167] In [168], the authors used fluorinated solvents with a highly fluorinated photoresist to perform UV and electron beam lithography at sub-micron resolutions. In this study, PEDOT:PSS contacts were patterned for a bottom-contact OFET, which is normally difficult to achieve as PEDOT:PSS is hydrophilic and incompatible with lithography processing chemicals. Lee et al. synthesized heavily fluorinated electroluminescent organic films that are patterned with traditional photoresists. [169] Traditional photoresists are orthogonal to the highly fluorinated organic molecules. The difficulty discussed in this study is synthesizing a heavily fluorinated polymer which is also an efficient light emitter. The same group later demonstrated a full set of RGB emitters that are highly fluorinated so can be patterned using traditional lithography materials. [170]

Machui et al. reported on the solvent compatibility of the widely-used OPV organic semiconductors P3HT and PCBM. [171] In a study of solution processed OPV devices, Ayzner et al. found that dichlorobenzene and dichloromethane were sufficiently orthogonal to spin bilayer P3HT and PCBM films on top of each other without affecting the underlying films. [172] By engineering the orthogonality of organic materials and solvents, we enable the use of fluorinated resists as polymer release layers during graphene transfer.

4.1.2 Transfer Process

We transfer graphene via an elastomeric polydimethylsiloxane (PDMS) stamp treated with OSCoR fluorinated photoresist manufactured by Orthogonal, Inc. A schematic of this process is depicted in Figure 4.2a. We manage the material compatibility and

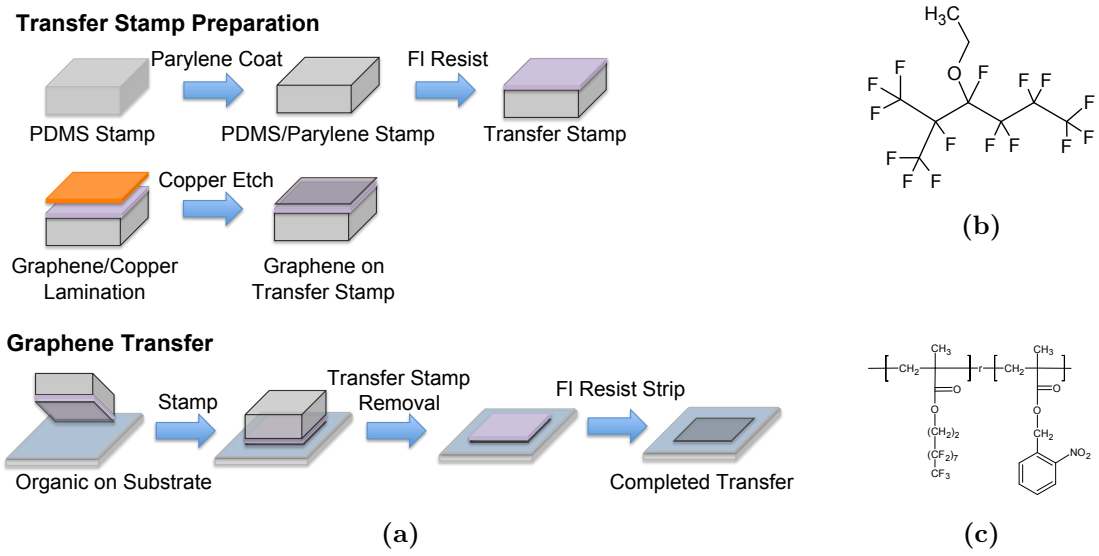

Figure 4.2: (a) Schematic of the fabrication of a transfer stamp, above, and graphene transfer onto a substrate, below. (b) Sample molecular structure for a hydrofluoroether solvent (Novec™ Engineered Fluid 7500 shown). [167] (c) Molecular structure of a fluorinated copolymer photoresist consisting of 1H,1H,2H,2H-perfluorodecyl methacrylate (FDMA) and tert-butyl methacrylate (TBMA)). [173]

surface energy problem by using fl-resist orthogonal chemistry. Orthogonal chemistry allows us to control the miscibility of organics in solvents; miscible materials mix homogenously while orthogonal materials remain heterogenous when mixed. Most oleophilic and hydrophilic organic materials are miscible or will degrade in the presence of aromatic and halogenated solvents. [174,175] The heavily fluorinated photoresist release layer and solvents do not dissolve or infiltrate the structures of organic semiconductors because they are orthogonal.

Preparation of Chemical Vapor Deposition Graphene films: Large-area films of graphene were grown using chemical vapor deposition (CVD) processes on copper foil. The complete synthesis is reported in the supporting information of a previous study. [69] We will briefly summarize the synthesis process here: Large-grain graphene was grown by low-pressure CVD using methane as a carbon feedstock. The graphene

was grown on the surface of 25 μm copper foil. The copper was annealed at 1 mTorr at 1030°C under a hydrogen background for 15 minutes. Graphene was grown at 10 mTorr and 1000°C by flowing methane and hydrogen over the foil. Following growth, the sample was cooled under a flow of methane and hydrogen.

The parylene-c is a conformal CVD process which passivates the PDMS surface and prevents silicone contamination transfer to the graphene. [176] We prepare PDMS stamps by mixing Sylgard 184 PDMS (Dow Corning) as instructed, vacuum degassing the mixture, and curing in a 80°C oven for 1 hour. Afterwards, we coat the stamps with approximately 450 nm of parylene-c. Parylene-c was deposited in a Specialty Coating Systems Labcoter. PDMS/parylene-c stamps were then spin-coated with Orthogonal fl-resist to a thickness of 450 nm. Orthogonal fl-resist contains a fluorinated copolymer based on 1H,1H,2H,2H-perfluorodecyl methacrylate (FDMA) and tert-butyl methacrylate (TBMA)), shown in Figure 4.2c, which has previously demonstrated compatibility with organic semiconductors. [167, 173, 177, 178] CVD graphene films on copper foil were cut with scissors and placed graphene-side down on the PDMS/parylene-c/fl-resist stamp. To adhere the graphene/copper foil to the stamps without mechanical damage, we placed the graphene/copper foil onto the transfer stamp while uniform downward pressure was applied by a glass-backed PDMS stamp covered with the non-adhesive side of Scotch® Magic™ Tape (3M). The non-adhesive side of scotch tape does not adhere to the graphene/copper foil or the PDMS/parylene-c/fl-resist stamp. Stamps with graphene/copper foil attached are shown in Figure 4.3. The PDMS/parylene-c/fl-resist/graphene stamp is floated in ferric chloride for approximetally 20 minutes to etch away the copper foil. After copper etching the stamp is rinsed in DI water, blown dry with N_2, and left overnight to dry.

It was previously difficult to transfer graphene from stamps onto organic materials because organic thin-films have low surface energies due to van der Waals bonding. [165] We found that thermal release tape [162] did not create a sufficient

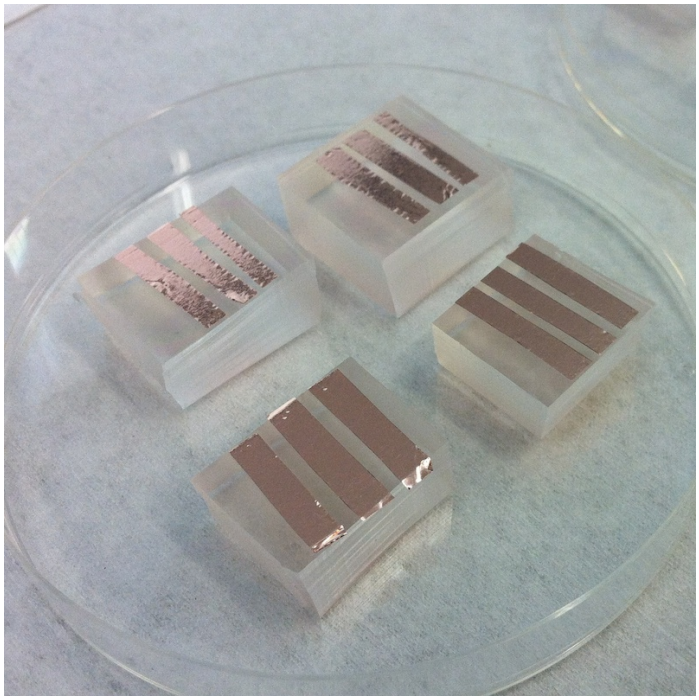

Figure 4.3: Photograph of CVD graphene on copper foils adhered to the top of PDMS/parylene-c/fl-resist stamps, before the copper foil is etched in ferric chloride. Each stamp has three graphene strips that are approximately 2 by 15 mm.

difference in surface energy to adhere graphene directly to low energy organic thin-films. The fl-resist modifies the surface adhesion of the PDMS stamp so graphene preferentially adheres to the destination substrate (an organic thin-film). We place the transfer stamp onto the organic thin films previously deposited onto a substrate (Figure 4.2a) and apply light pressure while heating the substrate to 50°C to promote adhesion between the graphene stamp and the substrate. After 30 seconds the stamp is lifted away from the surface, which leaves a single layer of graphene. Residual fl-resist is removed by three subsequent spray/puddle spin cleans using the Orthogonal photoresist stripper. The photoresist stripper contains an orthogonal solvent from the 3M Novec family of hydrofluoroethers (example shown in Figure 4.2b). We complete the fl-resist-transfer process by spinning the substrate to remove any residual stripper. The transfer process may be repeated to transfer additional graphene films.

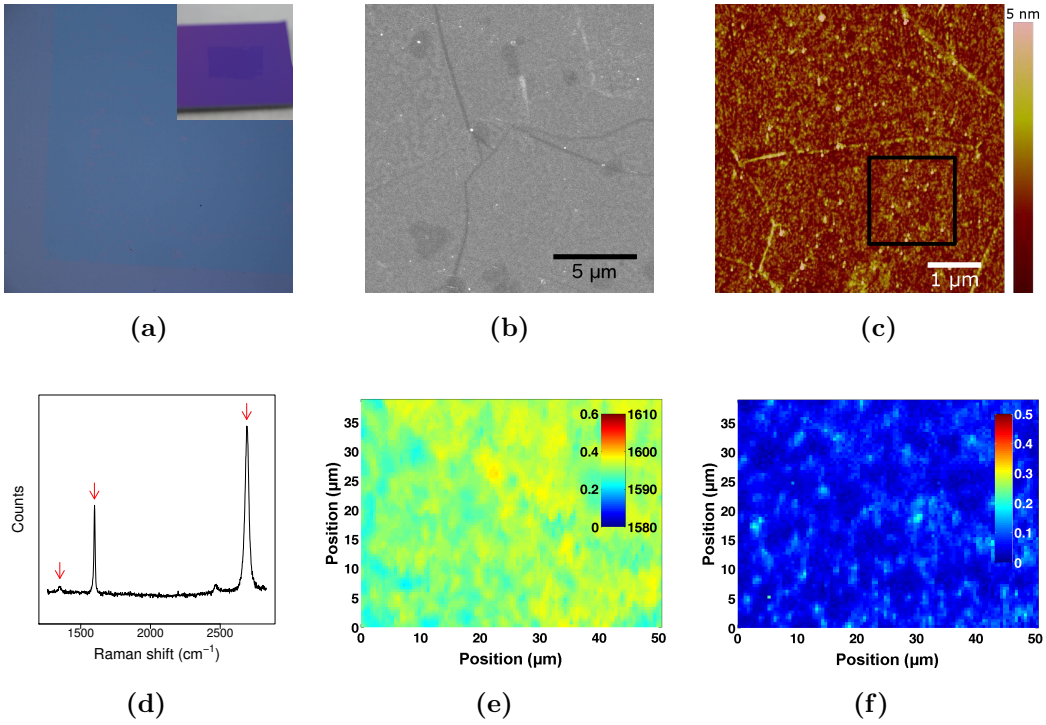

Figure 4.4: (a) Optical microscope image of fl-resist-transferred graphene on SiO_2. Inset photograph of graphene transferred to a SiO_2 chip. (b) SEM micrograph of fl-resist-transferred graphene on SiO_2. (c) 5 by 5 μm AFM scan of fl-resist-transferred graphene on SiO_2. The height scale is 5 nm. The RMS roughness is 0.526 nm within the 1.5 by 1.5 μm inset box. (d) Raman shift of fl-resist-transferred graphene on SiO_2. (e) Spatially resolved scan of G-Peak position of fl-resist-transferred graphene on SiO_2, 50 by 40 μm. The color scale bar shows the estimated doping in eV and the G-Peak position shift. (f) Spatially resolved scan of the ratio of D-band (1350 cm^{-1}) to G-band intensity of fl-resist-transferred graphene on SiO_2. The color scale bar shows the magnitude of the intensity ratio, from 0 to 0.5.

4.1.3 Graphene Characterization

Measurement and Characterization: We recorded SEM images in a Hitachi S-4700 field emission scanning electron microscope operated at 2 kV. We obtained AFM

images in a Dimension Icon which was operated in tapping mode. We performed Raman spectroscopy with a Renishaw inVia Raman Microscope using a 532 nm laser. The resolution of spatial Raman images is 500 nm.

We transferred graphene films up to 1 cm^2 in area onto 300 nm SiO_2/Si substrates, as shown in Figure 4.4a. We inspected these films using scanning electron microscopy (SEM) and atomic force microscopy (AFM). Figure 4.4b shows an SEM micrograph of fl-resist-transferred graphene on silicon. The graphene film has no rips or tears and minimal wrinkles and particulate residue. The AFM scan in Figure 4.4c shows few wrinkles, rips and tears with no cracks particulate residue. The graphene RMS roughness is 0.526 nm over the 1.5 by 1.5 μm inset area. The thin, uniform layer of resist residue is comparable to the residue left on graphene transferred with PMMA mechanical support after high-temperature vacuum annealing. [179]

We inspected the fl-resist-transferred graphene films using Raman spectroscopy and confirmed that the graphene is continuous with a low defect density. We transferred graphene onto SiO_2/Si substrates and measured the Raman shift, shown in Figure 4.4d. The small D-peak of transferred graphene at 1352.5 cm^{-2} demonstrates that the transfer process does not induce significant defects. Figure 4.4e shows the spatially resolved G-Peak position over a 50 by 40 μm area. The G-Peak consistency shows that the graphene film is continuous. The residual fl-resist causes 0.2-0.3 eV of doping, as extracted from the G-Peak shift. [180] Figure 4.4f shows the spatially resolved ratio of D-band to G-band intensity. The D-band to G-band ratio is less than 0.1 across the entire scanned area, which indicates that the defect density is low.

4.1.4 SEM and Raman of Fl-transferred Graphene

We evaluated graphene transferred onto organic thin films with Raman spectroscopy and Scanning Electron Microscopy (SEM). We first deposited the small-molecule organic, 2,2',2"-(1,3,5-benzinetriyl)-tris(1-phenyl-1-H-benzimidazole (TPBi) on ITO-

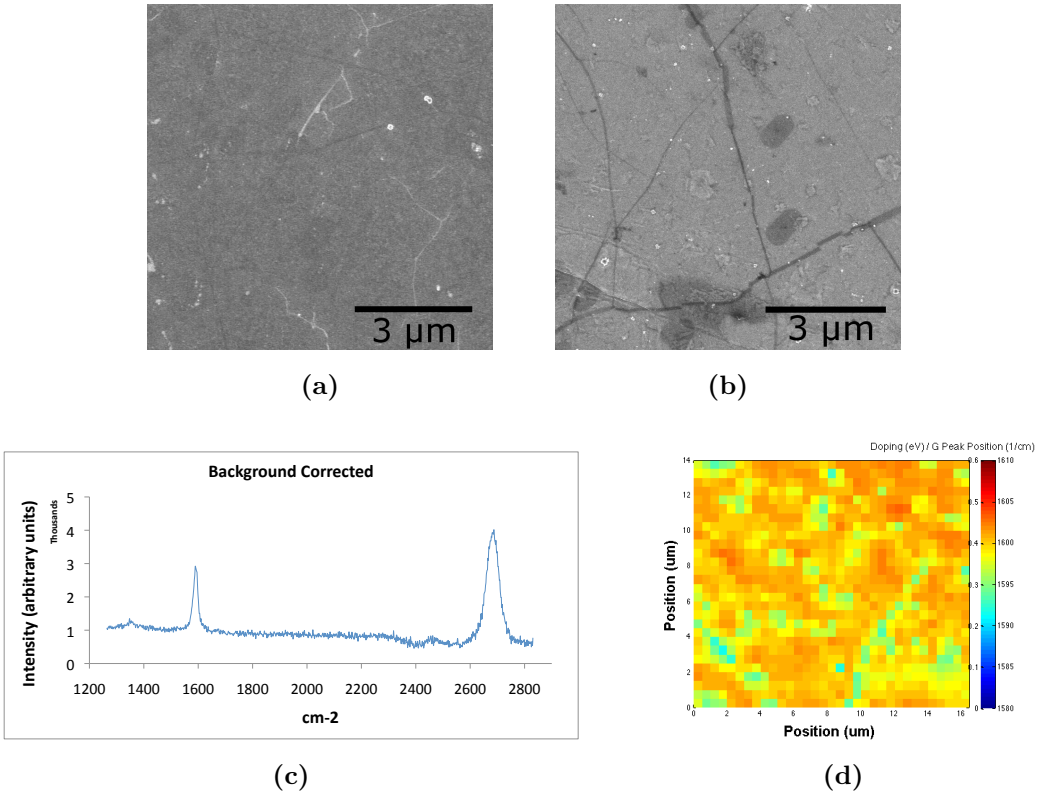

Figure 4.5: (a) SEM micrograph of fl-transferred graphene on TPBi, an organic semiconductor film. (b) SEM micrograph of PMMA-transferred graphene on SiO_2. (c) Background corrected Raman spectrum of fl-transferred graphene on TPBi (d) Spatially resolved scan of G-Peak position of PMMA-transferred graphene on SiO_2. The color scale bar shows doping estimate in eV and peak position shift.

coated glass at 1.0 Å sec^{-1} to a thickness of 40 nm. TPBi is a common hole blocking material in OPVs and electron transport material in OLEDs. Figure 4.5a shows an SEM micrograph of graphene transferred onto an organic thin-film of TPBi. The film of graphene transferred via fl-resist is similar to traditional PMMA-transferred graphene which is shown in Figure 4.5b. The fl-transfer method leaves less residue and particulate on the surface than PMMA transfer.

Graphene transferred onto Si using traditionally PMMA methods was analyzed with Raman spectroscopy. Figure 4.5d shows the spatially resolved G-Peak scan of

PMMA-transferred graphene over a 16 by 14 μm area. The residual PMMA resist causes 0.3-0.4 eV of doping, about 0.1 eV more than with the fl-resist. The PMMA transferred graphene was rinsed with dichloromethane and acetone before measurement. Graphene transferred onto TPBi was analyzed via Raman Spectroscopy. The presence of a strong signal from the G and 2D peaks, located at 1590.54 cm^{-2} and 2683.0 cm^{-2} respectively, indicate that graphene is successfully transferred by fl-method onto organic small-molecule substrates. [181,182] The fl-transferred graphene on the organic thin-film has the expected peak positions, relative heights, and full-width half-maximums (FWHM) that are expected as seen in the measured Raman spectra of graphene transferred onto SiO_2, via the same process, shown in Figure 4.4d. Deviations between graphene on SiO_2 and TPBi are a result of small levels of doping, [180, 183] and/or strain, [184] while the more significant difference in the 2D peak between our fl-transferred films and typical values indicate some areas of 2-layer graphene. The close agreement of Raman spectra between silicon and TPBi demonstrates the effectiveness of the fl-transfer process of graphene onto both high- and low-energy substrates.

4.2 Graphene Devices

4.2.1 Graphene Transistor

We fabricated graphene field effect transistors (GFETs) by orthogonal fl-resist transfer which perform as well as other CVD-grown polymer-transfer GFETs. The GFETs, shown in Figure 4.6a, exhibit a Dirac point at 21 V and hole mobilities of $\mu_h = 400 cm^2 V^{-1} s^{-1}$ at room temperature. While the GFET mobilities are 1-2 orders of magnitude lower than the best CVD-graphene GFET mobilities, [61, 69] the fl-resist transfer GFET fabrication does not require annealing to clean the graphene or solvents with the exception of the Orthogonal photoresist stripper. We attribute the larger Dirac points to impurity doping and contamination induced by the transfer

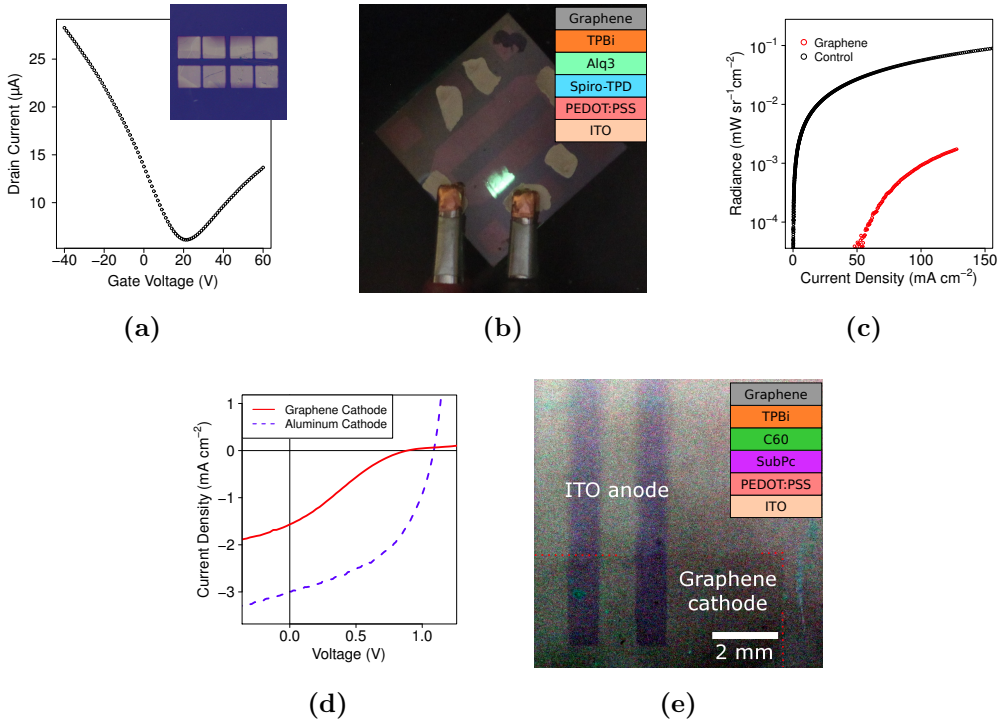

Figure 4.6: (a) GFET source-drain current. Inset: Photograph of four GFET devices on an SiO_2 chip. (b) Photograph of graphene laminated cathode OLED with a 2 x 4 mm active area. Inset: OLED device structure. (c) Radiance of graphene-laminated cathode OLED vs. control OLED. (d) J-V curves of control OPV with aluminum cathode vs. graphene-laminated cathode OLED. (e) Digital camera photograph of graphene OPV device. A red outline and digitally altered color balance increase visibility of the graphene cathode. Inset: OPV device structure.

process, which have been found in previous GFET studies. [185–187]

Transistor fabrication: Single layer graphene previously grown on 25 μm copper foils (99.999%) was spin coated with fluorinated resist and etched by oxygen plasma in order to remove any unwanted graphene from the back of the copper substrate. PDMS stamps were cut into small pieces (1 cm x 1 cm) in order to attach on top of the copper/graphene/fl-resist stack as a supporting layer. The graphene/PDMS stamp was etched in ammonium persulfate (Transene APS-100) for five hours to remove

copper from the backside. After etching, the remaining graphene/fl-resist/PDMS stamp was rinsed thoroughly with DI water and dried overnight before transfer to the target substrate. The target substrate, 300 nm SiO_2 on silicon, was cleaned in piranha solution, rinsed in DI water and dried. The graphene/fl-resist/PDMS stack was placed face-down on top of the wafer, on an 80°C hot plate. After stamp removal, the silicon/graphene/fl-resist sample was rinsed with fluorinated stripper. We used thermal physical vapor deposition to deposit Cr/Au (5 nm / 45 nm) source/drain contacts using a shadow mask. The transistor geometry has a W/L=20 (2000 μm/100 μm). Electrical characterization of the fabricated devices was performed with a Keithley 4200 parameter analyzer. All electrical measurements were performed at atmosphere and room temperature using three needle probes.

4.2.2 Graphene OLED

We demonstrated the compatibility and conductivity of transferred graphene by fabricating organic light emitting diode (OLED) devices with an fl-resist-transferred graphene cathode. We deposited the OLED thin-films onto ITO glass and used the fl-resist transfer method to laminate a graphene cathode on top of the organic thin-films. The graphene OLED structure is shown in the inset of Figure 4.6b. Graphene has previously been incorporated in OLED as bottom electrodes [59, 62], but has never been integrated as a top-electrode because there was no compatible process to transfer graphene onto underlying organic layers. The fl-resist transfer enables the use of graphene as a laminated electrode, expanding on the previous options of thermally deposited metals or sputtered indium tin oxide (ITO). Figure 4.6b shows a photograph of the graphene OLED. The transparency of the device is directly attributable to graphene, which transmits ~97.7% white light, in conjunction with a transparent ITO anode. [60] Figure 4.6c shows the radiance of the graphene OLED device compared to the control OLED device. The graphene OLED requires a higher turn-on voltage than the control OLED due to a low shunt resistance and work function

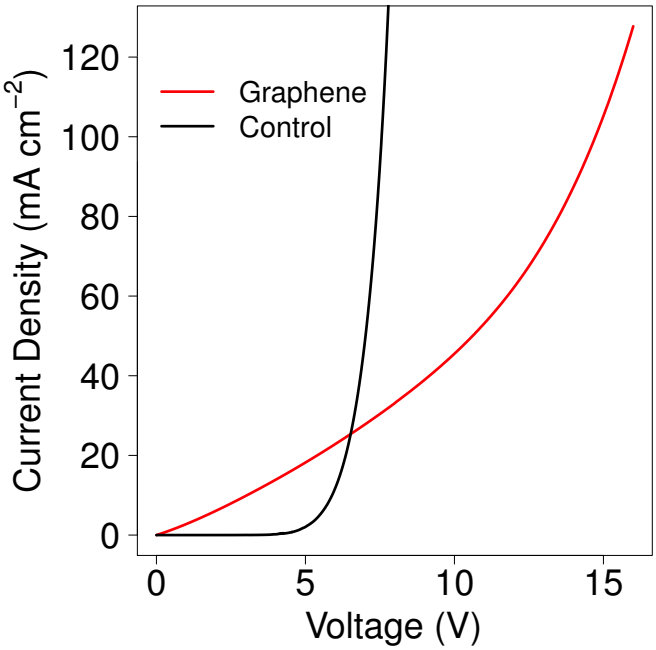

Figure 4.7: The current-voltage characteristics of OLED devices with graphene and magnesium-silver cathodes.

mismatch; the control Mg:Ag cathode has a better match to the Lowest Unoccupied Molecular Orbital (LUMO) energy level of the TPBi electron transporting material. As a result, the graphene OLED requires a higher current density before voltage can drop over the diode. The performance of the graphene OLED device may potentially be improved by decreasing the graphene work function, increasing the shunt resistance by reducing parasitic conduction, and decreasing graphene sheet resistance by using additional graphene layers. [61, 188]

Figure 4.7 shows the Current-Voltage characteristics of the graphene OLED device in comparison to a control device with a magnesium-silver cathode. The graphene OLED has a lower shunt resistance than the control device due to current passing through shorts between the graphene cathode and formation of a parasitic PEDOT:PSS anode. We estimate the sheet resistance of a two-layer graphene electrode to be 100 Ω $\square^{-1}$, based on a previous measurement of sheet resistance as a func-

tion of number of graphene layers. [61] We estimate the sheet resistance of the 80 nm MgAg cathode to be 0.3 $\Omega\ \square^{-1}$. The series resistance of the graphene OLED is higher because the sheet resistance of the graphene cathode is higher.

OLED fabrication: OLED devices were evaporated on pre-patterned ITO substrates (LumTec) with 9-15 $\Omega\ \square^{-1}$. Poly(3,4-ethylenedioxythiophene)-poly(styrenesulfonate) (PEDOT:PSS) (HC Stark) was filtered with 0.45 μm syringe filters and spin-coated on cleaned substrates at 3000 rpm to a thickness of approximately 80 nm. All films are subsequently annealed at 120°C for 1 hour. Following PEDOT:PSS deposition the substrates were taken into the N_2 glovebox. The OLED consists of 50 nm of N,N'-Bis(3-methylphenyl)-N,N'-diphenyl-9,9-spirobifluorene-2,7-diamine (Spiro-TPD, LumTec), 40 nm of Tris(8-hydroxyquinolinato)aluminium (AlQ_3, LumTec), 30 nm of 2,2',2"-(1,3,5-benzinetriyl)-tris(1-phenyl-1-H-benzimidazole) (TPBi, LumTec) and a cathode. Control devices have a 50 nm 10:1 Mg:Ag plus 25 nm Ag cathode. All OLED devices were kept in nitrogen for the duration of the experiment. OLED devices were driven by a Keithley 2602 sourcemeter and current-voltage data was collected. We measured radiance with a calibrated Newport 818 photodetector. The OLED peak emission is approximately 530 nm, as measured with an Ocean Optics USB4000 Fiber Optic Spectrometer.

4.2.3 Graphene OPV

We also fabricated semitransparent organic photovoltaic (OPV) devices with top-laminated graphene cathodes. OPV devices are typically fabricated with opaque metal electrodes such as aluminum, but have recently shown integration of graphene. [156, 163] We used the fl-resist transfer process to successively laminate two layers of graphene onto a SubPc/C60 small-molecule, vacuum-deposited OPV device on an ITO/glass substrate. The OPV device structure is shown in the inset of Figure 4.6e. The control devices have an identical device structure with an aluminum cathode in place of graphene. The graphene OPV device has a power conversion efficiency of

Cathode Type	V_{oc} [V]	J_{sc} [mA cm^{-2}]	FF [%]	η_p [%]
Laminated graphene	0.89	1.57	23	0.31
Aluminum	1.09	3.00	48	1.51

Table 4.1: Performance characteristics of OPV devices made with fl-resist-transferred graphene cathodes and aluminum cathodes.

0.31% and similar open-circuit voltage to the control device, shown in Figure 4.6d and Table 4.1. The graphene OPV has lower short-circuit current than the control device because it lacks a reflecting cathode, which decreases optical absorption 4.6e. The I-V curve of the graphene OPV device exhibits an S-shape, which occurs because the work function of graphene is too high to efficiently extract electrons. [189] The performance of the graphene device may potentially be improved by decreasing the graphene work function and decreasing the sheet resistance by using additional graphene layers. [61]

OPV fabrication: The OPV devices were evaporated on pre-patterned ITO substrates (LumTec) with 9-15 Ω $\square^{-1}$. The OPV consists of a 10 nm MoO_3 (molybdenum oxide) hole injection layer, 20 nm boron subphthalocyanine chloride (SubPc) electron donor, 40 nm C_{60} electron acceptor, 10 nm TPBi (2,2',2"-(1,3,5-benzinetriyl)-tris(1-phenyl-1-H-benzimidazole)) exciton blocking layer, and cathode. For graphene devices the cathode is two stamped monolayers of graphene transferred using the fl-resist process. Control devices have a 100 nm aluminum cathode. All depositions were performed at 1.0 Å sec^{-1} at less than $2 \cdot 10^{-6}$ Torr. The graphene device area was 2.58 mm^2 while the control device area was 1 mm^2. The illumination of the control device was from the bottom (through the ITO anode) while the illumination of the graphene device was from the top (through the graphene cathode). J-V characterization is performed using a Keithley 2400 source meter and a Newport solar simulator with an AM1.5 global tilt filter in a N_2 environment.

4.3 Conclusion

We successfully transferred graphene to organic thin-films via a modified PDMS stamp with an OSCoR orthogonal photoresist release layer. Raman spectroscopy indicates that the transferred graphene is high-quality, while SEM and AFM micrographs show a smooth surface morphology and low residual resist. We demonstrated that the OSCoR orthogonal photoresist transfer technique produces continuous, high-quality graphene by fabricating GFETs. We fabricated OLED and OPV devices to demonstrate the compatibility of our technique with organic thin-films. As the quality of CVD graphene improves, this transfer process may advance large-scale, graphene transfer to organic substrates to enable commercialization of flexible, semitransparent OLEDs and OPVs with graphene. This novel transfer technique potentially enables new hybrid organic-graphene device structures, such as tandem OPVs and all-carbon organic optoelectronic devices with no metal electrodes.

Chapter 5

Conclusions and Future Work

The field of organic electronics is driven by the desire to enable new functionality at low cost to increase the penetration of electronic devices. In order for organic electronics to be commercially viable, they must demonstrate high performance, increased stability, and integration with high-volume manufacturing techniques. Organic photovoltaic devices do not currently match the stability and performance of existing photovoltaic technologies. Processing techniques for organic photovoltaics and light emitting diodes must adapt to the low thermal budget and chemical incompatibilities of organic semiconductor materials. This thesis demonstrates new organic semiconductor device structures and processing techniques which advance the field of organic electronics towards commercial viability.

We investigated the design of nanostructured electrodes which improve fill factor performance in organic photovoltaic devices. By designing optimal nanostructured electrodes, we increased the charge extraction efficiency of OPV devices. The increased charge extraction causes an improvement in power conversion efficiency. This technique is potentially useful for many organic photovoltaic devices because many organic semiconductors have low charge carrier mobility, which is one of the root causes of poor fill factor.

Next, we investigated a general method for maximizing the efficiency of organic

photovoltaic devices by simultaneously optimizing light absorption and charge carrier collection. The short exciton diffusion length of many organic semiconductors means that films must be kept thin in order to efficiently extract charge. Optical absorption is correlated to film thickness, so thin films absorb less light. By designing surface nanostructures to trap incoming light, we demonstrate the ability to use thin OPV films with good charge collection while also increasing absorption. These techniques increase the efficiency of very thin OPV devices.

We investigated the recently isolated 2-D material graphene as a transparent conducting electrode for organic optoelectronic devices. The integrated of graphene is especially challenging because many techniques used in its processing are incompatible with organic semiconductor materials. The incompatibility between this electrode technology and organic materials has hindered the progress of highly transparent, flexible organic optoelectronic devices. We demonstrate a new graphene transfer technique that allows the direct transfer of graphene onto organic semiconductors. We showed that this technique can be used to fabricate graphene / organic photovoltaics and graphene / organic light emitting diodes.

The techniques developed in this thesis have been applied towards several key organic electronics challenges, with future work planned for each area. We plan to study OPV nanostructured electrode devices with impedance spectroscopy, an AC analysis technique which probes internal charge transport to provide more information than IV curves. We also plan to apply nanostructured electrodes to other third-generation photovoltaic technologies, such as quantum dot solar cells. We plan to iterate the design process of our graphene transfer technique to increase the efficiency of OPV and OLED devices. We also plan to integrated graphene with altered work functions to improve ohmic device contacts.

Bibliography

[1] "International energy outlook 2013." `http://www.eia.gov/forecasts/ieo/?src=Analysis-f3`.

[2] C. J. Chen, *Physics of solar energy*. Wiley. com, 2011.

[3] G. Carr, "Sunny uplands," *The Economist*, Nov 2012.

[4] B. O'Connor, K. P. Pipe, and M. Shtein, "Fiber based organic photovoltaic devices," *Applied Physics Letters*, vol. 92, no. 19, p. 193306, 2008.

[5] R. F. Bailey-Salzman, B. P. Rand, and S. R. Forrest, "Semitransparent organic photovoltaic cells," *Applied Physics Letters*, vol. 88, no. 23, p. 233502, 2006.

[6] R. F. Service, "Outlook brightens for plastic solar cells," *Science*, vol. 332, no. 6027, p. 293, 2011.

[7] L. Dou, J. You, J. Yang, C.-C. Chen, Y. He, S. Murase, T. Moriarty, K. Emery, G. Li, and Y. Yang, "Tandem polymer solar cells featuring a spectrally matched low-bandgap polymer," *Nature Photonics*, vol. 6, pp. 180–185, Mar 2012.

[8] C. W. Tang, "Two-layer organic photovoltaic cell," *Applied Physics Letters*, vol. 48, p. 183, 1986.

[9] C. Tang and S. VanSlyke, "Organic electroluminescent diodes," *Applied Physics Letters*, vol. 51, p. 913, 1987.

[10] K. Faied, M. Frechette, M. Ranger, L. Mazerolle, I. Levesque, M. Leclerc, T.-A. Chen, and R. D. Rieke, "Chromic phenomena in regioregular and nonregioregular polythiophene derivatives," *Chemistry of materials*, vol. 7, no. 7, pp. 1390–1396, 1995.

[11] H. Hoppe and N. S. Sariciftci, "Organic solar cells: An overview," *Journal of Materials Research*, vol. 19, no. 07, pp. 1924–1945, 2004.

[12] I. Hill, A. Rajagopal, A. Kahn, and Y. Hu, "Molecular level alignment at organic semiconductor-metal interfaces," *Applied Physics Letters*, vol. 73, no. 5, pp. 662–664, 1998.

[13] I. Kymissis, *Organic Field Effect Transistors: Theory, Fabrication and Characterization*. Springer, 2009.

[14] R. Y. Mahale, A. Arulkashmir, K. Dutta, and K. Krishnamoorthy, "Band edge modulated conjugated polymers for oxidation prevention," *Phys. Chem. Chem. Phys.*, vol. 14, pp. 4577–4583, 2012.

[15] P. E. Burrows, G. L. Graff, M. E. Gross, P. M. Martin, M.-K. Shi, M. Hall, E. Mast, C. Bonham, W. Bennett, and M. B. Sullivan, "Ultra barrier flexible substrates for flat panel displays," *Displays*, vol. 22, no. 2, pp. 65–69, 2001.

[16] B. Kippelen and J.-L. Brédas, "Organic photovoltaics," *Energy & Environmental Science*, vol. 2, no. 3, pp. 251–261, 2009.

[17] B. P. Rand, D. P. Burk, and S. R. Forrest, "Offset energies at organic semiconductor heterojunctions and their influence on the open-circuit voltage of thin-film solar cells," *Phys. Rev. B*, vol. 75, p. 115327, Mar 2007.

[18] S. R. Forrest, "The limits to organic photovoltaic cell efficiency," *MRS Bulletin*, vol. 30, pp. 28–32, Jan 2005.

[19] B. Ray and M. A. Alam, "Random vs regularized opv: Limits of performance gain of organic bulk heterojunction solar cells by morphology engineering," *Solar Energy Materials and Solar Cells*, vol. 99, no. 0, pp. 204 – 212, 2012. 9th International Meeting on Electrochromism.

[20] G. Yu, J. Gao, J. Hummelen, F. Wudl, and A. Heeger, "Polymer photovoltaic cells: enhanced efficiencies via a network of internal donor-acceptor heterojunctions," *Science-AAAS-Weekly Paper Edition*, vol. 270, no. 5243, pp. 1789–1790, 1995.

[21] B. Ray and M. A. Alam, "Optimum morphology and performance gains of organic solar cells," in *Photovoltaic Specialists Conference (PVSC), 2011 37th IEEE*, pp. 003477–003481, IEEE, 2011.

[22] J. D. Servaites, M. A. Ratner, and T. J. Marks, "Organic solar cells: a new look at traditional models," *Energy & Environmental Science*, vol. 4, no. 11, pp. 4410–4422, 2011.

[23] D. Y. Kim, J. Subbiah, G. Sarasqueta, F. So, H. Ding, Irfan, and Y. Gao, "The effect of molybdenum oxide interlayer on organic photovoltaic cells," *Applied Physics Letters*, vol. 95, no. 9, p. 093304, 2009.

[24] M. Vogel, S. Doka, C. Breyer, M. C. Lux-Steiner, and K. Fostiropoulos, "On the function of a bathocuproine buffer layer in organic photovoltaic cells," *Applied Physics Letters*, vol. 89, no. 16, p. 163501, 2006.

[25] B. P. Rand, J. Li, J. Xue, R. J. Holmes, M. E. Thompson, and S. R. Forrest, "Organic double-heterostructure photovoltaic cells employing thick tris (acetylacetonato) ruthenium (iii) exciton-blocking layers," *Advanced Materials*, vol. 17, no. 22, pp. 2714–2718, 2005.

[26] B. E. Lassiter, G. Wei, S. Wang, J. D. Zimmerman, V. V. Diev, M. E. Thompson, and S. R. Forrest, "Organic photovoltaics incorporating electron conduct-

ing exciton blocking layers," *Applied Physics Letters*, vol. 98, no. 24, p. 243307, 2011.

[27] V. Tripathi, D. Datta, G. Samal, A. Awasthi, and S. Kumar, "Role of exciton blocking layers in improving efficiency of copper phthalocyanine based organic solar cells," *Journal of Non-Crystalline Solids*, vol. 354, no. 19, pp. 2901–2904, 2008.

[28] T. Ameri, G. Dennler, C. Lungenschmied, and C. J. Brabec, "Organic tandem solar cells: a review," *Energy & Environmental Science*, vol. 2, no. 4, pp. 347–363, 2009.

[29] K. Vandewal, K. Tvingstedt, A. Gadisa, O. Inganas, and J. V. Manca, "On the origin of the open-circuit voltage of polymer-fullerene solar cells," *Nature Materials*, vol. 8, pp. 904–909, 11 2009.

[30] B. Ray, M. S. Lundstrom, and M. A. Alam, "Can morphology tailoring improve the open circuit voltage of organic solar cells?," *Applied Physics Letters*, vol. 100, no. 1, p. 013307, 2012.

[31] W. Shockley and H. J. Queisser, "Detailed balance limit of efficiency of p-n junction solar cells," *Journal of applied physics*, vol. 32, no. 3, pp. 510–519, 1961.

[32] M. A. Green, "Solar cells: operating principles, technology, and system applications," *Englewood Cliffs, NJ, Prentice-Hall, Inc., 1982. 288 p.*, vol. 1, 1982.

[33] J. Zhao, A. Wang, P. P. Altermatt, S. R. Wenham, and M. A. Green, "24% efficient perl silicon solar cell: Recent improvements in high efficiency silicon cell research," *Solar Energy Materials and Solar Cells*, vol. 4142, no. 0, pp. 87 – 99, 1996.

[34] T. Kirchartz, K. Taretto, and U. Rau, "Efficiency limits of organic bulk heterojunction solar cells," *The Journal of Physical Chemistry C*, vol. 113, no. 41, pp. 17958–17966, 2009.

[35] D. Veldman, O. Ipek, S. C. Meskers, J. Sweelssen, M. M. Koetse, S. C. Veenstra, J. M. Kroon, S. S. v. Bavel, J. Loos, and R. A. Janssen, "Compositional and electric field dependence of the dissociation of charge transfer excitons in alternating polyfluorene copolymer/fullerene blends," *Journal of the American Chemical Society*, vol. 130, no. 24, pp. 7721–7735, 2008.

[36] J. Mattheis, J. H. Werner, and U. Rau, "Finite mobility effects on the radiative efficiency limit of p n-junction solar cells," *Physical Review B*, vol. 77, no. 8, p. 085203, 2008.

[37] S. H. Park, A. Roy, S. Beaupré, S. Cho, N. Coates, J. S. Moon, D. Moses, M. Leclerc, K. Lee, and A. J. Heeger, "Bulk heterojunction solar cells with internal quantum efficiency approaching 100 percent," *Nature Photonics*, vol. 3, no. 5, pp. 297–302, 2009.

[38] R. D. Schaller, M. Sykora, J. M. Pietryga, and V. I. Klimov, "Seven excitons at a cost of one: redefining the limits for conversion efficiency of photons into charge carriers," *Nano Letters*, vol. 6, no. 3, pp. 424–429, 2006.

[39] D. N. Congreve, J. Lee, N. J. Thompson, E. Hontz, S. R. Yost, P. D. Reusswig, M. E. Bahlke, S. Reineke, T. Van Voorhis, and M. A. Baldo, "External quantum efficiency above 100% in a singlet-exciton-fission–based organic photovoltaic cell," *Science*, vol. 340, no. 6130, pp. 334–337, 2013.

[40] K. Petritsch, "Organic solar cell architectures,"

[41] B. W. D'Andrade and S. R. Forrest, "White organic light-emitting devices for solid-state lighting," *Advanced Materials*, vol. 16, no. 18, pp. 1585–1595, 2004.

[42] S. Reineke, F. Lindner, G. Schwartz, N. Seidler, K. Walzer, B. Lüssem, and K. Leo, "White organic light-emitting diodes with fluorescent tube efficiency," *Nature*, vol. 459, no. 7244, pp. 234–238, 2009.

[43] W. Brütting, S. Berleb, and A. G. Mückl, "Device physics of organic light-emitting diodes based on molecular materials," *Organic electronics*, vol. 2, no. 1, pp. 1–36, 2001.

[44] M. Baldo, S. Lamansky, P. Burrows, M. Thompson, and S. Forrest, "Very high-efficiency green organic light-emitting devices based on electrophosphorescence," *Applied Physics Letters*, vol. 75, p. 4, 1999.

[45] W. Brütting, J. Frischeisen, T. D. Schmidt, B. J. Scholz, and C. Mayr, "Device efficiency of organic light-emitting diodes: Progress by improved light outcoupling," *physica status solidi (a)*, vol. 210, no. 1, pp. 44–65, 2013.

[46] N. Koch, "Organic electronic devices and their functional interfaces," *ChemPhysChem*, vol. 8, no. 10, pp. 1438–1455, 2007.

[47] E. Ettedgui, H. Razafitrimo, Y. Gao, and B. Hsieh, "Band bending modified tunneling at metal/conjugated polymer interfaces," *Applied physics letters*, vol. 67, no. 18, pp. 2705–2707, 1995.

[48] L. Hung, C. Tang, and M. Mason, "Enhanced electron injection in organic electroluminescence devices using an al/lif electrode," *Applied Physics Letters*, vol. 70, no. 2, pp. 152–154, 1997.

[49] R. Meerheim, B. Lussem, and K. Leo, "Efficiency and stability of pin type organic light emitting diodes for display and lighting applications," *Proceedings of the IEEE*, vol. 97, no. 9, pp. 1606–1626, 2009.

[50] A. K. Geim and K. S. Novoselov, "The Rise of Graphene," *Nature Materials*, vol. 6, pp. 183–191, 2007.

[51] K. S. Novoselov, A. K. Geim, S. V. Morozov, D. Jiang, Y. Zhang, S. V. Dubonos, I. V. Grigorieva, and A. A. Firsov, "Electric Field Effect in Atomically Thin Carbon Films," *Science*, vol. 306, no. 5696, pp. 666–669, 2004.

[52] K. S. Novoselov, D. Jiang, F. Schedi, T. J. Booth, V. V. Khotkevich, S. V. Morozov, and A. K. Geim, "Two-dimensional atomic crystals," *Proceedings of the National Academy of Sciences*, vol. 102, pp. 10451–10453, 2005.

[53] Y. Zhang, Y.-W. Tan, H. L. Stormer, and P. Kim, "Experimental observation of the Quantum Hall effect and Berry's phase in graphene," *Nature*, vol. 438, pp. 201–204, 2005.

[54] Y.-W. Tan, Y. Zhang, K. Bolotin, Y. Zhao, S. Adam, E. H. Hwang, S. Das Sarma, H. L. Stormer, and P. Kim, "Measurement of Scattering Rate and Minimum Conductivity in Graphene," *Physical Review Letters*, vol. 99, pp. 10–13, Dec. 2007.

[55] P. Blake, P. D. Brimicombe, R. R. Nair, T. J. Booth, D. Jiang, F. Schedin, L. A. Ponomarenko, S. V. Morozov, H. F. Gleeson, E. W. Hill, A. K. Geim, and K. S. Novoselov, "Graphene-based liquid crystal device.," *Nano letters*, vol. 8, pp. 1704–8, June 2008.

[56] M. Lemme, T. Echtermeyer, M. Baus, B. Szafranek, J. Bolten, M. Schmidt, T. Wahlbrink, and H. Kurz, "Mobility in graphene double gate field effect transistors," *Solid-State Electronics*, vol. 52, pp. 514–518, Apr. 2008.

[57] C. Lee, X. Wei, J. W. Kysar, and J. Hone, "Measurement of the Elastic Properties and Intrinsic Strength of Monolayer Graphene," *Science*, vol. 321, pp. 385–388, 2008.

[58] K. S. Kim, Y. Zhao, H. Jang, S. Y. Lee, J. M. Kim, K. S. Kim, J.-H. Ahn, P. Kim, J.-Y. Choi, and B. H. Hong, "Large-scale pattern growth of graphene

films for stretchable transparent electrodes," *Nature*, vol. 457, pp. 706–710, Feb. 2009.

[59] L. G. D. Arco, Y. Zhang, C. W. Schlenker, K. Ryu, M. E. Thompson, and C. Zhou, "Continuous, Highly Flexible, and Transparent Graphene Films by Chemical Vapor Deposition for Organic Photovoltaics," *ACS Nano*, vol. 4, no. 5, pp. 2865–2873, 2010.

[60] R. R. Nair, P. Blake, A. N. Grigorenko, K. S. Novoselov, T. J. Booth, T. Stauber, N. M. R. Peres, and A. K. Geim, "Fine Structure Constant Defines Visual Transparency of Graphene," *Science*, vol. 320, no. 5881, p. 1308, 2008.

[61] S. Bae, H. Kim, Y. Lee, X. Xu, J.-S. Park, Y. Zheng, J. Balakrishnan, T. Lei, H. R. Kim, Y. I. Song, Y.-J. Kim, K. S. Kim, B. Ozyilmaz, J.-H. Ahn, B. H. Hong, and S. Lijima, "Roll-to-roll production of 30-inch graphene films for transparent electrodes," *Nature Nanotechnology*, vol. 5, pp. 574–578, 2010.

[62] C.-a. Di, D. Wei, G. Yu, Y. Liu, Y. Guo, and D. Zhu, "Patterned Graphene as Source/Drain Electrodes for Bottom-Contact Organic Field-Effect Transistors," *Advanced Materials*, vol. 20, no. 17, pp. 3289–3293, 2008.

[63] X. Wan, G. Long, L. Huang, and Y. Chen, "Graphene–a promising material for organic photovoltaic cells," *Advanced Materials*, vol. 23, no. 45, pp. 5342–5358, 2011.

[64] H. Schmidt, H. Flugge, T. Winkler, T. Bulow, T. Riedl, and W. Kowalsky, "Efficient semitransparent inverted organic solar cells with indium tin oxide top electrode," *Applied Physics Letters*, vol. 94, no. 24, pp. –, 2009.

[65] G. Gu, V. Bulovic, P. E. Burrows, S. R. Forrest, and M. E. Thompson, "Transparent organic light emitting devices," *Applied Physics Letters*, vol. 68, no. 19, 1996.

[66] S. R. Forrest, "The road to high efficiency organic light emitting devices," *Organic Electronics*, vol. 4, no. 2, pp. 45–48, 2003.

[67] J. Wu, H. a. Becerril, Z. Bao, Z. Liu, Y. Chen, and P. Peumans, "Organic solar cells with solution-processed graphene transparent electrodes," *Applied Physics Letters*, vol. 92, no. 26, p. 263302, 2008.

[68] J. Wu, M. Agrawal, H. A. Becerril, Z. Bao, Z. Liu, Y. Chen, and P. Peumans, "Organic light-emitting diodes on solution-processed graphene transparent electrodes," *ACS nano*, vol. 4, no. 1, pp. 43–48, 2009.

[69] N. Petrone, C. R. Dean, I. Meric, A. M. van der Zande, P. Y. Huang, L. Wang, D. Muller, K. L. Shepard, and J. Hone, "Chemical vapor deposition-derived graphene with electrical performance of exfoliated graphene," *Nano Letters*, vol. 12, no. 6, pp. 2751–2756, 2012.

[70] C. Dean, A. Young, I. Meric, C. Lee, L. Wang, S. Sorgenfrei, K. Watanabe, T. Taniguchi, P. Kim, K. Shepard, *et al.*, "Boron nitride substrates for high-quality graphene electronics," *Nature nanotechnology*, vol. 5, no. 10, pp. 722–726, 2010.

[71] H. Liu, Y. Liu, and D. Zhu, "Chemical doping of graphene," *Journal of Materials Chemistry*, vol. 21, no. 10, pp. 3335–3345, 2011.

[72] Y.-J. Yu, Y. Zhao, S. Ryu, L. E. Brus, K. S. Kim, and P. Kim, "Tuning the graphene work function by electric field effect.," *Nano letters*, vol. 9, pp. 3430–4, Oct. 2009.

[73] P. Khomyakov, G. Giovannetti, P. Rusu, G. Brocks, J. Van den Brink, and P. Kelly, "First-principles study of the interaction and charge transfer between graphene and metals," *Physical Review B*, vol. 79, no. 19, p. 195425, 2009.

[74] G. Jo, S.-I. Na, S.-H. Oh, S. Lee, T.-S. Kim, G. Wang, M. Choe, W. Park, J. Yoon, D.-Y. Kim, *et al.*, "Tuning of a graphene-electrode work function to enhance the efficiency of organic bulk heterojunction photovoltaic cells with an inverted structure," *Applied Physics Letters*, vol. 97, p. 213301, 2010.

[75] T. M. Clarke, F. C. Jamieson, and J. R. Durrant, "Transient absorption studies of bimolecular recombination dynamics in polythiophene/fullerene blend films," *The Journal of Physical Chemistry C*, vol. 113, no. 49, pp. 20934–20941, 2009.

[76] B. A. Gregg and M. C. Hanna, "Comparing organic to inorganic photovoltaic cells: Theory, experiment, and simulation," *Journal of Applied Physics*, vol. 93, no. 6, pp. 3605–3614, 2003.

[77] S. R. Cowan, W. L. Leong, N. Banerji, G. Dennler, and A. J. Heeger, "Identifying a threshold impurity level for organic solar cells: Enhanced first-order recombination via well-defined pc84bm traps in organic bulk heterojunction solar cells," *Advanced Functional Materials*, vol. 21, no. 16, pp. 3083–3092, 2011.

[78] J. Yu, Y. Zang, H. Li, and J. Huang, "Fill factor enhancement of organic solar cells based on a wide bandgap phosphorescent material and c60," *Thin Solid Films*, vol. 520, no. 21, pp. 6653 – 6657, 2012.

[79] C. M. Proctor, C. Kim, D. Neher, and T.-Q. Nguyen, "Nongeminate recombination and charge transport limitations in diketopyrrolopyrrole-based solution-processed small molecule solar cells," *Advanced Functional Materials*, vol. 23, no. 28, pp. 3584–3594, 2013.

[80] M. Green, J. Zhao, A. Wang, and S. Wenham, "Very high efficiency silicon solar cells-science and technology," *Electron Devices, IEEE Transactions on*, vol. 46, pp. 1940 –1947, Oct 1999.

[81] C.-F. Lin, S.-W. Liu, C.-C. Lee, J.-C. Hunag, W.-C. Su, T.-L. Chiu, C.-T. Chen, and J.-H. Lee, "Open-circuit voltage and efficiency improvement of

subphthalocyanine-based organic photovoltaic device through deposition rate control," *Solar Energy Materials and Solar Cells*, vol. 103, no. 0, pp. 69 – 75, 2012.

[82] G. Wei, S. Wang, K. Renshaw, M. E. Thompson, and S. R. Forrest, "Solution-processed squaraine bulk heterojunction photovoltaic cells," *ACS Nano*, vol. 4, no. 4, pp. 1927–1934, 2010.

[83] C. Melzer, E. J. Koop, V. D. Mihailetchi, and P. W. M. Blom, "Hole transport in poly(phenylene vinylene)/methanofullerene bulk-heterojunction solar cells," *Advanced Functional Materials*, vol. 14, no. 9, pp. 865–870, 2004.

[84] R. Pandey, A. A. Gunawan, K. A. Mkhoyan, and R. J. Holmes, "Efficient organic photovoltaic cells based on nanocrystalline mixtures of boron subphthalocyanine chloride and c60," *Advanced Functional Materials*, vol. 22, no. 3, pp. 617–624, 2012.

[85] B. Ray, M. Khan, C. Black, and M. Alam, "Nanostructured electrodes for organic solar cells: Analysis and design fundamentals," *Photovoltaics, IEEE Journal of*, vol. 3, pp. 318–329, Jan 2013.

[86] W. Tress, A. Petrich, M. Hummert, M. Hein, K. Leo, and M. Riede, "Imbalanced mobilities causing s-shaped iv curves in planar heterojunction organic solar cells," *Applied Physics Letters*, vol. 98, no. 6, p. 063301, 2011.

[87] W.-B. Chen, H.-F. Xiang, Z.-X. Xu, B.-P. Yan, V. Roy, C.-M. Che, and P.-T. Lai, "Improving efficiency of organic photovoltaic cells with pentacene-doped cupc layer," *Applied Physics Letters*, vol. 91, no. 19, p. 191109, 2007.

[88] G. Li, V. Shrotriya, J. Huang, Y. Yao, T. Moriarty, K. Emery, and Y. Yang, "High-efficiency solution processable polymer photovoltaic cells by self-organization of polymer blends," *Nature materials*, vol. 4, no. 11, pp. 864–868, 2005.

[89] C.-W. Chu, H. Yang, W.-J. Hou, J. Huang, G. Li, and Y. Yang, "Control of the nanoscale crystallinity and phase separation in polymer solar cells," *Applied Physics Letters*, vol. 92, no. 10, p. 103306, 2008.

[90] C.-Y. Nam, Q. Wu, D. Su, C.-Y. Chiu, N. J. Tremblay, C. Nuckolls, and C. T. Black, "Nanostructured electrodes for organic bulk heterojunction solar cells: Model study using carbon nanotube dispersed polythiophene-fullerene blend devices," *Journal of Applied Physics*, vol. 110, no. 6, p. 064307, 2011.

[91] M.-S. Kim, B.-G. Kim, and J. Kim, "Effective variables to control the fill factor of organic photovoltaic cells," *ACS Applied Materials & Interfaces*, vol. 1, no. 6, pp. 1264–1269, 2009. PMID: 20355922.

[92] J. Wagner, M. Gruber, A. Hinderhofer, A. Wilke, B. Brker, J. Frisch, P. Amsalem, A. Vollmer, A. Opitz, N. Koch, F. Schreiber, and W. Brtting, "High fill factor and open circuit voltage in organic photovoltaic cells with diindenoperylene as donor material," *Advanced Functional Materials*, vol. 20, no. 24, pp. 4295–4303, 2010.

[93] Z. Hu, J. Zhang, and Y. Zhao, "Effect of textured electrodes with light-trapping on performance of polymer solar cells," *Journal of Applied Physics*, vol. 111, no. 10, p. 104516, 2012.

[94] B. Niesen, B. P. Rand, P. Van Dorpe, D. Cheyns, L. Tong, A. Dmitriev, and P. Heremans, "Plasmonic efficiency enhancement of high performance organic solar cells with a nanostructured rear electrode," *Advanced Energy Materials*, pp. 145–150, 2012.

[95] M. Niggemann, M. Glatthaar, A. Gombert, A. Hinsch, and V. Wittwer, "Diffraction gratings and buried nano-electrode – architectures for organic solar cells," *Thin Solid Films*, vol. 451452, no. 0, pp. 619 – 623, 2004.

[96] Z. Yu, A. Raman, and S. Fan, "Fundamental limit of nanophotonic light trapping in solar cells," *Proceedings of the National Academy of Sciences*, 2010.

[97] J. E. Allen and C. T. Black, "Improved power conversion efficiency in bulk heterojunction organic solar cells with radial electron contacts," *ACS Nano*, vol. 5, no. 10, pp. 7986–7991, 2011.

[98] M.-H. Hsu, P. Yu, J.-H. Huang, C.-H. Chang, C.-W. Wu, Y.-C. Cheng, and C.-W. Chu, "Balanced carrier transport in organic solar cells employing embedded indium-tin-oxide nanoelectrodes," *Applied Physics Letters*, vol. 98, no. 7, p. 073308, 2011.

[99] M. K. Fung, Y. C. Sun, A. Ng, A. M. C. Ng, A. B. Djurisic, H. T. Chan, and W. K. Chan, "Indium tin oxide nanorod electrodes for polymer photovoltaics," *ACS Applied Materials & Interfaces*, vol. 3, no. 2, pp. 522–527, 2011.

[100] J. H. Lee, D. W. Kim, H. Jang, J. K. Choi, J. Geng, J. W. Jung, S. C. Yoon, and H.-T. Jung, "Enhanced solar-cell efficiency in bulk-heterojunction polymer systems obtained by nanoimprinting with commercially available aao membrane filters," *Small*, vol. 5, no. 19, pp. 2139–2143, 2009.

[101] H. K. Lee, J. H. Jeon, D. H. Wang, O. O. Park, J.-K. Kim, S. H. Im, and J. H. Park, "Enhanced charge collection via nanoporous morphology in polymer solar cells," *Applied Physics Letters*, vol. 96, no. 10, p. 103304, 2010.

[102] P. Yu, C.-H. Chang, M.-S. Su, M.-H. Hsu, and K.-H. Wei, "Embedded indium-tin-oxide nanoelectrodes for efficiency and lifetime enhancement of polymer-based solar cells," *Applied Physics Letters*, vol. 96, no. 15, p. 153307, 2010.

[103] R. Pandey, Y. Zou, and R. J. Holmes, "Efficient, bulk heterojunction organic photovoltaic cells based on boron subphthalocyanine chloride-c70," *Applied Physics Letters*, vol. 101, pp. 033308–1–033308–4, Jul 2012.

[104] K. L. Mutolo, E. I. Mayo, B. P. Rand, S. R. Forrest, and M. E. Thompson, "Enhanced open-circuit voltage in subphthalocyanine/c60 organic photovoltaic cells," *Journal of the American Chemical Society*, vol. 128, no. 25, pp. 8108–8109, 2006.

[105] J. Yu, N. Wang, Y. Zang, and Y. Jiang, "Organic photovoltaic cells based on tpbi as a cathode buffer layer," *Solar Energy Materials and Solar Cells*, vol. 95, no. 2, pp. 664 – 668, 2011.

[106] Z. Gao, C. S. Lee, I. Bello, S. T. Lee, R.-M. Chen, T.-Y. Luh, J. Shi, and C. W. Tang, "Bright-blue electroluminescence from a silyl-substituted ter-(phenylene–vinylene) derivative," *Applied Physics Letters*, vol. 74, no. 6, pp. 865–867, 1999.

[107] S. K. Hau, H.-L. Yip, O. Acton, N. S. Baek, H. Ma, and A. K.-Y. Jen, "Interfacial modification to improve inverted polymer solar cells," *J. Mater. Chem.*, vol. 18, pp. 5113–5119, 2008.

[108] S. A. Mann, R. R. Grote, R. M. Osgood, and J. A. Schuller, "Dielectric particle and void resonators for thin film solar cell textures," *Optics Express*, vol. 19, pp. 25729–25740, Dec 2011.

[109] "Rsoft design group, inc.." `http://www.rsoftdesign.com`.

[110] S. L. Ren, Y. Wang, A. M. Rao, E. McRae, J. M. Holden, T. Hager, K. Wang, W.-T. Lee, H. F. Ni, J. Selegue, and P. C. Eklund, "Ellipsometric determination of the optical constants of c60 (buckminsterfullerene) films," *Applied Physics Letters*, vol. 59, no. 21, pp. 2678–2680, 1991.

[111] A. D. Rakic, A. B. Djurišic, J. M. Elazar, and M. L. Majewski, "Optical properties of metallic films for vertical-cavity optoelectronic devices," *Applied Optics*, vol. 37, pp. 5271–5283, Aug 1998.

[112] F. Hamelmann, A. Brechling, A. Aschentrup, U. Heinzmann, P. Jutzi, J. Sandrock, U. Siemeling, T. Ivanova, A. Szekeres, and K. Gesheva, "Thin molybdenum oxide films produced by molybdenum pentacarbonyl 1-methylbutylisonitrile with plasma-assisted chemical vapor deposition," *Thin Solid Films*, vol. 446, no. 2, pp. 167 – 171, 2004.

[113] H. Gommans, D. Cheyns, T. Aernouts, C. Girotto, J. Poortmans, and P. Heremans, "Electro-optical study of subphthalocyanine in a bilayer organic solar cell," *Advanced Functional Materials*, vol. 17, no. 15, pp. 2653–2658, 2007.

[114] K. L. Mutolo, E. I. Mayo, B. P. Rand, S. R. Forrest, and M. E. Thompson, "Enhanced open-circuit voltage in subphthalocyanine/c60 organic photovoltaic cells," *Journal of the American Chemical Society*, vol. 128, no. 25, pp. 8108–8109, 2006.

[115] H. Gommans, S. Schols, A. Kadashchuk, P. Heremans, and S. Meskers, "Exciton diffusion length and lifetime in subphthalocyanine films," *The Journal of Physical Chemistry C*, vol. 113, no. 7, pp. 2974–2979, 2009.

[116] J. Kim and S. Yim, "Influence of surface morphology evolution of subpc layers on the performance of subpc/c60 organic photovoltaic cells," *Applied Physics Letters*, vol. 99, no. 19, pp. 193303–193303, 2011.

[117] A. Polman and H. A. Atwater, "Photonic design principles for ultrahigh-efficiency photovoltaics," *Nature materials*, vol. 11, no. 3, pp. 174–177, 2012.

[118] E. Yablonovitch, "Statistical ray optics," *JOSA*, vol. 72, no. 7, pp. 899–907, 1982.

[119] Z. Yu, A. Raman, and S. Fan, "Fundamental limit of nanophotonic light trapping in solar cells," *Proceedings of the National Academy of Sciences*, vol. 107, no. 41, pp. 17491–17496, 2010.

[120] Y. Park, E. Drouard, O. El Daif, X. Letartre, P. Viktorovitch, A. Fave, A. Kaminski, M. Lemiti, and C. Seassal, "Absorption enhancement using photonic crystals for silicon thin film solar cells," *Optics express*, vol. 17, no. 16, pp. 14312–14321, 2009.

[121] J. R. Tumbleston, D.-H. Ko, E. T. Samulski, and R. Lopez, "Absorption and quasiguided mode analysis of organic solar cells with photonic crystal photoactive layers," *Optics Express*, vol. 17, no. 9, pp. 7670–7681, 2009.

[122] L. Chen, W. Sha, and W. Choy, "Light harvesting improvement of organic solar cells with," *Optics Express*, vol. 20, no. 7, pp. 8175–8185, 2012.

[123] W. Sha, W. Choy, Y. Wu, and W. Chew, "Optical and electrical study of organic solar cells with a," *Optics Express*, vol. 20, no. 3, pp. 2572–2580, 2012.

[124] A. J. Morfa, K. L. Rowlen, T. H. Reilly, M. J. Romero, and J. van de Lagemaat, "Plasmon-enhanced solar energy conversion in organic bulk heterojunction photovoltaics," *Applied Physics Letters*, vol. 92, no. 1, pp. 013504–013504, 2008.

[125] N. C. Lindquist, W. A. Luhman, S.-H. Oh, and R. J. Holmes, "Plasmonic nanocavity arrays for enhanced efficiency in organic photovoltaic cells," *Applied Physics Letters*, vol. 93, p. 123308, 2008.

[126] H. Shen and B. Maes, "Combined plasmonic gratings in organic solar cells," *Optics Express*, vol. 19, no. S6, pp. A1202–A1210, 2011.

[127] N. C. Panoiu, R. M. Osgood Jr, *et al.*, "Enhanced optical absorption for photovoltaics via excitation of waveguide and plasmon-polariton modes," *Optics letters*, vol. 32, no. 19, pp. 2825–2827, 2007.

[128] A. Raman, Z. Yu, and S. Fan, "Dielectric nanostructures for broadband light trapping in organic solar cells," in *CLEO: Science and Innovations*, Optical Society of America, 2011.

[129] S. A. Mann, R. R. Grote, R. M. Osgood, and J. A. Schuller, "Dielectric particle and void resonators for thin film solar cell textures," *Optics Express*, vol. 19, no. 25, pp. 25729–25740, 2011.

[130] A. P. Vasudev, J. A. Schuller, and M. L. Brongersma, "Nanophotonic light trapping with patterned transparent conductive oxides," *Optics Express*, vol. 20, no. 103, pp. A385–A394, 2012.

[131] P. Wang and R. Menon, "Optimization of periodic nanostructures for enhanced light-trapping in ultra-thin photovoltaics," *Optics express*, vol. 21, no. 5, pp. 6274–6285, 2013.

[132] "Best research-cell efficiencies." `http://www.nrel.gov/ncpv/images/efficiency_chart.jpg`.

[133] "Refractiveindex.info refractive index database." `http://refractiveindex.info/`.

[134] H. Gommans, D. Cheyns, T. Aernouts, C. Girotto, J. Poortmans, and P. Heremans, "Electro-optical study of subphthalocyanine in a bilayer organic solar cell," *Advanced functional materials*, vol. 17, no. 15, pp. 2653–2658, 2007.

[135] C. A. Barrios, M. Lipson, *et al.*, "Electrically driven silicon resonant light emitting device based on slot-waveguide," *Opt. Express*, vol. 13, no. 25, pp. 10092–10101, 2005.

[136] P. Mullner and R. Hainberger, "Structural optimization of silicon-on-insulator slot waveguides," *Photonics Technology Letters, IEEE*, vol. 18, no. 24, pp. 2557–2559, 2006.

[137] T. Baehr-Jones, M. Hochberg, C. Walker, and A. Scherer, "High-q optical resonators in silicon-on-insulator-based slot waveguides," *Applied Physics Letters*, vol. 86, no. 8, pp. 081101–081101, 2005.

[138] R. Oulton, G. Bartal, D. Pile, and X. Zhang, "Confinement and propagation characteristics of subwavelength plasmonic modes," *New Journal of Physics*, vol. 10, no. 10, p. 105018, 2008.

[139] R. F. Oulton, V. J. Sorger, D. Genov, D. Pile, and X. Zhang, "A hybrid plasmonic waveguide for subwavelength confinement and long-range propagation," *Nature Photonics*, vol. 2, no. 8, pp. 496–500, 2008.

[140] I. Avrutsky, R. Soref, and W. Buchwald, "Sub-wavelength plasmonic modes in a conductor-gap-dielectric system with a nanoscale gap," *Opt. Express*, vol. 18, no. 1, pp. 348–363, 2010.

[141] L. Zeng, C. W. Tang, and S. H. Chen, "Effects of active layer thickness and thermal annealing on polythiophene: Fullerene bulk heterojunction photovoltaic devices," *Applied Physics Letters*, vol. 97, p. 053305, 2010.

[142] J. D. Servaites, S. Yeganeh, T. J. Marks, and M. A. Ratner, "Efficiency enhancement in organic photovoltaic cells: consequences of optimizing series resistance," *Advanced Functional Materials*, vol. 20, no. 1, pp. 97–104, 2010.

[143] B. P. Rand, D. P. Burk, and S. R. Forrest, "Offset energies at organic semiconductor heterojunctions and their influence on the open-circuit voltage of thin-film solar cells," *Physical Review B*, vol. 75, no. 11, p. 115327, 2007.

[144] A. Yariv and P. Yeh, *Photonics: Optical Electronics in Modern Communications (The Oxford Series in Electrical and Computer Engineering)*. Oxford University Press, Inc., 2006.

[145] F. Hamelmann, A. Brechling, A. Aschentrup, U. Heinzmann, P. Jutzi, J. Sandrock, U. Siemeling, T. Ivanova, A. Szekeres, and K. Gesheva, "Thin molybdenum oxide films produced by molybdenum pentacarbonyl 1-methylbutylisonitrile with plasma-assisted chemical vapor deposition," *Thin Solid Films*, vol. 446, no. 2, pp. 167–171, 2004.

[146] "American society for testing and materials (astm)." `http://www.astm.org/`.

[147] T. Tamir and S.-T. Peng, "Analysis and design of grating couplers," *Applied physics*, vol. 14, no. 3, pp. 235–254, 1977.

[148] M. Li and S. J. Sheard, "Waveguide couplers using parallelogramic-shaped blazed gratings," *Optics communications*, vol. 109, no. 3, pp. 239–245, 1994.

[149] C. Allain and M. Cloitre, "Optical diffraction on fractals," *Physical Review B*, vol. 33, pp. 3566–3569, 1986.

[150] M. Lehman, "Fractal diffraction gratings built through rectangular domains," *Optics communications*, vol. 195, no. 1, pp. 11–26, 2001.

[151] Z. Yu, A. Raman, and S. Fan, "Fundamental limit of nanophotonic light trapping in solar cells," *Proceedings of the National Academy of Sciences*, vol. 107, no. 41, pp. 17491–17496, 2010.

[152] A. Sytchkova, D. Zola, L. Bailey, B. Mackenzie, G. Proudfoot, M. Tian, and A. Ulyashin, "Depth dependent properties of ito thin films grown by pulsed dc sputtering," *Materials Science and Engineering: B*, 2012.

[153] H. Park, J. A. Rowehl, K. K. Kim, V. Bulovic, and J. Kong, "Doped graphene electrodes for organic solar cells," *Nanotechnology*, vol. 21, no. 50, p. 505204, 2010.

[154] J. Wu, H. A. Becerril, Z. Bao, Z. Liu, Y. Chen, and P. Peumans, "Organic solar cells with solution-processed graphene transparent electrodes," *Applied Physics Letters*, vol. 92, p. 263302, 2008.

[155] M. W. Rowell, M. A. Topinka, M. D. McGehee, H.-J. Prall, G. Dennler, N. S. Sariciftci, L. Hu, and G. Gruner, "Organic solar cells with carbon nanotube network electrodes," *Applied Physics Letters*, vol. 88, no. 23, pp. 233506–233506, 2006.

[156] M. Cox, A. Gorodetsky, B. Kim, K. S. Kim, Z. Jia, P. Kim, C. Nuckolls, and I. Kymissis, "Single-layer graphene cathodes for organic photovoltaics," *Applied Physics Letters*, vol. 98, p. 123303, 2011.

[157] X. Liang, B. A. Sperling, I. Calizo, G. Cheng, C. A. Hacker, Q. Zhang, Y. Obeng, K. Yan, H. Peng, Q. Li, X. Zhu, H. Yuan, A. R. Hight Walker, Z. Liu, L.-m. Peng, and C. A. Richter, "Toward clean and crackless transfer of graphene," *ACS Nano*, vol. 5, no. 11, pp. 9144–9153, 2011.

[158] Y. Lee, S. Bae, H. Jang, S. Jang, S.-E. Zhu, S. H. Sim, Y. I. Song, B. H. Hong, and J.-H. Ahn, "Wafer-Scale Synthesis and Transfer of Graphene Films," *Nano Letters*, vol. 10, pp. 490–493, Jan. 2010.

[159] X. Li, Y. Zhu, W. Cai, M. Borysiak, B. Han, D. Chen, R. D. Piner, L. Colombo, and R. S. Ruoff, "Transfer of large-area graphene films for high-performance transparent conductive electrodes," *Nano Letters*, vol. 9, no. 12, pp. 4359–4363, 2009. PMID: 19845330.

[160] A. Reina, X. Jia, J. Ho, D. Nezich, H. Son, V. Bulovic, M. S. Dresselhaus, and J. Kong, "Large area, few-layer graphene films on arbitrary substrates by chemical vapor deposition," *Nano Letters*, vol. 9, no. 1, pp. 30–35, 2009.

[161] Y. J. Shin, Y. Wang, H. Huang, G. Kalon, A. T. S. Wee, Z. Shen, C. S. Bhatia, and H. Yang, "Surface-energy engineering of graphene," *Langmuir*, vol. 26, no. 6, pp. 3798–3802, 2010. PMID: 20158275.

[162] Y.-Y. Lee, K.-H. Tu, C.-C. Yu, S.-S. Li, J.-Y. Hwang, C.-C. Lin, K.-H. Chen, L.-C. Chen, H.-L. Chen, and C.-W. Chen, "Top laminated graphene electrode in a semitransparent polymer solar cell by simultaneous thermal annealing/releasing method.," *ACS nano*, vol. 5, pp. 6564–70, Aug. 2011.

[163] Z. Liu, J. Li, and F. Yan, "Package-free flexible organic solar cells with graphene top electrodes," *Advanced Materials*, vol. 25, no. 31, pp. 4296–4301, 2013.

[164] J. A. Robinson, M. LaBella, M. Zhu, M. Hollander, R. Kasarda, Z. Hughes, K. Trumbull, R. Cavalero, and D. Snyder, "Contacting graphene," *Applied Physics Letters*, vol. 98, no. 5, pp. –, 2011.

[165] J. Song, F.-Y. Kam, R.-Q. Png, W.-L. Seah, J.-M. Zhuo, G.-K. Lim, P. K. H. Ho, and L.-L. Chua, "A general method for transferring graphene onto soft surfaces," *Nature Nano*, pp. 1–7, Apr. 2013.

[166] S. W. Tong, Y. Wang, Y. Zheng, M.-F. Ng, and K. P. Loh, "Graphene intermediate layer in tandem organic photovoltaic cells," *Advanced Functional Materials*, vol. 21, no. 23, pp. 4430–4435, 2011.

[167] A. A. Zakhidov, J.-K. Lee, H. H. Fong, J. A. DeFranco, M. Chatzichristidi, P. G. Taylor, C. K. Ober, and G. G. Malliaras, "Hydrofluoroethers as orthogonal solvents for the chemical processing of organic electronic materials," *Advanced Materials*, vol. 20, no. 18, pp. 3481–3484, 2008.

[168] P. G. Taylor, J.-K. Lee, A. A. Zakhidov, M. Chatzichristidi, H. H. Fong, J. A. DeFranco, G. G. Malliaras, and C. K. Ober, "Orthogonal patterning of pedot: Pss for organic electronics using hydrofluoroether solvents," *Advanced Materials*, vol. 21, no. 22, pp. 2314–2317, 2009.

[169] J.-K. Lee, H. H. Fong, A. A. Zakhidov, G. E. McCluskey, P. G. Taylor, M. Santiago-Berrios, H. D. Abruna, A. B. Holmes, G. G. Malliaras, and C. K. Ober, "Semiperfluoroalkyl polyfluorenes for orthogonal processing in fluorous solvents," *Macromolecules*, vol. 43, no. 3, pp. 1195–1198, 2010.

[170] H. H. Fong, J.-K. Lee, Y.-F. Lim, A. A. Zakhidov, W. W. Wong, A. B. Holmes, C. K. Ober, and G. G. Malliaras, "Orthogonal processing and patterning enabled by highly fluorinated light-emitting polymers," *Advanced Materials*, vol. 23, no. 6, pp. 735–739, 2011.

[171] F. Machui, S. Langner, X. Zhu, S. Abbott, and C. J. Brabec, "Determination of the p3ht:pcbm solubility parameters via a binary solvent gradient method: Impact of solubility on the photovoltaic performance," *Solar Energy Materials and Solar Cells*, vol. 100, pp. 138–146, 2012.

[172] A. L. Ayzner, C. J. Tassone, S. H. Tolbert, and B. J. Schwartz, "Reappraising the need for bulk heterojunctions in polymer-fullerene photovoltaics: The role of carrier transport in all-solution-processed p3ht/pcbm bilayer solar cells," *The Journal of Physical Chemistry C*, vol. 113, no. 46, pp. 20050–20060, 2009.

[173] H. S. Hwang, A. A. Zakhidov, J.-K. Lee, X. Andre, J. A. DeFranco, H. H. Fong, A. B. Holmes, G. G. Malliaras, and C. K. Ober, "Dry photolithographic patterning process for organic electronic devices using supercritical carbon dioxide as a solvent," *J. Mater. Chem.*, vol. 18, pp. 3087–3090, 2008.

[174] D. J. Mascaro, M. E. Thompson, H. I. Smith, and V. Bulović, "Forming oriented organic crystals from amorphous thin films on patterned substrates via solvent-vapor annealing," *Organic electronics*, vol. 6, no. 5, pp. 211–220, 2005.

[175] D. Gundlach, T. Jackson, D. Schlom, and S. Nelson, "Solvent-induced phase transition in thermally evaporated pentacene films," *Applied Physics Letters*, vol. 74, no. 22, pp. 3302–3304, 1999.

[176] K. Glasmästar, J. Gold, A.-S. Andersson, D. S. Sutherland, and B. Kasemo, "Silicone transfer during microcontact printing," *Langmuir*, vol. 19, no. 13, pp. 5475–5483, 2003.

[177] J.-K. Lee, M. Chatzichristidi, A. A. Zakhidov, P. G. Taylor, J. A. DeFranco, H. S. Hwang, H. H. Fong, A. B. Holmes, G. G. Malliaras, and C. K. Ober, "Acid-sensitive semiperfluoroalkyl resorcinarene: An imaging material for organic electronics," *Journal of the American Chemical Society*, vol. 130, no. 35, pp. 11564–11565, 2008. PMID: 18686954.

[178] A. A. Zakhidov, J.-K. Lee, J. A. DeFranco, H. H. Fong, P. G. Taylor, M. Chatzichristidi, C. K. Ober, and G. G. Malliaras, "Orthogonal processing: A new strategy for organic electronics," *Chem. Sci.*, vol. 2, pp. 1178–1182, 2011.

[179] A. Pirkle, J. Chan, A. Venugopal, D. Hinojos, C. W. Magnuson, S. McDonnell, L. Colombo, E. M. Vogel, R. S. Ruoff, and R. M. Wallace, "The effect of chemical residues on the physical and electrical properties of chemical vapor deposited graphene transferred to sio2," *Applied Physics Letters*, vol. 99, no. 12, pp. –, 2011.

[180] J. Yan, Y. Zhang, P. Kim, and A. Pinczuk, "Electric Field Effect Tuning of Electron-Phonon Coupling in Graphene," *Physical Review Letters*, vol. 98, p. 166802, 2007.

[181] A. C. Ferrari, J. C. Meyer, V. Scardaci, C. Casiraghi, M. Lazzeri, F. Mauri, S. Piscanec, D. Jiang, K. S. Novoselov, S. Roth, and A. K. Geim, "Raman Spectrum of Graphene and Graphene Layers," *Physical Review Letters*, vol. 97, p. 187401, 2006.

[182] A. C. Ferrari, "Raman spectroscopy of graphene and graphite: Disorder, electron-phonon coupling, doping and nonadiabatic effects," *Solid State Communications*, vol. 143, pp. 47–57, 2007.

[183] A. Das, S. Pisana, B. Chakraborty, S. Piscanec, S. K. Saha, U. V. Waghmare, K. S. Novoselov, H. R. Krishnamurthy, A. K. Geim, A. C. Ferrari, and A. K. Sood, "Monitoring dopants by Raman scattering in an electrochemically top-gated graphene transistor," *Nature Nanotechnology*, vol. 3, pp. 210–215, 2008.

[184] M. Huang, H. Yan, C. Chen, D. Song, T. F. Heinz, and J. Hone, "Phonon softening and crystallographic orientation of strained graphene studied by Raman spectroscopy," *PNAS*, vol. 106, pp. 7304–7308, 2009.

[185] X. Li, W. Cai, J. An, S. Kim, J. Nah, D. Yang, R. Piner, A. Velamakanni, I. Jung, E. Tutuc, *et al.*, "Large-area synthesis of high-quality and uniform graphene films on copper foils," *Science*, vol. 324, no. 5932, pp. 1312–1314, 2009.

[186] A. Venugopal, J. Chan, X. Li, C. W. Magnuson, W. P. Kirk, L. Colombo, R. S. Ruoff, and E. M. Vogel, "Effective mobility of single-layer graphene transistors as a function of channel dimensions," *Journal of Applied Physics*, vol. 109, no. 10, pp. 104511–104511, 2011.

[187] X. Li, C. W. Magnuson, A. Venugopal, J. An, J. W. Suk, B. Han, M. Borysiak, W. Cai, A. Velamakanni, Y. Zhu, *et al.*, "Graphene films with large domain size by a two-step chemical vapor deposition process," *Nano letters*, vol. 10, no. 11, pp. 4328–4334, 2010.

[188] J. O. Hwang, J. S. Park, D. S. Choi, J. Y. Kim, S. H. Lee, K. E. Lee, Y.-H. Kim, M. H. Song, S. Yoo, and S. O. Kim, "Workfunction-tunable, n-doped reduced graphene transparent electrodes for high-performance polymer light-emitting diodes," *ACS Nano*, vol. 6, no. 1, pp. 159–167, 2012.

[189] A. Kumar, S. Sista, and Y. Yang, "Dipole induced anomalous s-shape i-v curves in polymer solar cells," *Journal of Applied Physics*, vol. 105, no. 9, p. 094512, 2009.

[190] M. Bass, C. DeCusatis, J. Enoch, V. Lakshminarayanan, G. Li, C. Macdonald, V. Mahajan, and E. Van Stryland, *Handbook of optics, Volume II: Design, fabrication and testing, sources and detectors, radiometry and photometry.* McGraw-Hill, Inc., 2009.

[191] "The r project for statistical computing." `http://www.r-project.org/`.

Appendix A

Measurement and Fabrication

A.1 Details of Sample Preparation

A.1.1 Substrates

ITO glass substrates were purchased from Luminescence Technology Corp (Taiwan). The ITO glass specifications are: a thickness of approximately 120 - 160 nm; a sheet resistance of approximately 9 - 15 Ω $\square^{-1}$; the optical transmission is better than 84% at 550 nm; the RMS roughness is less than 6 nm with maximum roughness of less than 35 nm. For some devices, we use custom pre-patterned ITO glass from the manufacturer.

Our standard cleaning process for preparing substrates is the following: substrates are removed from packaging and visually inspected for defects, scratches, and foreign material. The substrates are blown with dry N_2 to remove any debris. The substrates are placed in a wafer carrier or chip carrier. First, the substrates are sonicated for 10 minutes in a mild detergent solution. Second, the substrates are sonicated for 10 minutes in DI water. Third, the substrates are sonicated for 10 minutes each in acetone, isopropanol, and methanol. Finally, the substrates are blown or spun dry. In many cases the substrates are cleaned for 10 minutes in a UV/Ozone cleaner

to clean remaining residue or to improve the hydrophobicity of the substrate. ITO glass, in particular, is exposed to the UV/Ozone cleaner, because this results in a work function shift which is useful for organic electronic devices. After cleaning the substrates are ready for device fabrication.

A.1.2 Film Deposition

All organic and metal films were deposited in an Angstrom Engineering thermal physical vapor deposition system. Organic materials and oxides were deposited from tungsten baffled box sources with covers and baffles. Metals were deposited from tungsten folded metal boats. Organic materials were purchased from Luminescence Technology Corp. (Taiwan) and used without further purification; the materials are sublimated at the manufacturer.

A.2 Details of Measurements

A.2.1 External Quantum Efficiency

The spectrally resolved photocurrent (EQE) measurements are performed in air using a chopped monochromator (Newport, Inc.). The monochromator is normalized using a Newport 818 calibrated photodetector. The Newport photodetector has a factory calibrated responsivity (A/W). The short-circuit current was measured through a lock-in amplifier (Stanford Research) with zero applied bias, corresponding to V_{oc} = 0 V. Short-circuit current is converted to short-circuit current density by dividing by area. EQE equals the number of electrons in the external circuit divided by the number of incident photons and is defined in the measurement as

$$EQE(\lambda) = SR(\lambda)\dot{hc}/q\lambda \tag{A.1}$$

where $SR(\lambda) = J_{sc}(\lambda)/\Phi(\lambda)$. $\Phi(\lambda)$ is the radiance of the monochromator after normalization using the calibrated photodetector.

A.2.2 Details of OLED efficiency measurements

The OLED radiant efficiency measurements are performed in a N_2 glove box in the dark. The sensor is a Newport 818 calibrated photodetector with a 1 cm diameter sensor. The photodetector current is measured with a Keithley 2602 sourcemeter while the OLED current-voltage characteristic is simultaneously measured. The OLED device area is normalized using a 750 μm aperture. The radiant transfer function, from the OLED to the detector, is calculated using the following equation:

$$\Phi = M\pi \int \int \frac{cos(\theta_s)cos(\theta_d)}{s_{sd}^2} dA_s dA_d \tag{A.2}$$

Where s- terms represent the source and d- terms represent the detector. [190]

A.3 R script for analyzing photovoltaic device data

R is a free and open source software environment for statistical computing and image analysis. [191] R runs on many Windows, Linux, Mac OS and UNIX-based platforms. A majority of the figures in this thesis were prepared with R. The following R script, called opvPLOT, was developed for analyzing and plotting large sets of OPV data. opvPLOT generates an I-V plot of the measured device data, calculates performance metrics such as efficiency, fill factor, open-circuit voltage, short-circuit current and equivalent circuit resistances. The opvPLOT script also generates a dark current curve for the device. The sample image output is shown in Figure A.1.

```
#!/usr/bin/Rscript
# OPV performance and graphing script
# Jonathan Beck
# jhb2158@columbia.edu
# Columbia Lab for Unconventional Electronics
```

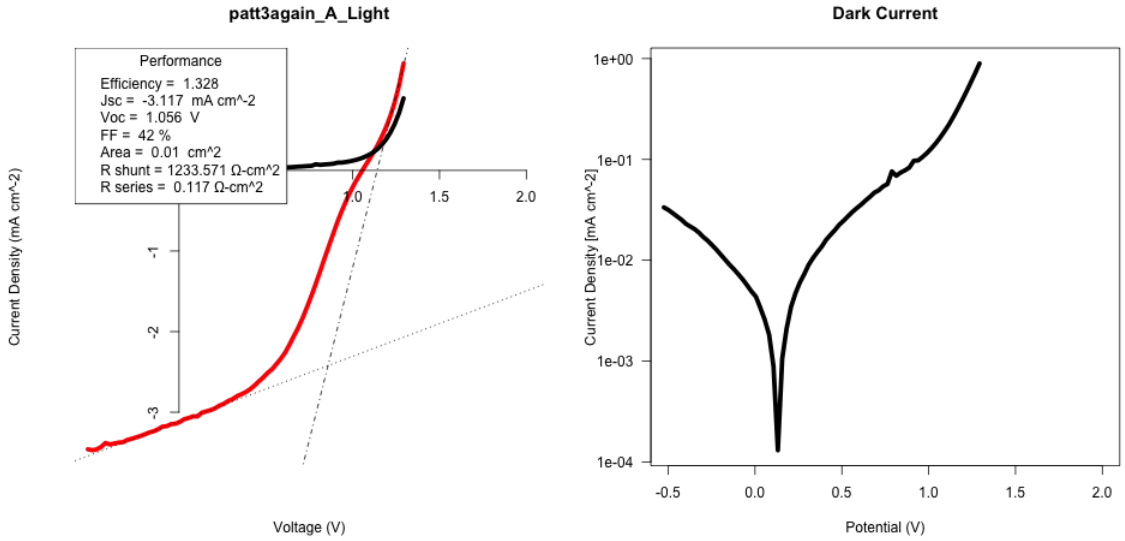

Figure A.1: Sample output of the opvPLOT script, developed by the author for analyzing OPV current-voltage data.

```
#
# Input files are dark, light I-V curves
# Input argument is the name of the light file
# Assumes dark file has the same name

# pass arguments to file
inputfiles <- commandArgs(TRUE)[1]
darkname <- sub("Light", "Dark", inputfiles)
lightname <- paste(inputfiles)

# load graph file
dark <- read.table(darkname, header=FALSE)
light <- read.table(lightname, header=FALSE)

# Convert I column of Dark,Light to mA/cm^2
```

```
cellArea <- 0.1*0.1
light[,2] <- light[,2] # * (1/cellArea) / 1000
dark[,2] <- dark[,2] # * (1/cellArea) / 1000

# OPV performance math
# Find Jsc
# Linear regression of 5 points surrounding V=0
absindex <- abs(light)
approxJsc <- which.min(absindex[,1])
jsclist <- rbind(light[approxJsc-3,],light[approxJsc-2,],
   light[approxJsc-1,], light[approxJsc,], light[approxJsc
   +1,], light[approxJsc+2,], light[approxJsc+3,])
Jsc_lm <- lm(jsclist[,2]~jsclist[,1])
Jsc_lm_coeff <- Jsc_lm$coefficients
Jsc <- Jsc_lm_coeff[1]

# Find shunt resistance
# R_Shunt <- (I / V)^-1 (inverse slope) around V=0
Rsh_slope <- Jsc_lm_coeff[2]
# print(paste("R shunt slope = ", Rsh_slope))
R_shunt <- (Rsh_slope)^-1
# print(R_shunt)

# Find Voc
abslight <- abs(light)
approxIntercept <- which.min(abslight[,2])
voclist <- rbind(light[approxIntercept-1,],light[
   approxIntercept,], light[approxIntercept+1,])
```

```
f <- approxfun(voclist)
Voc <- uniroot(f, lower=light[approxIntercept-1,1], upper=
    light[approxIntercept+1,1])$root

# Find series resistance
# Around Voc where J=0
start <- approxIntercept-4
finish <- approxIntercept+2
rs_list <- (light[start:finish,])
rs_lm <- lm(rs_list[,2]~rs_list[,1])
rs_lm_coeff <- rs_lm$coefficients
Rs_slope <- rs_lm_coeff[2]
# print(paste("R series slope = ", Rs_slope))
R_series <- (Rs_slope)^-1

# power calculations
power <- light[,1] * light[,2]
mppJ <- light[which.min(power),1]
mppV <- light[which.min(power),2]
ff <- (mppJ * mppV) / (Jsc * Voc)
pce <- 100*(-mppJ*mppV)/104 #1040 W/m^2

# output to PNG file
today <- Sys.Date()
outputfilename <- gsub("_Light.txt", "", inputfiles)
png(filename=paste(outputfilename, "_plot_", format(today,
    format="%Y%m%d"), ".png", sep=""), width=960, height=480)
```

```
# plot the graph
par(mfrow=c(1,2))
plot(light[,1], light[,2], type="l", col="red", xlab="Voltage
    (V)", ylab="Current Density (mA cm^-2)", axes=FALSE, lwd
    =5, xlim=c(-0.5,2), las=1)
lines(dark, type="l", col="black", lwd=5)
abline(Jsc_lm_coeff[1], Jsc_lm_coeff[2], lty=3)
abline(rs_lm_coeff[1], rs_lm_coeff[2], lty=4)

# make the graph pretty
title(main=paste(inputfiles))
axis(1, pos=0.0) #horizonatal
axis(2, outer=TRUE, pos=0.0) #vertical
legend("topleft", c(paste("Efficiency = ", round(pce, digits
    =3)), paste("Jsc = ", round(Jsc, digits=3), " mA cm^-2"),
    paste("Voc = ", round(Voc, digits=3), " V"), paste("FF = "
    , round(ff, digits=3)*100, "%"), paste("Area = ", cellArea
    , " cm^2"), paste("R shunt =", round(R_shunt, digits=3), "
    ?-cm^2"), paste("R series = ", round(R_series, digits=3),
    "?-cm^2")), title="Performance")

# plot the log I-V curve
plot(dark[,1], abs(dark[,2]), log="y", type="l", xlim=c
    (-0.5,2), xlab="Potential (V)", ylab = "Current Density [
    mA cm^-2]", las=1, lwd=5)
title("Dark Current")

graphics.off()
```

Appendix B

List of Publications

Jonathan H. Beck, Robert Barton, Marshall P. Cox, Konstantinos Alexandrou, Nicholas Petrone, Giorgia Olivieri, Shyuan Yang, James Hone, and Ioannis Kymissis, "Clean Graphene Electrodes on Organic Thin-Film Devices via Orthogonal Fluorinated Chemistry", submitted to Advanced Materials, 2013.

Jonathan H. Beck, Biswajit Ray, Richard R. Grote, Richard M. Osgood, Jr., Charles T. Black, Muhammad A. Alam, Ioannis Kymissis, "Nanostructured Electrodes Improve the Fill Factor of Organic Photovoltaics", submitted to IEEE Journal of Photovoltaics, 2013.

Jonathan H. Beck, James Basham, David Gundlach, Ioannis Kymissis, "Analysis of Optimized Photovoltaic Devices Using Impedance Spectroscopy", Materials Research Society, Boston, MA. December 2013. Conference Poster.

Giriraj Jnawali, Yi Rao, **Jonathan H. Beck**, Nicholas Petrone, Ioannis Kymissis, James Hone, and Tony F. Heinz, "Observation of ground-state and excited-state charge transfer at the C_{60}/graphene interface", submitted to Nano Letters, 2013.

Jonathan H. Beck, Biswajit Ray, Cheng-Chia Tsai, Richard R. Grote, Richard M. Osgood, Dirk Englund, Charles T. Black, Muhammad A. Alam, and Ioannis Kymissis, "Use of subwavelength structures to improve optics and transport in organic photovoltaics", Materials Research Society, Boston, MA. November 2012. Conference

Poster.

Cheng-Chia Tsai, Richard R. Grote, **Jonathan H. Beck**, Ashish Banerjee, Ioannis Kymissis, Richard M. Osgood, Jr., and Dirk Englund, "General method for simultaneous optimization of light trapping and carrier collection in an ultra-thin organic photovoltaic cell", in preparation.

Marshall P. Cox, Hongtao Ma, Matthias E. Bahlke, **Jonathan H. Beck**, Theodore H. Schwartz, and Ioannis Kymissis, "LED-based optical device for chronic in vivo cerebral blood volume measurement", IEEE Transactions on Electron Devices, 57, pp. 174-177, 2010.